Surface and electrochemical controls on UO_2 dissolution under anoxic conditions

Beng Thye Tan [a,*], Aleksej J. Popel [a], Richard J. Wilbraham [b], Jason Day [a], Giulio I. Lampronti [a], Colin Boxall [b], Ian Farnan [a]

[a] Department of Earth Sciences, University of Cambridge, Downing Street, Cambridge, CB2 3EQ, United Kingdom

[b] The Lloyd's Register Foundation Centre for Nuclear Engineering, Engineering Department, Lancaster University, Bailrigg, Lancashire, LA1 4YW, United Kingdom

[*] Corresponding author. Present address: Department of Earth Sciences, University of Cambridge, Downing Street, Cambridge, CB2 3EQ, United Kingdom, tel: +44 1223 768357, e-mail: btt30@cam.ac.uk

Abstract

The escape of radionuclides from underground spent nuclear fuel disposal facilities will likely result from anoxic dissolution of spent nuclear fuel by intruding groundwater. Anoxic dissolution of various forms of uranium dioxide (UO_2), namely bulk pellet, powder and thin film, has been investigated. Long-duration static batch dissolution experiments were designed to investigate the release of uranium ions in deionized water and any surface chemistry that may occur on the UO_2 surface. The dissolved uranium concentration for anoxic dissolution of nearly stoichiometric UO_2 was found to be of the order of 10^{-9} mol/l for the three different sample types. Further, clusters (~500 nm) of homogenous uranium-containing precipitates of ~20–100 nm grains were observed in thin film dissolution experiments. Such a low solubility of UO_2 across sample types and the observation of secondary phases in deionized water suggest that anoxic UO_2 dissolution does not only occur through a $U(IV)_{(solid)}$ to $U(VI)_{(aqueous)}$ process. Thus, we propose that dissolution of uranium under anoxic repository conditions may also proceed via $U(IV)_{(solid)}$ to $U(IV)_{(aqueous)}$, with subsequent $U(IV)_{(precipitates)}$ in a less defective form. Quantitative analysis of surface-sensitive EBSD diffractograms was conducted to elucidate lattice-mismatch induced cracks observed in UO_2 thin film studies. Variable temperature anoxic dissolution was conducted, and no increased uranium concentration was observed in elevated temperatures.

Keywords: UO_2; anoxic dissolution; secondary phases; surface alteration; nucleation; geological disposal

1. Introduction

The relative abundance of uranium as an energy resource, coupled with the high costs of spent nuclear fuel (SNF) reprocessing and the associated risks of nuclear proliferation, make a strong case for direct disposal of SNF in deep underground geological disposal facilities (GDF) [1,2]. The evaluation of such a facility is a multi-faceted problem; of which an important consideration is the projected radionuclide release rates from the spent fuel in the case of groundwater intrusion and secondary containment failure [3,4]. Extensive work had been devoted to the analysis of the different aspects of spent nuclear fuel dissolution under geological disposal conditions [2–11]. Depending on burn-up and local position in the rod (the linear power rating), spent fuel is comprised of ~96 at% uranium dioxide (UO_2) matrix with ~3 at% of fission products and ~1 at% of transuranium elements. As such, previous studies have shown that the release of radionuclides (apart from instant release fractions [12,13] of several percent of total inventory for some radionuclides), is mainly dependent on dissolution of the UO_2 matrix under the oxygen-free environment of deep geological facilities [3,4].

However, there has been no consensus on the proposed mechanisms of anoxic UO_2 dissolution in the literature. Ulrich et al. [14] initially suggested that anoxic dissolution of UO_2 proceeds via Eq. 1:

$$UO_2(s) + 4H^+ \rightleftharpoons U^{4+} + 2H_2O \quad (1).$$

Based on an XPS analysis of leached UO_2 samples consisting of bulk and surface U(IV), they noted surface oxidation to 7–10% U(VI) and ~20% U(V) under reducing dissolution conditions (5 vol% H_2, 95 vol% N_2 atmosphere) which was explained by a sequential oxidation mechanism of U(IV) to U(V) to U(VI) by water molecules, similar to

that proposed by Shoesmith and Sunder [15] for UO_2 dissolution below the oxidative threshold potential (–100 mV versus saturated calomel electrode on the UO_2 surface).

$$UO_2 + H_2O \rightarrow \left(U^{V}O_2OH\right)_{ads} + H^+ + e^-_{(aq)} \quad (2),$$

$$\left(U^{V}O_2OH\right)_{ads} + H_2O \rightarrow \left(U^{VI}O_2(OH)_2\right)_{ads} + H^+ + e^-_{(aq)} \quad (3).$$

A caveat to the applicability of these equations is the absence of detectable U(VI) in the sample solutions with a kinetic phosphorescence analyzer (KPA), although U(VI) is a few orders of magnitude more soluble than U(IV) [16]. Ulrich et al. concluded that the anoxic UO_2 dissolution was primarily driven by hydrolysis of U(IV) and not by oxidation to U(VI) [14]. However, it is possible that, although the sample transfer occurred with minimal exposure to oxygen in this work, a short exposure was enough to induce surface oxidation, which led to the observed U(V) and U(VI) at the surface. In addition, Ollila et al. [5] reported that after anoxic (N_2 atmosphere) dissolution of UO_2 in deionized water, the uranium oxidation state in the solution was U^{6+} as determined by anion exchange methods in an HCl medium within an inert atmosphere glove box (N_2). However, there was no information on the characterization of UO_2 samples in contact with the solution. In view of the above literature, the motivation of this paper is to investigate the anoxic dissolution mechanism of uranium dioxide with respect to the anoxic conditions pertaining in a GDF.

Considering the long timeline for SNF storage and disposal, this study focuses on the long-term surface changes and products due to dissolution of spent nuclear fuel. Three anoxic experiments with near stoichiometric uranium dioxide were conducted with

different aims. 1) The dissolution of uranium dioxide in solid pellet electrode form to determine electrochemical variation of both solution and surface and subsequent analysis of surface oxidation with Raman spectroscopy, Scanning Electron Microscopy (SEM) and Energy Dispersive X-ray (EDX) analysis techniques. 2) The dissolution of a single crystal uranium dioxide thin film (~100 nm thickness) deposited epitaxially on a (001) silicon substrate, to ascertain uranium dissolution and potential secondary phase precipitation [9,10] on a topographically flat surface with high surface sensitivity. 3) High-surface area UO_2 powder in steel heating vessels with PTFE (polytetrafluoroethylene) liners to analyse differences in dissolved uranium concentrations at different temperatures, simulating decay heat at different disposal ages.

2. Materials and methods

2.1. Anoxic conditions

Anoxic dissolution involves the exclusion of dissolved oxygen in the experiments as far as reasonably possible. All dissolution experiments were conducted in positive pressure gloveboxes with an argon atmosphere with oxygen concentrations controlled to 0.1 ppm O_2 for the thin film and powder experiments and a nitrogen atmosphere of 2.0 ppm O_2 for the solid pellet experiments. In all cases, the dissolution experiments took place in sealed containers containing deoxygenated water. Deionized Milli-Q water (18.2 MΩ/cm), for both dissolution and sample washing, was sparged with 5 vol% H_2 in 95 vol% Ar gas mixture for 6 hours to reduce the amount of dissolved oxygen to a

103 suitable low level. Post-sparging testing with CHEMetrics® Oxygen CHEMets Kit K-
104 7540 revealed dissolved oxygen content below the detection limit of 2.5 ppb. The
105 dissolved oxygen content was measured at the start and end of each experiment and
106 was found to be low at < 2.5 ppb. Sampling of the solution took place as rapidly as
107 possible and occurred infrequently. During the intervening periods, the vessels were
108 sealed.

109 *2.2. Sample preparation*

110 Efforts have been taken to reduce the amount of U(VI) and U(V) from surface
111 oxidation of the nominal UO_2 samples. Powder and thin film samples were reduced in a
112 5 vol% H_2, 95 vol% Ar atmosphere and heating to 800º C [17]. Sintered UO_2 pellets
113 were polished with SiC paper under deionized water to remove any oxidized surface
114 layer of UO_{2+x} that arises from exposure to the atmosphere for extended periods of time
115 [18]. Anderson et al. [19] have previously reported that such surface oxidation occurs
116 slowly as a logarithmic function of time due to the chemisorption of oxygen at room
117 temperatures. Pellet and thin film samples were subsequently pre-washed before
118 undertaking dissolution experiments.

119 A detailed description of the fabrication and initial characterisation of sintered UO_2
120 pellets has been previously reported by Hiezl et al. [20] with additional characterisation
121 by Popel et al. [10]. In order to make suitable electrodes for use in long-term dissolution
122 experiments, stoichiometric UO_2, disc-shaped slices of sintered pellets (~1 cm diameter
123 and ~1 mm thickness) were mounted onto a threaded brass rod using silver-loaded
124 epoxy. This assembly was then placed in a cylindrically shaped mould and cast in

125 epoxy resin in order to produce a suitable sealed working electrode. Prior to being
126 characterised, the working electrodes were polished using 600 and 1200 grit SiC paper
127 under deionized water (to avoid uranium dust formation). Such a polishing process
128 reduces differences in electrode surface area between samples and enhances the
129 reproducibility of triplicate dissolution experiments (see Section 2.5.1). Prior to
130 dissolution, the polished surfaces were examined by scanning electron microscopy and
131 Raman spectroscopy (see Section 2.3) before placing them in 10 ml of deoxygenated,
132 deionized water in a Nalgene® bottle for 21-hours pre-washing under a N_2 atmosphere
133 with 2.0 ppm O_2. This pre-wash phase again aims to remove any higher oxidation
134 uranium oxide phases which might have been formed, albeit slowly, in the processing
135 atmosphere and relies on the higher solubility of surface UO_{2+x} phases vs. bulk UO_2.
136 Indeed, previous literature studies [21–23] have found that the solubility product at the
137 standard state, K_{sp}^{o} of U(VI) is -22.46, significantly higher than that of U(IV), -52.0 with
138 slight variation dependent on solid form [24].

139 The thin film of UO_2 was produced by direct current reactive sputtering onto a single
140 crystal Si substrate with (001) orientation using a Labstation machine at the European
141 Commission Joint Research Centre (EC-JRC), Karlsruhe. The substrate was cleaned
142 before the film deposition with ethanol and heated to ~600 °C under pO_2 of 2×10^{-6}
143 mbar for 40–60 min [25]. A natural uranium metal target was used as a source of
144 uranium with argon used as the sputtering gas at a pAr set to 5×10^{-3} mbar and O_2
145 used as the reactive gas at a pO_2 set to 7×10^{-6} mbar. The Si substrate was maintained
146 at a temperature close to 600 °C. The film was deposited for 30 minutes with deposition
147 conditions which should give film thickness in the range from 90 to 270 nm. The thin film

148 sample was then annealed in an anoxic glove box-attached furnace at 800 °C with a
149 reducing mixture of 5 vol% H_2 in 95 vol% Ar for two hours, taking one hour to heat up
150 and three hours to cool down. It was subsequently transferred to another glove box,
151 where the dissolution experiment took place under an argon atmosphere at 0.1 ppm O_2.
152 Finally, pre-wash in 20 ml of sparged deionized water in a plastic bottle for 12 hours
153 was carried out before transfer to a fresh deionized water solution for the dissolution
154 experimental run (see section 2.5.2).

155 For the powder samples, high surface area, micro-porous UO_2 beads were produced
156 from uranyl nitrate at the EC-JRC by the sol-gel technique [26,27]. About 2.3 g of this
157 powder was weighed and transferred into a 1 ml alumina boat for annealing. In order to
158 achieve stoichiometry, the powder was annealed in a tube furnace attached to a glove
159 box where ingress and egress of the sample into the furnace occurs inside the glovebox
160 with an argon atmosphere (0.1 O_2 ppm). It was annealed at 800 °C for three hours with
161 a reducing gas mixture of 5 vol% H_2 in 95 vol% Ar, after an initial hour of pre-heating to
162 the requisite temperature. There was no pre-wash carried out for this set of
163 experiments.

164 *2.3. Sample characterisation*

165 The solid pellet samples were analysed before and after the dissolution experiment
166 by SEM with EDX as well as a Raman microscopy system. SEM-EDX was carried out at
167 20 keV using a JSM-6010PLUS (Jeol, Japan). Raman microscopy measurements were
168 taken using a Voyage confocal Raman microscope system (B&WTek, Newark, USA).
169 All Raman spectra were acquired with an excitation wavelength of 785 nm. The sample

was focussed using a 50× objective lens before taking spectra with an integration time of 40 seconds over a wavenumber range from 190 to 3000 cm^{-1}. Before analysis, the laser power was adjusted to < 5 mW using neutral density filters in order to avoid any thermal oxidation of UO_2 to U_3O_8 [28]. In order to account for surface roughness and surface inhomogeneity, 10 spectra were taken at random locations across the sample with the highest and lowest outliers removed to produce a sample average.

The thin film sample was analysed before and after the dissolution experiment by SEM, EDX, X-ray diffraction (XRD) and electron backscatter diffraction (EBSD) techniques [25]. A FEI Quanta 650F instrument operating at 5 kV with beam spot size 3 under high vacuum was used to acquire SEM images with a Bruker 6130 XFlash EDX detector. EBSD instrumentation from Bruker with an e-Flash$_{HD}$ detector associated with the FEI Quanta 650F SEM was used to obtain EBSD data; the resolution of each square pixel of 97 nm. The operating voltage was 20 kV and the beam spot size 5.5. The detector resolution was 320 × 240 pixels, while working distance and sample to detector distance was 26 mm and 15.5 mm respectively. Analysis of collected EBSD data from the uranium dioxide thin film was conducted with the computational aid of MTEX V5.0.3 [29], a freeware toolset for the commercial software package MATLAB™ [30]. The MATLAB™ toolbox MTEX provides a unique way to represent, analyse and interpret crystallographic preferred orientation, i.e. texture, based on integral ("pole figure") or individual orientation ("EBSD") measurements.

Due to limitations in examining radioactive uranium oxide powder under vacuum, capillary XRD was conducted with a Bruker D8 Advance diffractometer (Cu Kα radiation, λ = 1.541 Å, Ge monochromator and Sol-XE energy dispersive detector).

Measurements were carried out for 12 hours each over an angular range 25° ≤ 2θ ≤ 90° ($\Delta 2\theta$ = 0.01°). Data collection and indexing was performed with Bruker QUANTAX CrystaAlign software [31]. A full Rietveld refinement was carried out of the acquired diffraction patterns. The backgrounds were fitted using linear interpolation and the peak shape was modelled using a pseudo-Voigt function for the micro-porous uranium dioxide powder pre- and post-annealing. Based on the lattice parameter obtained of 5.466 Å, and the equation $a_x = 5.4690 - 0.12x$ [32], a bulk stoichiometric ratio prior to dissolution of $UO_{2.03}$ was found for the UO_2 powder. However, in this dissolution study, the bulk stoichiometric ratio may be lower than the surface. As discussed by Sunder [33], the surface is likely to be UO_{2+x} (0 < x < 0.25). This is because XRD is a bulk technique which convolutes~~convolutes~~the signal from the underlying bulk and surface signals hence typically registering lower values of *x* than surface sensitive Raman spectroscopy as Raman laser has a lower penetration depth than X-rays.

2.4. Aliquot analyses

For inductively coupled plasma mass spectrometry (ICP-MS), the acquired 1 ml aliquots (see section 2.5) were acidified with another 1 ml of 1 wt% HNO_3. All samples were analysed on a Perkin Elmer Nexion 350D ICP-MS instrument. The uranium calibration standards were prepared as an external calibration using serial dilutions of standards (blank, 0.001, 0.01, 0.10, 1.0, 10 ppb, mass basis) prepared from single element high purity standard (CPI, California, USA) in high purity 1 wt % HNO_3 (quartz distilled in house). The ICP-MS internal standards were 10 ppb Rh, In and Re and each sample was prepared in 1 wt % HNO_3, added online with a t-piece and mixing tube prior to the nebuliser. Two different independently prepared quality control standards (SPS-

SW2, LGC Standards, UK and SCP Science, Canada, ICP-MS Verification Mix) were repeatedly analysed throughout the run to check for calibration accuracy (~5%) with a similar precision. Instrumental drift was less than 10% measured for the raw intensity of the internal standards during the entire analytical run (50 or more solutions per batch). Solutions were analysed using a Micromist FM05 microconcentric nebuliser using a pumped flow rate of 80 µl/min (Glass Expansion, Australia) and a quartz cyclonic baffled spray chamber with nickel sampler and skimmer cones. ICP-MS sensitivity in this configuration was 4.5 × 10^5 cps/ppb In with CeO/Ce ratios = 2.8%. Concentration results were calculated using the Syngistix 1.1 software with a simple linear calibration line and intercept set to zero. The raw intensities were blank subtracted and internal standard normalised before calibration calculations were performed. All results (unknowns and standards) were accurately corrected for dilutions by mass by performing all dilutions with calibrated pipettes on a four place analytical balance.

For the leachate from the uranium dioxide thin film experiment, dynamic light scattering was used to confirm the absence of colloids greater than 5 nm. Inductively coupled plasma atomic emission spectroscopy (ICP-AES) of this leachate found the concentration of dissolved silicon in that experiment to be in the range of 15–25 ppb.

2.5. Dissolution experiment setups

A summary of the dissolution experiments has been tabulated at the end of this section in Table 1.

2.5.1 Solid pellet dissolution

After a 21-hour prewash and drying for 1 hour in the glovebox atmosphere, UO_2 electrodes were immersed in 220 ml of sparged, deionized water in a sealed (screw top) 480 ml Fisherbrand® PTFE dissolution vessel. Dissolution measurements were performed in triplicate~~, with the setup shown in Fig. 1~~s.

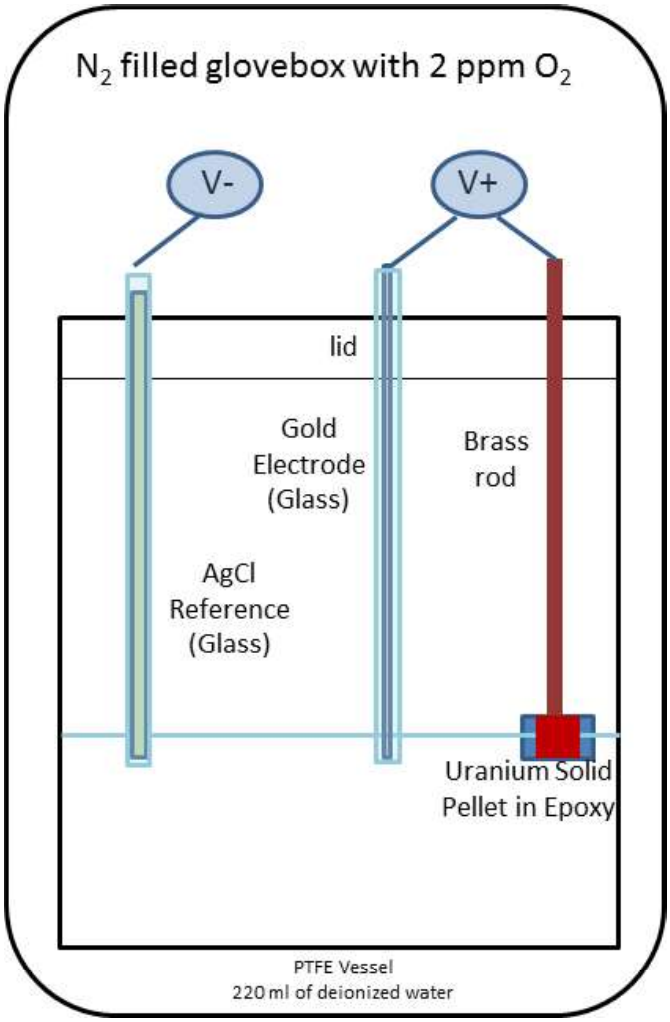

~~**Fig. 1.** Schematics of the solid UO_2 pellet dissolution experiment set up to determine the oxidation potential of the UO_2 surface and the solution.~~

To determine the electrochemical evolution of both the uranium dioxide electrode and the solution potential, open circuit potentiometry was used [34]. Solution potential was

246 measured using 500 μm Au disk electrodes, polished using 600 and 1200 grit SiC
247 papers and rinsed with deoxygenated, deionized water inside the glovebox prior to
248 immersion. Through the use of a simple switch box, the open circuit potential of both
249 electrodes was measured vs. one reference electrode. In order to avoid chloride
250 contamination, an ammonium nitrate saturated agar double junction was used with an
251 Ag|AgCl reference electrode (RE-5B, BASi, Indiana, USA). All vessels were tightly
252 closed to prevent water evaporation, with gaps around electrodes sealed using
253 parafilm®. One vessel filled with 250 ml of deionized water and an Au electrode only
254 (no UO_2 electrode) was used as a control. During dissolution, batch replenishment tests
255 were conducted, where ~1 ml aliquots of the solution sample were extracted and ~1 ml
256 of the deionized water was replenished at defined time intervals after the start of the
257 experiment, namely 2 hours, 6 hours, 1 day, 5 days, 12 days, 30 days, 61 days and 100
258 days. The amount of solution in the aliquots was monitored by weighing empty and filled
259 vials on a balance. The dissolution of all samples was performed at an ambient
260 temperature of ~25 °C for 100 days. After completion, the PTFE vessels were acid-
261 washed using 3 M HNO_3. 5 ml of each acid wash was used for ICP-MS analysis in order
262 to determine the presence of any uranium sorption or precipitation on the walls of the
263 leaching vessel.

264 *2.5.2 Thin film dissolution*

265 After the 12-hour prewash and drying for an hour, the UO_2 thin film sample was
266 rinsed with sparged, deionized water and placed into a 60 mL Fisherbrand® PTFE
267 dissolution vessel ~~(shown in Fig. 2)~~ containing 20 ml of the deionized water and two
268 blank Si substrates (to detect any U precipitation/nucleation from the solution) [25].

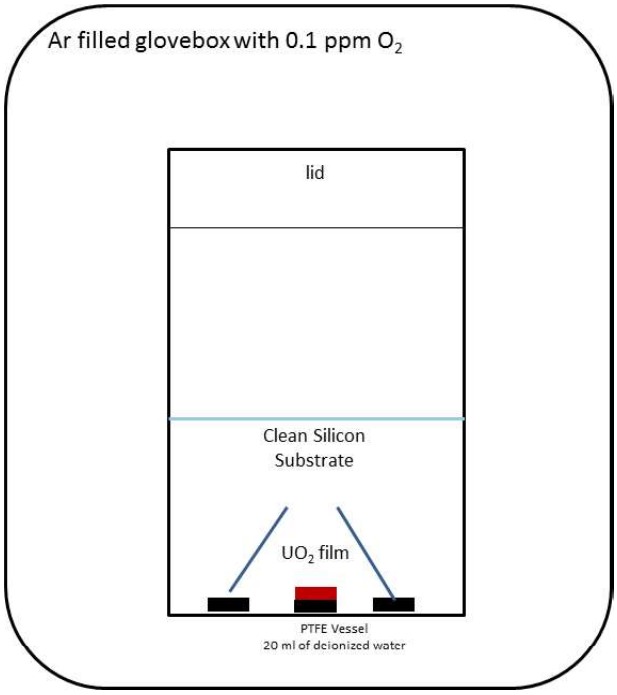

Fig. 2. Schematics of the UO_2 thin film dissolution experiment set up to ascertain uranium dissolution and potential secondary phase precipitation on topographically flat surface with high surface sensitivity.

Static batch replenishment tests were run where ~1 ml aliquots were extracted at various intervals and ~1 ml of the deionized water was replenished. One vessel, filled with 20 ml of the deionized water and two blank Si substrates, was used as a control blank. All vessels were tightly closed to prevent water evaporation. The amount of the solution transferred from the dissolution vessels into the vials was monitored by weighting empty and filled vials. The dissolution experiment was performed at an ambient temperature of ~25 °C for 140 days.

2.5.3 High surface area powder dissolution

After annealing, 100 mg of reduced UO_2 powder was weighed out carefully with a Mettler Toledo XS-104 mass balance and placed into each of twelve stainless steel leaching vessels with a PTFE liner and a Swagelock seal. Upon the addition of 4 ml of sparged, deionized water to each leaching vessel, the leaching vessel was tightly sealed and transferred to another glove box under double containment. The dissolution experiment was performed at 4 different temperatures ambient (~25 ˚C), 40 ˚C, 90 ˚C and 140 ˚C with deoxygenated water (<2.5 ppb O_2) within an Ar atmosphere glovebox (0.1 O_2 ppm). All vessels were kept in the glove box for the duration of the experiment and tightly sealed. The extraction was carried out on the 390th day with a syringe through a 0.45 µm pore size disposable filter.

Table 1

A summary of the UO_2 dissolution experiments conducted in this study

-	Annealing	Polishing	Prewashing	Oxygen content	Leaching test conditions
Pellet	No	Yes (SiC paper + deionized water)	Yes (21 hours) – 10 mL	2 ppm glovebox <2.5 ppb dissolved O_2	100 days 220 mL deionized water
Thin film	Yes (5% H_2 in Ar at 800 ^{0}C for 2 hours)	No.	Yes (12 hours) – 20 mL	0.1 ppm <2.5 ppb dissolved O_2	140 days 20 mL deionized water
Powder	Yes (5% H_2 in Ar at 800 ^{0}C for 2 hours)	Not applicable	No	0.1 ppm <2.5 ppb dissolved O_2	390 days 4 mL deionized water Filtration 0.45 µm

3. Results

3.1. Solid pellet dissolution

ICP-MS results, represented in Fig. 13, show a uranium concentration increase from 1×10^{-9} mol/l to ~6×10^{-9} mol/l being leached from the solid uranium pellet. Such a low level of uranium release is indicative of anoxic dissolution, which has a reduced rate of uranium ion release compared to oxic leaching [35]. This also agrees with the ~~Au-electrode recorded~~ end solution potential of the uranium containing pots (-56 mV, -52 mV, -52 mV vs. SCE, respectively) and the control pot (-55 mV vs SCE). There is no significantly measurable difference in the solution potential between the leaching and control pots. Such a negligible change in potential is predicted by the Nernst equation, as the dissolved uranium ion release into the solution is so small (10^{-9} mol/l).

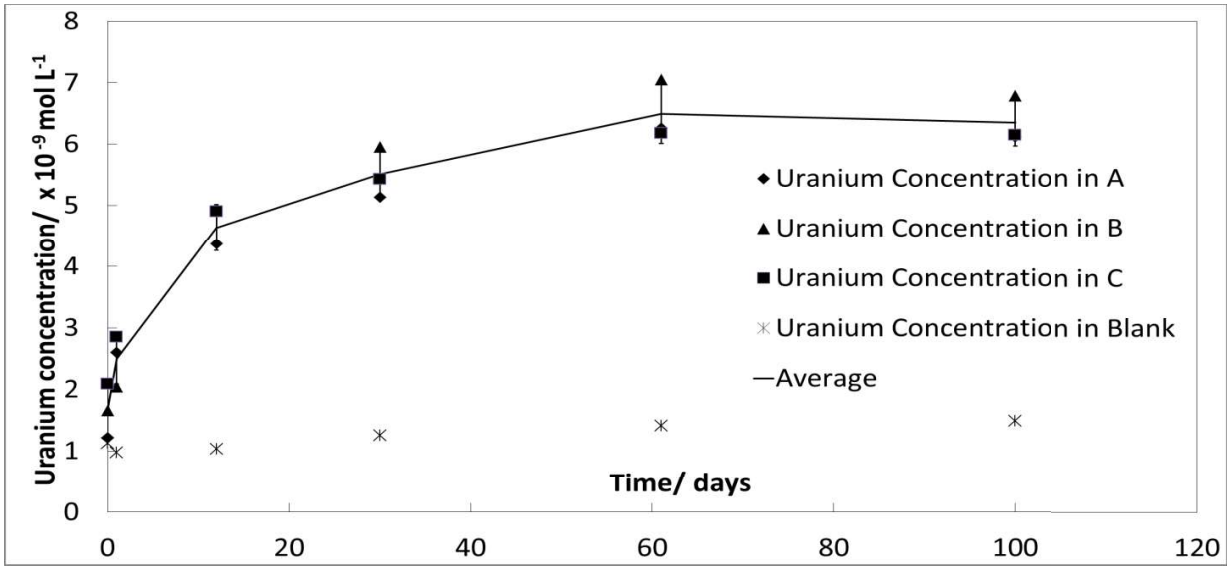

Fig. 13. Uranium concentration in aliquots obtained from three vessels, A, B and C

containing a uranium pellet each and a control vessel labelled as blank with the same set up without a uranium pellet.

The concentration of uranium reaches a maximum value of 6×10^{-9} mol/l after 60 days. This may be attributed to the uranium reaching its solubility limit under anoxic condition, hence there was a decrease in the driving force for further dissolution. Under such a scenario, reprecipitation can occur, which was confirmed by the detection of solid uranium precipitates when dissolved uranium was observed in the acid washout fraction after the experiment. This effect is more pronounced in the uranium concentration data of the thin film experiment discussed in Fig. 68 under Section 3.2. ICP-MS of acid washes of the vessels after completion of the dissolution experiment show a dissolved uranium concentration of ~3×10^{-9} mol/l in 250 cm^3 of 3 mol/l nitric acid, which is significantly higher than that in the blank pot (1×10^{-9} mol/l). Such an observation supports the presence of precipitated uranium phases within the dissolution vessel.

Fig. 24 shows the recorded open circuit potential of the uranium dioxide electrodes at the beginning and end of this experiment. These measurements indicate some evolution [15] of the oxidation state at the uranium dioxide surface. Referencing with a standard calomel electrode, Shoesmith and Sunder [15] reported potential readings between -150 to -270 mV for near stoichiometric uranium dioxide in argon-purged solutions, containing UO_{2+x}. This correlates reasonably well with our data with an average initial reading of -150 mV shown in Fig. 24. With increased oxidation of the uranium surface, Shoesmith and Sunder reported that the potential reading would increase correspondingly, and the region of oxidative dissolution occurs at a threshold

of -50 to -100 mV, where the surface composition approaches a thin layer (2–5 nm) of $UO_{2.33}$ as detected from angular-dependent XPS studies [33]. Our experimental reading reaches an average of -70 mV after 100 days of dissolution. We suspect that this might be due to oxidation arising from trace amount of ~2 ppm O_2 present in the glovebox atmosphere.

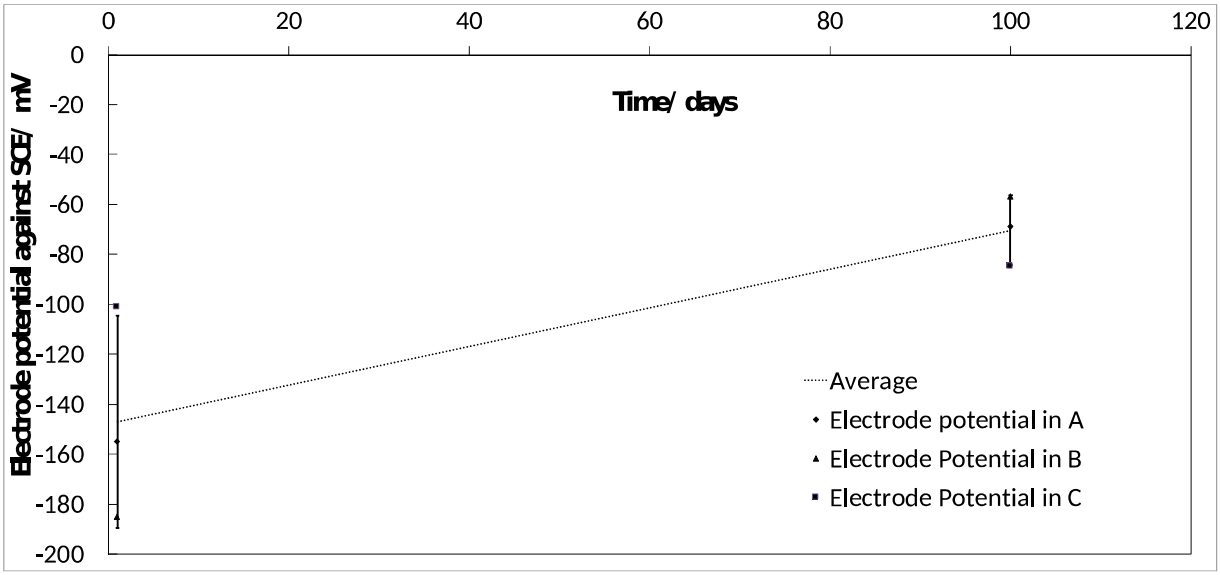

Fig. 24. Open circuit potential of the uranium dioxide electrodes recorded at the beginning and end of this leaching experiment. Note values are plotted vs. the standard calomel electrode (SCE) for ease of comparison with data from [15].

Area averaged Raman spectra of a freshly polished UO_2 electrode and three UO_2 electrodes after 100 days dissolution is shown in Fig. 35, which is a magnification of the Raman shift range 350 to 750 cm^{-1}, a region previously reported as being the most important with regards to the degree of oxidation of the UO_2 lattice [36,37]. It can be seen that there are two distinct differences between a freshly polished electrode and that leached in deionized water under anoxic conditions. Firstly, there is a decrease in

the large vibration at 440 cm^{-1}, although it should be noted that this intensity difference is only significant for Electrode C after accounting for the measurement's standard deviation as function of measured area. Secondly, there is a small increase in the broad band from ~550 to ~650 cm^{-1}.

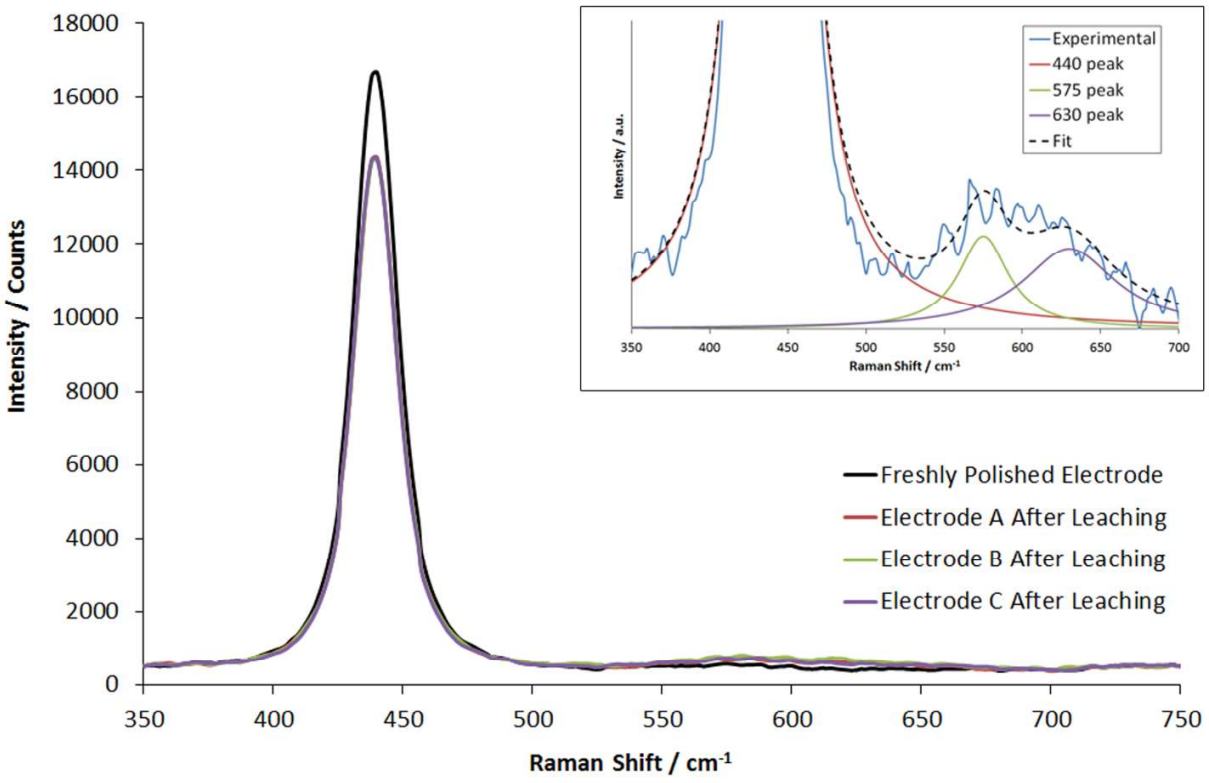

Fig. 35. Main: Linear baseline subtracted, area averaged Raman spectra of a freshly polished UO_2 electrode and three UO_2 electrodes after 100 days dissolution over the Raman shift range 350 to 750 cm^{-1}. Inset: Example Lorentzian fit of defect bands at 575 cm^{-1} and 630 cm^{-1} from a single measurement point from electrode A after leaching.

Considering the former 440 cm^{-1} vibration first, group theory predicts that a perfect fluorite structure would be expected to give a triply degenerate Raman active mode (T2g) [38], typically defined as the fundamental U-O symmetric stretching mode [11,39].

This intense vibration has been reported at ~445 cm^{-1} and in the UO_2 pellet samples of Fig. 35 is very close to this value at 440 cm^{-1}. A decrease in the intensity of this peak has been reported as being indicative of deviation from a perfect fluorite lattice structure, caused by either dopant effects or changes in UO_2 stoichiometry [37,39].

Turning now to the broad band from ~550 to ~650 cm^{-1}, this band has been ascribed to various vibrations that may occur as a result of increasing lattice defectiveness [37]. In the absence of dopants, this region is composed of three overlapping peaks at 550, 575 and 630 cm^{-1}, respectively. The peak at 550 cm^{-1} has only recently been considered and is tentatively assigned to UO_2 grain boundaries [36,40,41]. The other two peaks are of more interest with regards to the degree of oxidation of the leached samples. The first at 575 cm^{-1} has been assigned to a longitudinal optical (LO) phonon [37]. Usually, this phonon is forbidden under the selection rule imposed due to lattice symmetry, this peak can appear as a result of changes in translational symmetry at oxygen vacancy sites, leading to lattice disorder and the consequential breakdown in selection rules. These changes in symmetry are caused by either the incorporation of interstitial oxygens or dopant ions. The second peak at 630 cm^{-1} has been attributed to clustering of interstitial oxygens to form higher oxidation state cuboctahedrons associated with a transition to a defective U_4O_9 structure [42].

Thus, the ratio of either the 575 cm^{-1} or 624 cm^{-1} peak to the 440 cm^{-1} UO fundamental stretch is indicative of the degree of surface hyperstoichiometry (oxidation) of UO_2 [36]. In order to determine the contributions of each peak to the broad band of Fig. 35, a Lorentzian peak fit was performed for the data of Fig. 35, assuming peak maxima at 440, 575 and 630 cm^{-1}. An example fit for data from electrode A is shown in

Fig. 35 – inset. The results of this peak analysis expressed as a ratio to the 440 cm^{-1} peak are shown in Fig. 46A for the 575 cm^{-1} and Fig. 46B for the 630 cm^{-1} peak.

For both the 575 cm^{-1} and 630 cm^{-1} peak, there is a significant increase in surface oxidation heterogeneity as shown by the increase in result standard deviation after electrode leaching in deionized water. However, with the exception of the 575 cm^{-1} peak for Electrode B, the results show a significant increase in the 575/440 and 630/440 peak ratio after dissolution compared to a freshly polished electrode. This suggests there is an increase in the degree of surface oxidation of the electrodes after leaching for 100 days, corroborating the change in the measured open circuit potentials of the uranium dioxide electrodes discussed above. Finally, despite the observed increase in surface oxidation, no new peaks were observed in the region 800–830 cm^{-1} [28] in any of the acquired spectra, suggesting that there was no detectable highly-oxidised uranium dioxide (such as U_3O_8 and above) phases formed during the leaching process.

Scanning electron microscopy and EDX studies of the UO_2 electrode surfaces were carried out pre- (Fig. 57a) and post-dissolution (Fig. 57b) to ascertain the presence of any observable surface morphology changes or secondary phases.

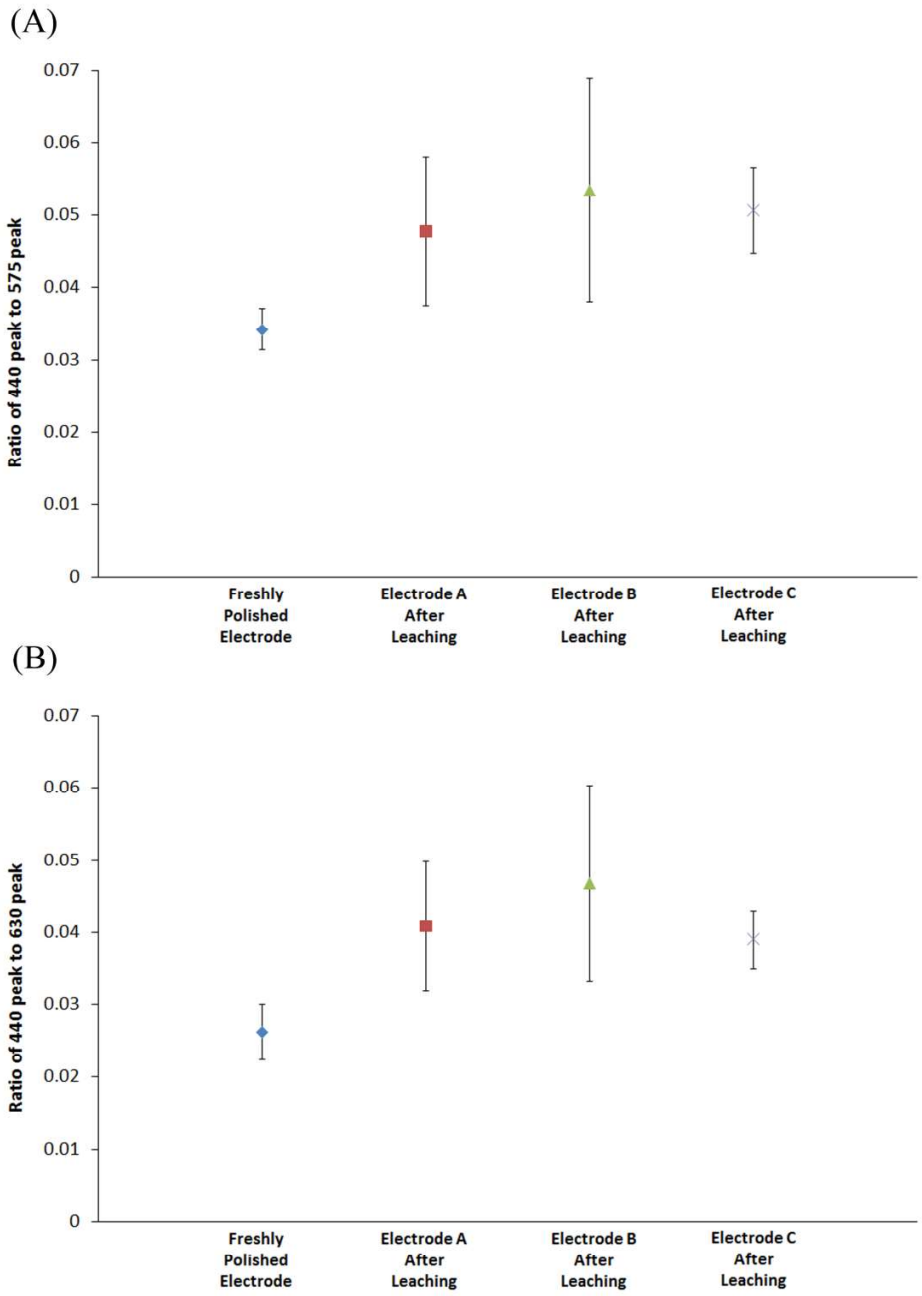

397

398 **Fig. 46.** Lorentzian peak fit results for the data of Fig. 35, assuming peak maxima at
399 440, 575 and 630 cm^{-1}. Results are expressed as a ratio of (A) the 575 cm^{-1} peak and
400 (B) the 630 cm^{-1} peak to the 440 cm^{-1} peak.

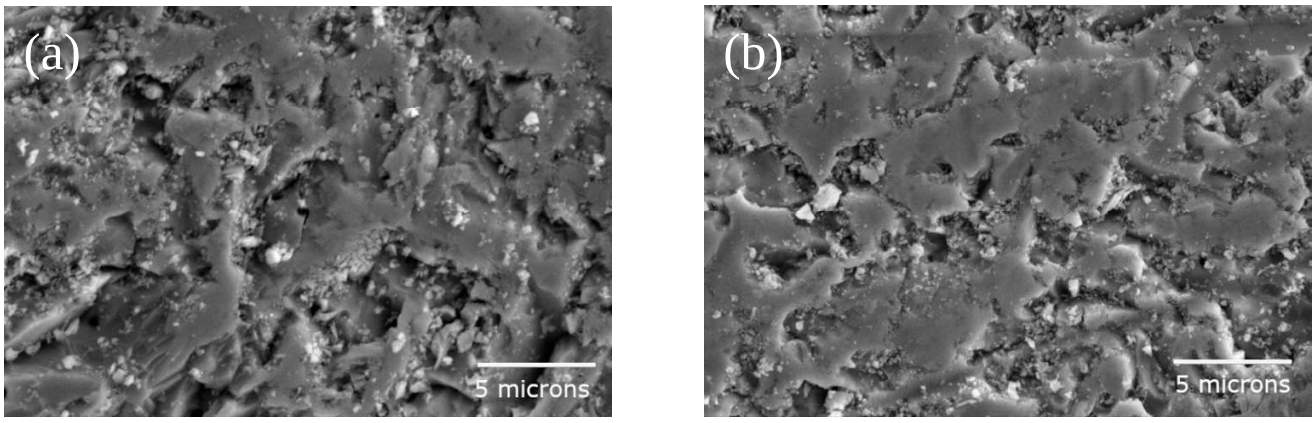

Fig 57. SEM at the surface of the (a) pre-leached UO_2 pellet after polishing and (b) the post-leached UO_2 pellet.

Comparison between Figs. 57a and Fig 57b reveals no significant differences before and after the leaching process. Furthermore, the high degree of surface roughness makes the identification of small secondary phases, such as those described for the thin film below, extremely difficult. However, comparison of the area EDX analysis of the electrodes before and after the leaching process reveals a small but measurable increase in oxygen atomic % from 45.71 (±0.23) to 46.44 (±0.35) where the uncertainties arose from the fitting. Again, this agrees with both Raman and open circuit potential measurements (see Figs. 35 and 46) that there is a small oxidation of the surface occurring due to a trace amount of ~2 ppm O_2 present in the glovebox atmosphere.

3.2. Thin film dissolution

A high-quality single-crystalline thin film (~100 nm) of UO_2 deposited on a (001) silicon single crystal substrate has been subjected to an extended anoxic dissolution test in

deoxygenated deionized water under anoxic argon (0.1 O_2 ppm) atmosphere at ambient temperature (~25 °C) [25].

The advantages of UO_2 thin film dissolution over pellets or powders is that the flat morphology of the film facilitates sharper focusing in surface imaging, allowing features that will have gone unnoticed in samples with rougher surfaces to be made more apparent.

ICP-MS measurements of both the uranium dissolution vessel and the silicon wafer only vessel as a function of time are shown in Fig. 6~~8~~.

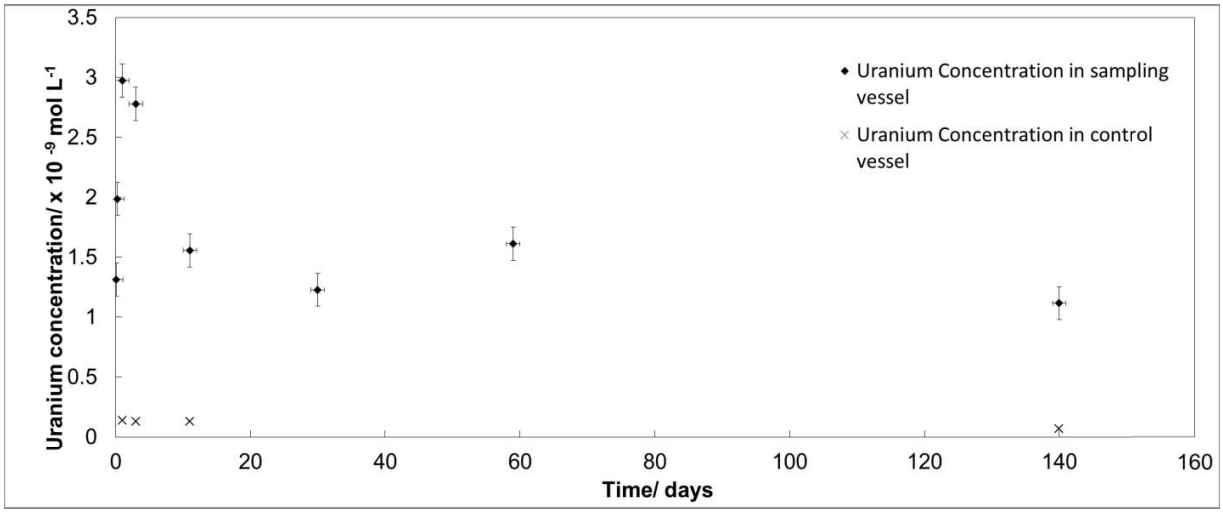

Fig. 6~~8~~. Dissolved uranium concentrations of extracted aliquots from both the uranium dioxide thin film dissolution vessel and the silicon wafer only vessel (control), determined by ICP-MS.

Fig. 6~~8~~ reveals uranium concentrations in the UO_2 thin film vessel are in the range of 1.2–3.0 × 10^{-9} mol/l. This is similar in order of magnitude to the uranium concentration from the pellet dissolution experiment shown in Fig. 1~~3~~. The initial increase in uranium

concentrations followed by a decrease and plateau concentration at >10 days dissolution time is again indicative of a secondary phase precipitation mechanism. The nature of such deposits is described in more detail in the following sections.

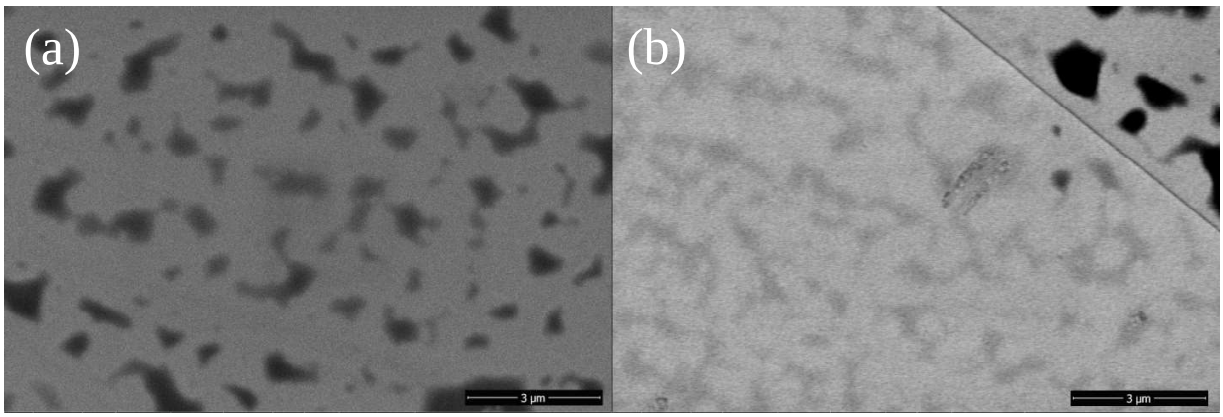

Fig. 7~~9~~. (a) 30000× magnified secondary electron and (b) backscattered electron micrographs of the thin film before prewash and heat treatment.

From the pre-leaching SEM micrographs of Fig. 7~~9~~, the surface is generally smooth with some trace particulates. Backscattered atomic contrast electron images (not shown) reveal that the particles are significantly darker than the uranium surface, i.e. they have a significantly lower atomic number, suggesting they are not uranium dioxide particles. A likely cause is carbon particles from the carbon tape used in the mounting.

Post-leach SEM images of a UO_2 thin film exposed to anoxic deionized water are shown in Figs. 8~~10~~ and 9~~11~~.

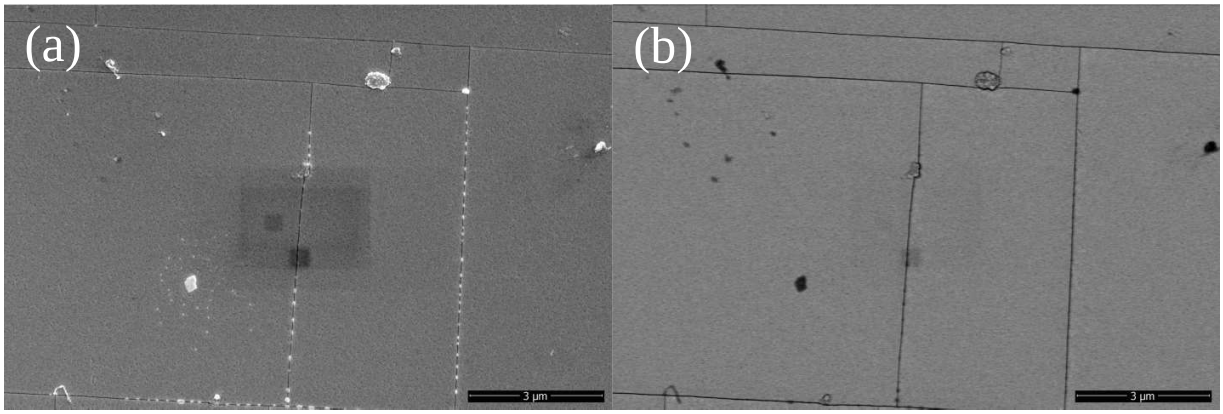

Fig. 8~~10~~. (a) 30000× magnified secondary electron and (b) backscattered electron micrographs of the leached thin film surface after 140 days dissolution.

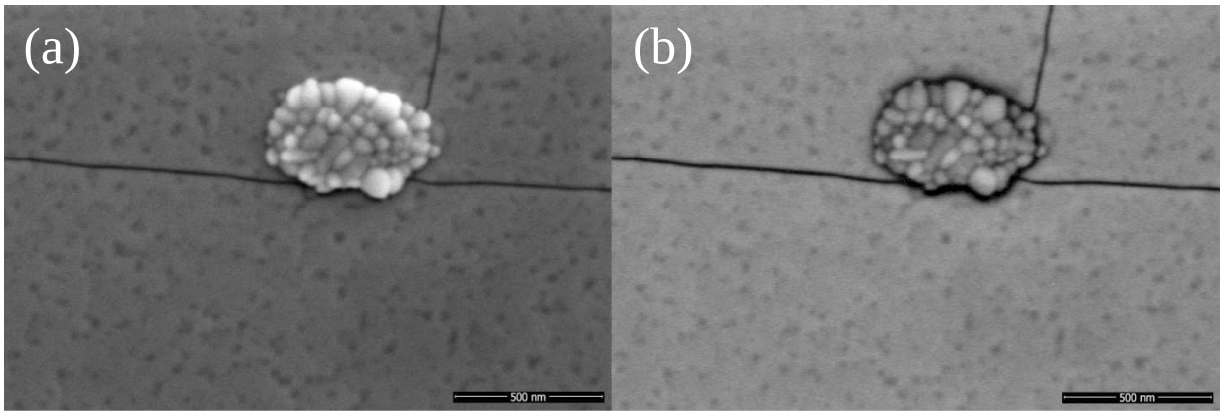

Fig. 9~~11~~. (a) 200,000× magnification secondary electron and (b) backscattered electron micrographs on the nucleate with clear growth domains ranging between 20-100 nm [25].

From Figs. 8~~10~~ and 9~~11~~, there are three main differences that can be seen between pre and post leaching. First, more cracks are observed. These cracks are likely due to the relaxation of the stress between the substrate and thin film during the dissolution process. Both structures are based on the face centred cubic structure with slight differences in the lattice parameters, the uranium dioxide (fluorite type lattice) thin

film and the underlying silicon (diamond type lattice) substrate having lattice parameters of 5.47 Å [43] and 5.43 Å [44], respectively.

Secondly, high magnification images at 200,000× magnification (Fig. 9~~11~~) enable the identification of small pits (20–100 nm) where dissolution has occurred. Based on previous studies, dissolution is known to initiate at energetically reactive sites [45] such as point defects, dislocations terminating at the surface and so forth [46–48]. Lastly, Fig. 9~~11~~ reveal the presence of circular (d = 20–100 nm) secondary phase formations preferentially nucleated at film cracks. The backscattered electron image in Fig. 9~~11~~b shows that the nucleated phases have almost the same contrast as the rest of the film, which implies similarity in composition. Unfortunately, due to the small size of the individual grains a reliable EDX analysis could not be carried out to obtain compositional information on the secondary phase.

SEM imaging was also conducted on the silicon substrates in the same vessel as the UO_2 thin film, with secondary and backscattered electron images shown in Fig. 10~~2~~.

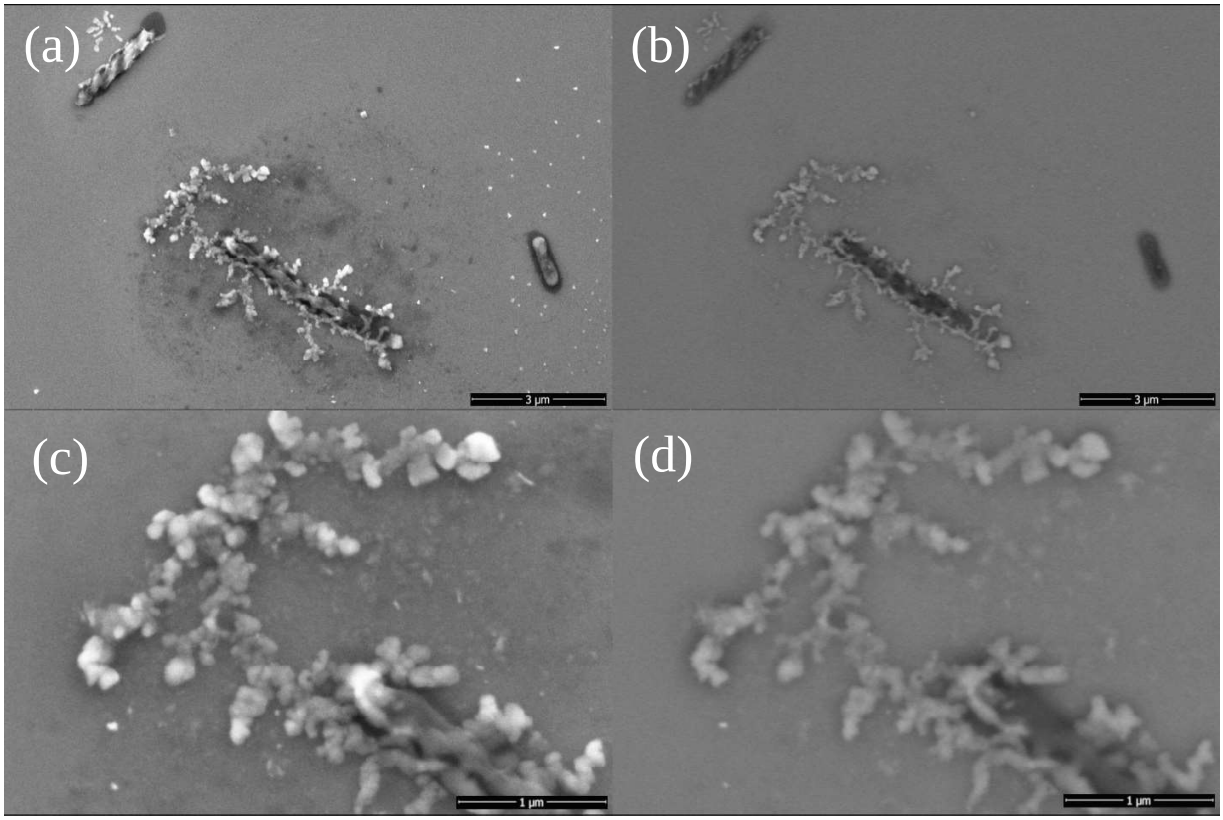

Fig. 102. Secondary (a) and backscattered electron (b) micrographs of secondary precipitates detected at 30, 000× and secondary (c) and backscattered electron (d) micrographs of secondary precipitates detected on blank silicon substrates at 100, 000× magnifications.

Fig. 102 shows some precipitates present on the silicon surface. Back-scattered electron image, Fig. 102b and Fig. 102d show that the precipitates contrasted significantly against the silicon substrate suggesting the precipitates have higher atomic numbers. Considering the closed system of deionized water, silicon substrates and uranium thin film, this implies that uranium precipitates are not just a local phenomenon found at the uranium thin film surface. However, the mechanism of precipitation is postulated to be different.

The precipitates formed on the silicon substrates differ significantly from the precipitates formed on the UO_2 thin film in terms of topography and morphology. On the flat silicon substrate, Fig. 102 shows clearly the presence of two types of precipitates, randomly scattered particles and dendritic precipitates at the dissolution trenches and pits, appearing as agglomerates of many grains (~50 nm) with different heights. Both these precipitates have distinctly different morphologies from those formed on the uranium thin film. Spherical UO_2 colloids have previously been reported in oxygen-starved dissolution of uranium dioxide [49]. We believe the scattered particles might be formed from colloidal agglomeration and~~colloidal~~ precipitation [50] from dissolved uranium in the solution and the dendritic growth are uranium secondary phases formed after interaction with the silicon substrate at dissolution pits/trenches.

Despite the low ionic strength of deionized water contributing to a large kinetic barrier against aggregation [51], the gravitational force on the colloids coupled with the large difference in density between the dense uranium colloids and the surrounding fluid resulted in their precipitation after formation. Neglecting Brownian motion, Fig. 113 shows the relationship of colloidal size to settling time using sedimentation velocity calculation based on the Stokes' equation where sedimentation velocity $=$

$$\frac{g\left(\rho_{UO_2}-\rho_f\right)(d_{UO_2})2}{18\mu_f} \qquad (4)$$

where g represents the gravitational acceleration experienced by the colloid, ρ_{UO_2} represents the density of uranium dioxide, ρ_f represents the density of fluid (water), d_{UO_2} represents the diameter of uranium dioxide colloids and μ_f stands for the dynamic viscosity of water.

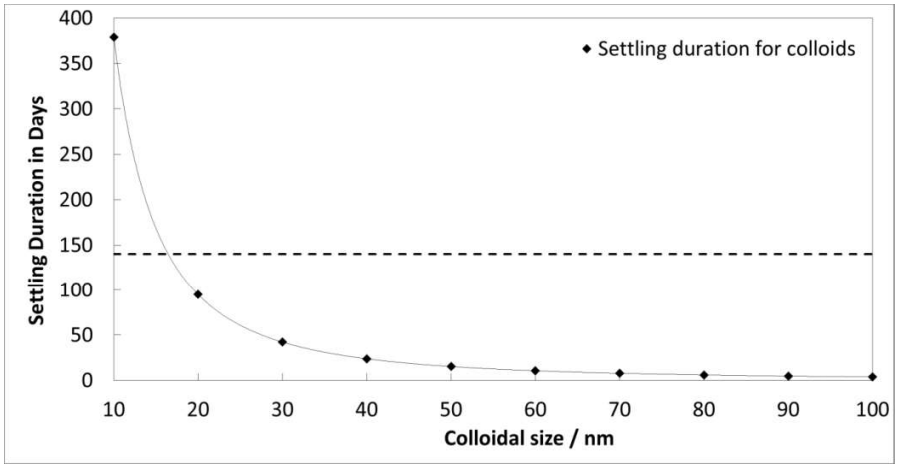

Fig. 113. Stokes' equation predicts the relationship between the settling/sedimentation duration against colloidal size for colloidal precipitation in 2 cm deep leaching vessel, similar to our set-up.

For 140 days experiments, colloid precipitation is seen to have a colloidal size limit at 15 nm. Smaller colloids will take a much longer time to settle. The velocity of sedimentation was calculated to be 1.53×10^{-8} ms^{-1} for the observed ~50 nm uranium dioxide colloids, achieving sedimentation after 2 cm descent (depth in our experiment) in ~14 days.

To identify the precipitates, EBSD, EDX and XRD were attempted but no signals were detected that allowed differentiation from the underlying UO_2 thin film. The lack of elemental analysis opens up possible alternative interpretations for these colloids to be uranium silicates, such as coffinite. Given the high~~high~~ solution concentration of silicon ions (25 ppb or 10^{-6} mol/l Si from ICP-AES measurement of the solution after the experiment ~~which is close to the 10^{-6} mol/l~~), these colloids are possibly ~~unlikely to be~~ uranium silicate colloids ~~although it is possible that uranium silicate colloids may~~

~~have~~that have been formed in the near field of the silicon substrate at near neutral pH [52] if there is super saturation of silicon ions of a few orders of magnitude. Our concentrations of silicate to uranium concentration is quite close to that reported in the dissolution of coffinite by S~~, but this seems unlikely with the low concentration of dissolved silicon ions in the solution.~~zenknect et al [53]. The only caveat to this interpretation is the difficulty in producing coffinite at room temperature in laboratory conditions [6,52,53] where the concentration of silicon is higher than our measured silicon concentrations at 10^{-4} mol/ l. It is however possible that the precipitates might be precursors of coffinite.

The distinct morphology of the dendritic formation implies a different secondary phase from that observed at the uranium thin film. From the sharp contrast from the underlying silicon substrate at Fig. 102d, these grains may be preferential uranium precipitation in the dissolution trenches/pits where super saturation of silicon ions is possible and uranium secondary phases containing silicon, potentially uranium silicates are formed.

X-ray diffraction analysis of the uranium thin film in standard Bragg-Brentano geometry is shown in Fig. 124. Unfortunately, the diffractogram of Fig. 124 does not show any signal from any secondary phases that may be present, most likely due to the low amount of material present versus the bulk UO_2 film.

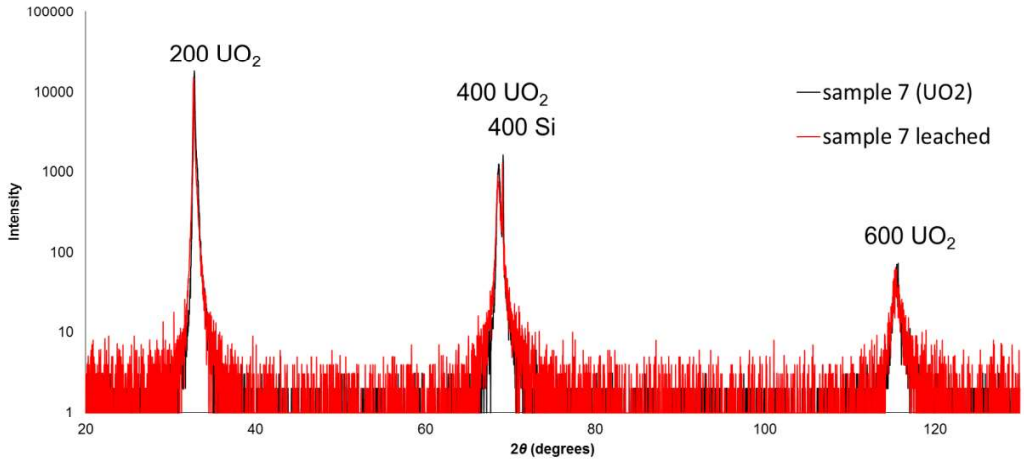

Fig. 124. XRD diffractogram for the pre-leached and post-leached UO_2 thin film sample on a silicon substrate. Only 200, 400, and 600 UO_2 reflections corresponding to the (001) crystallographic orientation are present.

Neck and Kim [21] proposed that for actinides in neutral and alkaline solutions, where $An(OH)_{4(aq)}$ are the predominant aqueous species, the solubilities of $AnO_{2(cr)}$ become equal to those of the amorphous solids. Hence, a conclusion was drawn that the crystalline dioxides are covered by amorphous hydroxide layers. Despite this, from X-ray diffraction of the pre and post-leached thin film samples (Fig. 124) and surface sensitive EBSD measurements (Fig. 146), we found that the sample of UO_2 did not amorphize during the dissolution duration of 140 days.

Finally, we observe that dissolution of the uranium dioxide thin film led to micro-crack formations seen in Figs. 810 and 911. We postulate this to result from the release of film strain due to lattice-mismatch between the uranium dioxide thin film and the underlying silicon substrate. We investigated carefully the misorientation differences between each

point of the thin film surface with the help of EBSD images. MTEX, a MATLAB toolbox for quantitative texture analysis, was used to quantify the misorientation differences between individual points on the thin film to investigate this dissolution-assisted strain release micro-cracks formation in the compressively stressed thin film. Such crack formation in thin films under tensile stress has been simulated by Zhang et al [54]. These micro-cracks are distinct from previously observed, oxidative cracks [55] as we have no evidence of oxidation of UO_2 to U_3O_7 from our XRD data.

A thresholded EBSD map, Fig. 1~~3~~5, shows that the crystal orientation is constant throughout the grain, with virtually the entire area within 1 degree of misorientation. Next, subgrain boundaries were defined with the fast multiscale clustering (FMC) method [56] with a scaling parameter for grouping and segregating pixels into subgrains, (C_Maha of 4.8). Fig. 1~~3~~5 shows the subgrain features found reflect the crack morphology. By fitting a misorientation profile with a third order polynomial function we calculated a precision error (3sigma) smaller than ± 0.3° (see Electronic Supplementary Information (ESI)).

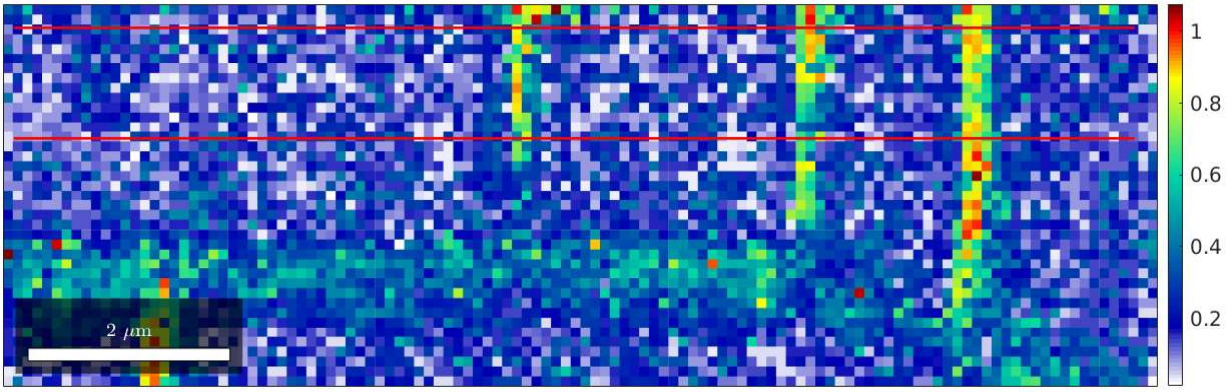

Fig. 135. Thresholded EBSD map showing the misorientation angle of every pixel with respect to the average orientation. The twelve adjacent misorientation profiles delimited by the two red curves were averaged to obtain the averaged misorientation profile of Figure 146.

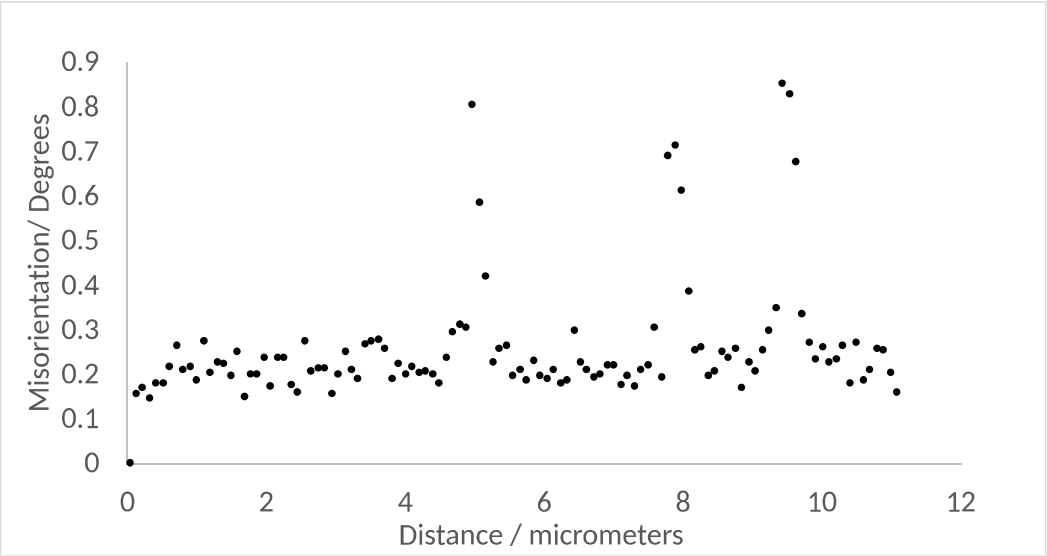

Fig. 146. Averaged misorientation profile (see Fig. 15 as a reference)

The resolution of each square pixel shown in Fig. 135 is 97 nm by 97 nm. Vertical grains with areas of two by ten pixels left and right of each crack were merged and their average misorientation axes were calculated with respect to the immediate adjacent areas to the left. These misorientation axes are plotted in the inverse pole figure shown in Fig 157. Our data show that the misorientation axis looks relatively similar at both flanks of the cracks. With our averaging approach, we have been able to show that the misorientation axes oscillate around <111>, which is the cleavage related direction expected for a cubic fluorite structure [57]. Our interpretation is that due to the lattice mismatch between the UO_2 and the silicon substrate crystal structures, the oxide

structure is distorted along the <111> cleavage directions throughout the entire thin film. This distortion becomes experimentally significant (i.e. larger than 0.3 º) at the proximity of the cracks: that is, the crack allows for a larger crystal distortion. Such distortion promotes further propagation of the cracks themselves in a positive feedback loop. This can be seen from Fig. 8~~10~~ where the cracks are seen at 90º to each other, implying a <111> direction of propagation in this (001) oriented uranium dioxide thin film.

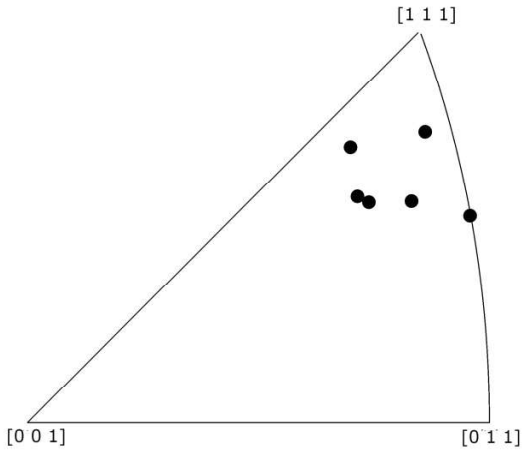

Fig. 1~~5~~~~7~~. Plot of misorientation axes obtained on either side of the three cracks. They have similar misorientation axis with some statistical variation.

3.3. Powder samples

This last experiment aims to determine the effect of temperature on uranium dioxide dissolution. High surface area uranium dioxide powder was leached under varying temperatures to determine the effect of temperature on uranium dioxide dissolution. ~~These high temperatures, high surface area uranium dioxide powder experiments were designed to maximise the concentration of dissolved uranium ions with the backdrop of low concentration of dissolved uranium dioxide ions observed in both the solid pellet~~

~~and thin film experiments.~~ ICP-MS determined uranium solution concentration values from the UO_2 powder leaching vessels held at different temperatures (ambient temperature (~25˚C), 40 ˚C, 90 ˚C and 150 ˚C) are shown in Fig. 1~~6~~8. It should be noted that the aliquot extraction was done at the ambient glovebox temperature of 25˚C.

From Fig. 1~~6~~8, it can be seen that the concentration of dissolved uranium does not vary significantly despite the different temperatures employed. In fact, the mean U concentration appears to decrease from 40 ˚C to 150 ˚C. It should be noted that the aliquot extraction was done a few minutes after removing the samples from the autoclave and temperatures may have fallen slightly. This observation indicates that increased temperatures do not increase dissolved uranium concentrations for long duration dissolution. It can again be seen that the final concentrations are ~10^{-9} mol/l consistent with our results on the thin film and bulk dissolution experiments at ambient temperature.

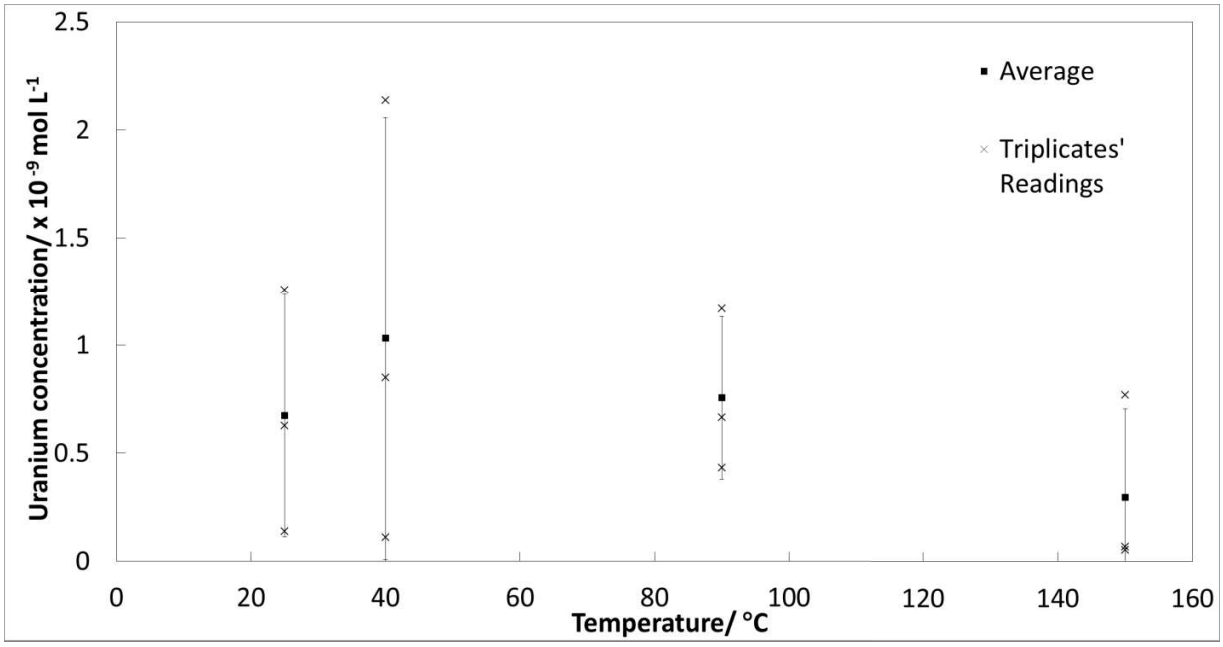

Fig. 168. ICP-MS determined uranium concentration values after 390 days of dissolution at temperatures from 25 to 140 ˚C.

4. Discussion

4.1. Simulations

Phreeqc 3.4.0-13927 [58] calculates the equilibrium concentration of ions for a given combination of reactants in solution after inputting initial conditions, such as solubility, pH, Eh, concentration of dissolved oxygen and so forth. Using a referenced thermodynamic database, such as Hatches [59], we estimated the equilibrium concentration of dissolved uranium ions by integrating the different speciation of uranium (IV, V, VI) at different concentrations of dissolved oxygen using existing solubility and reaction parameters for UO_2 from the Nuclear Energy Authority (NEA) database.

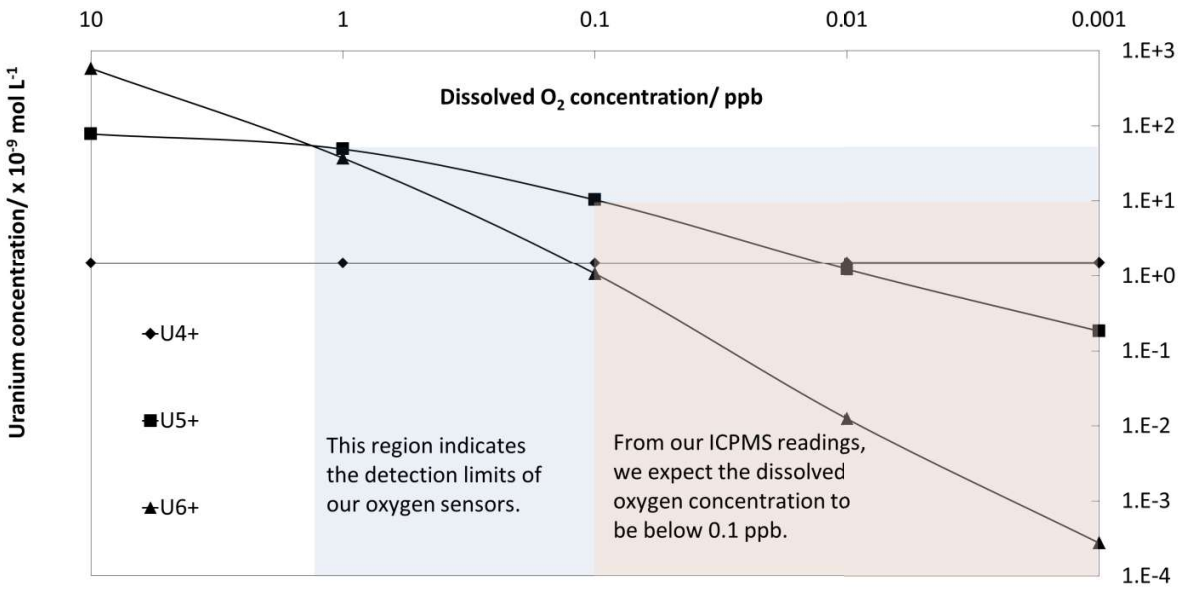

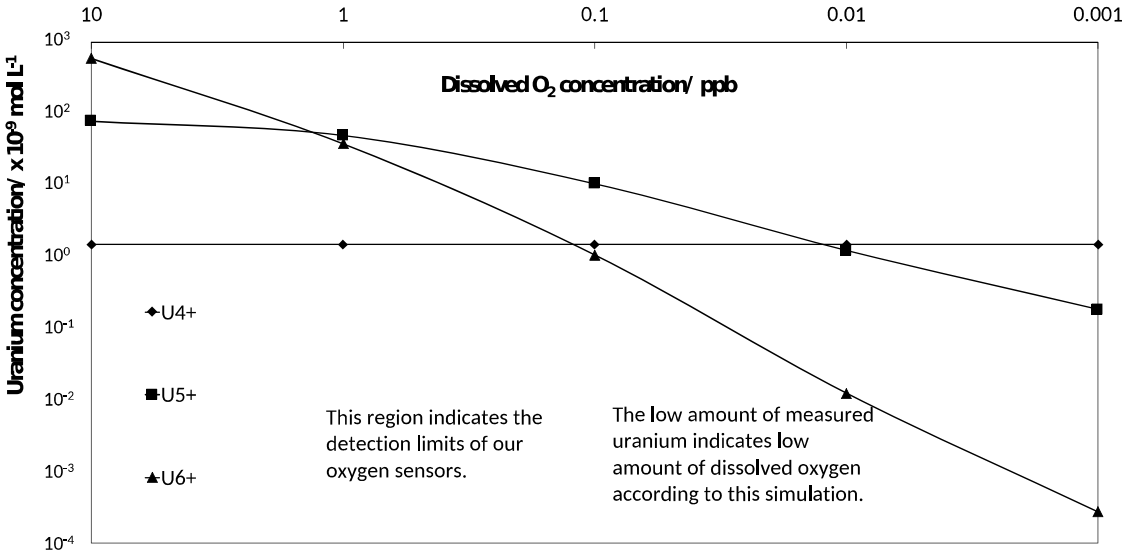

634

635 **Fig. 179.** Phreeqc simulation of dissolved uranium concentration at equilibrium as a
636 function of oxygen content for UO_2 (NEA) dissolution in deionized water at room
637 temperature, where log $K^0 = 54.5 \pm 1.0$.

638 Given a starting condition of stoichiometric tetravalent uranium dioxide, oxidation of
639 uranium dioxide, U(IV)O_2 to U^{5+} and U^{6+} are dominant in solution at concentrations of
640 dissolved oxygen above 0.1 ppb. Based on the highest dissolved uranium concentration
641 readings in all our experiments (see Fig. 13) of about 6×10^{-9} mol/L, we can relate that
642 the upper limit of dissolved oxygen in our system is about 0.1 ppb.

643 Simulations show constant equilibrium concentration of tetravalent uranium at these
644 lowall levels of dissolved oxygen indicating that anoxic dissolution of uranium dioxide in
645 its tetravalent form proceeds invariably at a limiting rate due to low associated solubility
646 and such tetravalent dissolution becomes dominant at low levels of dissolved oxygen for
647 stoichiometric uranium dioxide where oxidation of uranium dioxide to higher oxidation

levels is seen to drop off sharply according to these thermodynamic calculations.

4.2. Experimental discussions

There is some variability in reported uranium concentrations for the anoxic dissolution of uranium dioxide, ranging from 10^{-7} mol/L to 10^{-10} mol/L [21] and these have been noted by NEA [60] to result from a range of solids with different thermodynamic stabilities. The common theme from the results of this series of experiments, with different physical forms of UO_2, is that the dissolved uranium concentration is ~10^{-9} mol/l and in all cases less than 10^{-8} mol/l, for all physical forms when care is taken to control the oxygen content of the water and therefore oxidation potential of the water. Thermodynamic calculations indicate that concentrations in this range represent the solubility limit of uranium in its tetravalent oxidation state.

For the first time, well-defined growth of precipitates at low uranium concentration was observed [25]. This contradicts the notion of an oxidative dissolution mechanism for U with it transforming to hexavalent form prior to dissolution, as U^{6+} has solubility limits (~10^{-6} mol/l) [3] that are 3 orders of magnitude higher than the U concentration values observed (~10^{-9} mol/l). This difference in solubilities is also observed with anoxic dissolution as ICP-MS results from pre-washes are noted to contain a higher concentration of uranium, which we attribute to preferential dissolution of U^{5+} and U^{6+} in slightly oxidized uranium dioxide.

The low concentration of dissolved uranium ions and the high solubility of hexavalent uranium implies that no secondary phase formation should take place at this concentration if dissolution was going through the hexavalent pathway. Hence, the

observation of these uranium precipitates leads us to conclude that anoxic dissolution of uranium must proceed through the tetravalent phase.

We put forward that the anoxic dissolution of stoichiometric uranium over time is made up of two simultaneous and competing processes:

1) A widely-accepted mechanism [3] dissolved oxygen-dependent transformation of $U(IV)_{(solid)}$ to $U(V,VI)_{(solid)}$ then $U(VI)_{(aqueous)}$,

This will lead to $U(VI)_{(precipitates)}$ at a high concentration of dissolved uranium ions at its solubility limit, as in the case of oxic dissolution.

We observe a small amount of transformation of uranium to higher oxidation states indirectly through the increase in oxygen levels with EDX at the surface of our solid pellet electrode dissolution experiments and from Raman evidence of higher numbers of interstitial oxygens in leached samples, but not a significant increase in the dissolved uranium concentration.

2) A proposed non-oxygen dependent [25] $U(IV)_{(solid)}$ to $U(IV)_{(aqueous)}$ then $U(IV)_{(precipitates)}$

process 2 has been demonstrated to prevail in our sets of anoxic experiments and thus has significance in real-life nuclear repositories which are expected be anoxic [2].

From the solid pellet experiment, it can be concluded that in anoxic dissolution with low levels of oxygen at 2.0 ppm O_2, it is still possible to observe surface oxidation indirectly from Raman spectroscopy inferences, open circuit potential and EDX

690 measurements. Despite this, the dissolved uranium concentration remains low at 6 × 10-
691 9 mol/l, which is an indication that mainly tetravalent uranium ions are present in solution
692 with their characteristic low solubility. However, with pellet studies the higher surface
693 roughness inhibits clear observations of any secondary phases that may be formed.
694 Nevertheless, we have observed from ICP-MS results of the acid post-washes of the
695 leaching vessel, an average of 3 × 10^{-9} mol/l of dissolved uranium in 250 cm^3 of 3.0 M
696 nitric acid. This highlights the presence of uranium sorption/precipitation on the wall of
697 the PTFE vessels as observed before [10,61].

698 Considering an accidental container corrosion scenario of 500-1000 years when
699 container will fail to be water tight and groundwater ingresses, the temperature of spent
700 nuclear fuel interacting with groundwater will be higher than the prevailing underground
701 repository temperatures depending on the fuel burn-up and the waste canisters. Thus,
702 temperatures in the vicinity of the spent nuclear fuel will vary from ~45 ºC to ~130 ºC
703 [62].

704 High-surface area powder dissolution conducted at elevated temperatures for 390
705 days showed uranium concentrations falling within a range between 0.1 × 10^{-9} to
706 2 × 10^{-9} mol/l. We notice a slight decrease in the mean dissolved uranium
707 concentrations at higher temperatures, albeit within the error bars. Although, it should
708 be noted that the aliquot extraction was performed at an ambient glove box temperature
709 of ~25 °C.

710 Slightly higher concentration of dissolved uranium concentrations in the solid pellet
711 experiment (6.0 × 10^{-9} mol/l) might be attributed to a thin layer of higher oxidized

712 uranium on its surface as these samples were not annealed in a reducing environment
713 like the others with values of about 3.0 × 10^{-9} mol/l. Since the uranium concentration
714 values in the contact solutions were essentially of the same order of magnitude (~10^{-9}
715 mol/l) for the pellet, thin film and powder samples, and formation of a uranium
716 containing secondary phase took place, it can be suggested that the equilibrium
717 uranium concentration in the solution is limited by the solubility of the nucleating
718 secondary phase and is independent of the UO_2 form (bulk pellet, thin film or powder).
719 Just as schoepite's solubility [35] forms the upper limit of uranium dissolution in oxic
720 conditions, the limitation of uranium dioxide dissolution in anoxic conditions will be
721 limited by solubility of these uranium (IV) secondary nucleates. Hence, parameters such
722 as specific surface area, density of reactive surface sites, particle sizes and sample
723 crystallinity (amorphous vs. crystalline) should not affect the uranium concentration
724 established in the solution in the long-term and may only affect the kinetic aspects of the
725 process [63].

726 **5. Conclusions**

727 For extended durations up to 390 days, we conclude that the baseline scenario of
728 uranium dioxide dissolution in deionized water will result in dissolved uranium dioxide
729 concentration of the order of 10^{-9} mol/l, which is indicative of U^{4+} dissolution. Relatively
730 slight variation in uranium concentrations of less than one order of magnitude is
731 observed between different sets of UO_2 samples (pellets, thin film and powder).
732 Variable temperature dissolution was conducted over a duration of 390 days and the
733 concentration of dissolved uranium did not increase with elevated temperatures.

The dissolved uranium concentration of these long-term anoxic uranium dissolution experiments went through a maximum before decreasing to a constant value being indicative of a dissolution and precipitation mechanism, which is verified by the observed uranium containing secondary phases. At such low dissolved uranium concentration, dissolution and precipitation of uranium is hypothesized to proceed through the tetravalent form. This hypothesis is reinforced by clear observations of clusters (~500 nm) of homogenous uranium-containing precipitates of 20–100 nm grains in the thin film dissolution experiment.

From these experiments, we conclude that anoxic uranium dissolution with deionized water proceeds in 2 forms simultaneously at the surface.

1) a dissolved oxygen-dependent step of $U(IV)_{(solid)}$ to $U(V, VI)_{(solid)}$ then $U(VI)_{(aqueous)}$

2) a non oxygen-dependent $U(IV)_{(solid)}$ to $U(IV)_{(aqueous)}$ process to $U(IV)_{(precipitates)}$

We proposed that the equation for process 2 will take the following form:

$$UO_{2(s,\ \text{defective})} + 2H_2O_{(l)} \rightarrow U(OH)_{4(aqueous)} \rightleftharpoons UO_{2(s,\ \text{less defective})} + 2H_2O_{(l)},\ \Delta H < 0 \quad (5)$$

Acknowledgements

We would like to acknowledge the Singapore Nuclear Research and Safety Initiative for partial funding. We would also like to acknowledge Thomas Gouder, Rachel Eloirdi, Alice Seibert from the European Commission, Joint Research Centre, Directorate for Nuclear Safety and Security for providing the thin film sample. Lastly, we will also like to

757 express our thanks for being able to use the UTGARD National Nuclear User Facility
758 (NNUF) for some of our experiments.

759 **Conflicts of interests**

760 There are no conflicts of interests to declare.

761

762 **Data Availability**

763 The raw/processed data required to reproduce these findings cannot be shared at this
764 time as the data also forms part of an ongoing study. However, additional information on
765 EBSD data processing has been included in the electronic supplementary information.

766 **References**

767 [1] MIT, The Future of the Nuclear Fuel Cycle, 2011.
768 http://medcontent.metapress.com/index/A65RM03P4874243N.pdf%0Ahttps://mite
769 i.mit.edu/system/files/The_Nuclear_Fuel_Cycle-all.pdf.

770 [2] D. Cui, E. Ekeroth, P. Fors, K. Spahiu, The Interaction of Dissolved Hydrogen with
771 Spent Fuel or UO2 Doped with Alpha, in: Mater. Res. Soc. Symp. Proc., 2008.

772 [3] D.W. Shoesmith, Fuel corrosion processes under waste disposal conditions, J.
773 Nucl. Mater. 282 (2000) 1–31. doi:10.1016/S0022-3115(00)00392-5.

774 [4] H. He, M. Broczkowski, K.O. Neil, D. Ofori, D. Shoesmith, Corrosion of nuclear
775 fuel (UO2) inside a failed nuclear waste container | NWMO TR-2012-09, 2012.

776 [5] K. Ollila, M. Olin, M. Lipponen, Solubility and Oxidation State of Uranium under
777 Anoxic Conditions (N 2 Atmosphere), Radiochim. Acta. 74 (1996) 9–13.
778 https://www.degruyter.com/downloadpdf/j/ract.1996.74.issue-

s1/ract.1996.74.special-issue.9/ract.1996.74.special-issue.9.pdf.

[6] M. Amme, T. Wiss, H. Thiele, P. Boulet, H. Lang, Uranium secondary phase formation during anoxic hydrothermal leaching processes of UO2 nuclear fuel, J. Nucl. Mater. 341 (2005) 209–223. doi:10.1016/j.jnucmat.2005.02.004.

[7] T. Mennecart, B. Grambow, M. Fattahi, Z. Andriambololona, Effect of alpha radiolysis on doped UO2 dissolution under reducing conditions, Radiochim. Acta. 92 (2004) 611–615. doi:10.1524/ract.92.9.611.55010.

[8] J. Bruno, I. Casas, I. Puigdomènech, UO 2 under reducing conditions and the influence of an oxidized surface layer (UO 2+ x): Application of a continuous flow-through reactor, Geochim. Cosmochim. Acta. 55 (1991) 647–658. doi:10.1016/0016-7037(91)90330-8.

[9] A.J. Popel, V.G. Petrov, V.A. Lebedev, J. Day, S.N. Kalmykov, R. Springell, T.B. Scott, I. Farnan, The effect of fission-energy Xe ion irradiation on dissolution of UO2 thin films, J. Alloys Compd. 721 (2017) 586–592. doi:10.1016/j.jallcom.2017.05.084.

[10] A.J. Popel, T.W. Wietsma, M.H. Engelhard, A.S. Lea, O. Qafoku, C. Grygiel, I. Monnet, E.S. Ilton, M.E. Bowden, I. Farnan, The effect of ion irradiation on the dissolution of UO2 and UO2-based simulant fuel, J. Alloys Compd. 735 (2018) 1350–1356. doi:10.1016/j.jallcom.2017.11.216.

[11] H. He, Z. Qin, D.W. Shoesmith, Characterizing the relationship between hyperstoichiometry, defect structure and local corrosion kinetics of uranium

800 dioxide, Electrochim. Acta. 56 (2010) 53–60. doi:10.1016/j.electacta.2010.09.064.

801 [12] D. Serrano-Purroy, F. Clarens, E. González-Robles, J.P. Glatz, D.H. Wegen, J.
802 De Pablo, I. Casas, J. Giménez, A. Martínez-Esparza, Instant release fraction and
803 matrix release of high burn-up UO2spent nuclear fuel: Effect of high burn-up
804 structure and leaching solution composition, J. Nucl. Mater. 427 (2012) 249–258.
805 doi:10.1016/j.jnucmat.2012.04.036.

806 [13] K. Lemmens, E. González-Robles, B. Kienzler, E. Curti, D. Serrano-Purroy, R.
807 Sureda, A. Martínez-Torrents, O. Roth, E. Slonszki, T. Mennecart, I. Günther-
808 Leopold, Z. Hózer, Instant release of fission products in leaching experiments with
809 high burn-up nuclear fuels in the framework of the Euratom project FIRST-
810 Nuclides, J. Nucl. Mater. 484 (2017) 307–323. doi:10.1016/j.jnucmat.2016.10.048.

811 [14] K.U. Ulrich, E.S. Ilton, H. Veeramani, J.O. Sharp, R. Bernier-Latmani, E.J.
812 Schofield, J.R. Bargar, D.E. Giammar, Comparative dissolution kinetics of
813 biogenic and chemogenic uraninite under oxidizing conditions in the presence of
814 carbonate, Geochim. Cosmochim. Acta. 73 (2009) 6065–6083.
815 doi:10.1016/j.gca.2009.07.012.

816 [15] D.W. Shoesmith, S. Sunder, The prediction of nuclear fuel (UO2) dissolution rates
817 under waste disposal conditions, J. Nucl. Mater. 190 (1992) 20–35.
818 doi:10.1016/0022-3115(92)90072-S.

819 [16] M. Altmaier, E. Yalçıntaş, X. Gaona, V. Neck, R. Müller, M. Schlieker, T.
820 Fanghänel, Solubility of U(VI) in chloride solutions. I. The stable

821 oxides/hydroxides in NaCl systems, solubility products, hydrolysis constants and
822 SIT coefficients, J. Chem. Thermodyn. 114 (2017) 2–13.
823 doi:10.1016/j.jct.2017.05.039.

824 [17] M. Pijolat, C. Brun, F. Valdivieso, M. Soustelle, Reduction of uranium oxide U3O8
825 to UO2 by hydrogen, Solid State Ionics. 101–103 (1997) 931–935.
826 doi:10.1016/S0167-2738(97)00385-8.

827 [18] G. Leinders, Low-Temperature Oxidation of Fine Uo 2 Powders: Thermochemistry
828 and Kinetics, Inorg. Chem. 9 (2018) 2–10. doi:10.1021/acs.inorgchem.8b00517.

829 [19] B.J.S. Anderson, L.E.J. Roberts, E.A. Harper, Aszderson, Roberts, and Hayper :
830 The Oxides, (1949).

831 [20] Z. Hiezl, D.I. Hambley, C. Padovani, W.E. Lee, Processing and microstructural
832 characterisation of a UO2-based ceramic for disposal studies on spent AGR fuel,
833 J. Nucl. Mater. 456 (2015) 74–84. doi:10.1016/j.jnucmat.2014.09.002.

834 [21] V. Neck, J.I. Kim, Solubility and hydrolysis of tetravalent actinides, Radiochim.
835 Acta. 89 (2001) 1–16. doi:10.1524/ract.2001.89.1.001.

836 [22] D. Rai, A.R. Felmy, J.L. Ryan, Uranium(IV) Hydrolysis Constants and Solubility
837 Product of UO2·x*H2O(am), Inorg. Chem. 29 (1990) 260–264.
838 doi:10.1021/ic00327a022.

839 [23] K. Fujiwara, H. Yamana, T. Fujii, K. Kawamoto, T. Sasaki, H. Moriyama, Solubility
840 product of hexavalent uranium hydrous oxide, J. Nucl. Sci. Technol. 42 (2005)

841 289–294. doi:10.1080/18811248.2005.9726392.

842 [24] K. Opel, S. Weiß, S. Hübener, H. Zänker, G. Bernhard, Study of the solubility of
843 amorphous and crystalline uranium dioxide by combined spectroscopic methods,
844 Radiochim. Acta. 95 (2007) 143–149. doi:10.1524/ract.2007.95.3.143.

845 [25] A.J. Popel, B.T. Tan, T. Gouder, G.I. Lampronti, J. Day, R. Eloirdi, A. Seibert, I.
846 Farnan, Surface alteration evidence for a mechanism of anoxic dissolution of
847 UO2, Appl. Surf. Sci. 464 (2019) 376–379. doi:/10.1016/j.apsusc.2018.09.094.

848 [26] A. Fernández, D. Haas, R.J.M. Konings, J. Somers, Transmutation of actinides, J.
849 Am. Ceram. Soc. 85 (2002) 694–696.

850 [27] M. Cologna, V. Tyrpekl, M. Ernstberger, S. Stohr, J. Somers, Sub-micrometre
851 grained UO2 pellets consolidated from sol gel beads using spark plasma sintering
852 (SPS), Ceram. Int. 42 (2016) 6619–6623. doi:10.1016/J.CERAMINT.2015.12.172.

853 [28] J.M. Elorrieta, L.J. Bonales, M. Naji, D. Manara, V.G. Baonza, J. Cobos, Laser-
854 induced oxidation of UO_2: A Raman study, J. Raman Spectrosc. (2018) 878–
855 884. doi:10.1002/jrs.5347.

856 [29] F. Bachmann, R. Hielscher, H. Schaeben, Texture Analysis with MTEX – Free
857 and Open Source Software Toolbox, Solid State Phenom. 160 (2010) 63–68.
858 doi:10.4028/www.scientific.net/SSP.160.63.

859 [30] N. The MathWorks, MATLAB 2016a, (2016).

860 [31] G. Bruker Nano GmbH, Berlin, QUANTAX CrystAlign., (2010).

[32] K.I. Maslakov, Y.A. Teterin, A.J. Popel, A.Y. Teterin, K.E. Ivanov, S.N. Kalmykov, V.G. Petrov, R. Springell, T.B. Scott, I. Farnan, XPS study of the surface chemistry of UO2 (111) single crystal film, Appl. Surf. Sci. 433 (2018) 582–588. doi:10.1016/j.apsusc.2017.10.019.

[33] S. Sunder, D.W. Shoesmith, M.G. Bailey, F.W. Stanchell, N.S. McIntyre, Anodic oxidation of UO2. Part I. Electrochemical and X-ray photoelectron spectroscopic studies in neutral solutions, J. Electroanal. Chem. 130 (1981) 163–179. doi:10.1016/S0022-0728(81)80384-1.

[34] R.J. Wilbraham, C. Boxall, D.T. Goddard, R.J. Taylor, S.E. Woodbury, The effect of hydrogen peroxide on uranium oxide films on 316L stainless steel, J. Nucl. Mater. 464 (2015) 86–96. doi:10.1016/j.jnucmat.2015.04.007.

[35] E. Cera, M. Grivé, J. Bruno, K. Ollila, Modelling of the U0 2 dissolution mechanisms in synthetic groundwater solutions Dissolution experiments carried out under oxic conditions, 2001.

[36] J.M. Elorrieta, L.J. Bonales, N. Rodríguez-Villagra, V.G. Baonza, J. Cobos, A detailed Raman and X-ray study of UO2+x oxides and related structure transitions, Phys. Chem. Chem. Phys. 18 (2016) 28209–28216. doi:10.1039/C6CP03800J.

[37] H. He, D. Shoesmith, Raman spectroscopic studies of defect structures and phase transition in hyper-stoichiometric UO2+x, Phys. Chem. Chem. Phys. 12 (2010) 8108. doi:10.1039/b925495a.

882 [38] G.C. Allen, I.S. Butler, Nguyen Anh Tuan, Characterisation of uranium oxides by
883 micro-Raman spectroscopy, J. Nucl. Mater. 144 (1987) 17–19. doi:10.1016/0022-
884 3115(87)90274-1.

885 [39] M. Razdan, D.W. Shoesmith, Influence of Trivalent-Dopants on the Structural and
886 Electrochemical Properties of Uranium Dioxide (UO2), J. Electrochem. Soc. 161
887 (2013) H105–H113. doi:10.1149/2.047403jes.

888 [40] G. Guimbretière, L. Desgranges, A. Canizarès, R. Caraballo, F. Duval, N.
889 Raimboux, R. Omnée, M.R. Ammar, C. Jégou, P. Simon, In situ Raman
890 monitoring of He2+ irradiation induced damage in a UO2 ceramic, Appl. Phys.
891 Lett. 103 (2013). doi:10.1063/1.4816285.

892 [41] O.A. Maslova, G. Guimbretière, M.R. Ammar, L. Desgranges, C. Jégou, A.
893 Canizarès, P. Simon, Raman imaging and principal component analysis-based
894 data processing on uranium oxide ceramics, Mater. Charact. 129 (2017) 260–269.
895 doi:10.1016/j.matchar.2017.05.015.

896 [42] L. Desgranges, G. Baldinozzi, P. Simon, G. Guimbretière, A. Canizares, Raman
897 spectrum of U 4O 9: A new interpretation of damage lines in UO 2, J. Raman
898 Spectrosc. 43 (2012) 455–458. doi:10.1002/jrs.3054.

899 [43] G. Leinders, T. Cardinaels, K. Binnemans, M. Verwerft, Accurate lattice
900 parameter measurements of stoichiometric uranium dioxide, J. Nucl. Mater. 459
901 (2015) 135–142. doi:10.1016/j.jnucmat.2015.01.029.

902 [44] Y. Okada, Y. Tokumaru, Precise determination of lattice parameter and thermal

903 expansion coefficient of silicon between 300 and 1500 K, J. Appl. Phys. 56 (1984)
904 314–320. doi:10.1063/1.333965.

905 [45] C.L. Corkhill, D.J. Bailey, F.Y. Tocino, M.C. Stennett, J.A. Miller, J.L. Provis, K.P.
906 Travis, N.C. Hyatt, Role of Microstructure and Surface Defects on the Dissolution
907 Kinetics of CeO2, a UO2 Fuel Analogue, ACS Appl. Mater. Interfaces. 8 (2016)
908 10562–10571. doi:10.1021/acsami.5b11323.

909 [46] C.L. Corkhill, E. Myllykylä, D.J. Bailey, S.M. Thornber, J. Qi, P. Maldonado, M.C.
910 Stennett, A. Hamilton, N.C. Hyatt, Contribution of energetically reactive surface
911 features to the dissolution of CeO2 and ThO2 analogues for spent nuclear fuel
912 microstructures, ACS Appl. Mater. Interfaces. 6 (2014) 12279–12289.
913 doi:10.1021/am5018978.

914 [47] W. Stumm, Reactivity at the mineral-water interface: Dissolution and inhibition,
915 Colloids Surfaces A Physicochem. Eng. Asp. 120 (1997) 143–166.
916 doi:10.1016/S0927-7757(96)03866-6.

917 [48] U. Schwertmann, T.U. Miinchen, Solubility and dissolution of iron oxides, (1991)
918 1–25.

919 [49] M.D. Kaminski, N.M. Dimitrijevic, C.J. Mertz, M.M. Goldberg, Colloids from the
920 aqueous corrosion of uranium nuclear fuel, J. Nucl. Mater. 347 (2005) 77–87.
921 doi:10.1016/j.jnucmat.2005.07.009.

922 [50] H. Zänker, C. Hennig, Colloid-borne forms of tetravalent actinides: A brief review,
923 J. Contam. Hydrol. 157 (2014) 87–105. doi:10.1016/j.jconhyd.2013.11.004.

924 [51] P.C. Hiemenz, R. Rajagopalan, Surface Tension and Contact Angle: Application
925 to Pure Substances, 1997. doi:10.1201/9781315274287.

926 [52] I. Dreissig, S. Weiss, C. Hennig, G. Bernhard, H. Zänker, Formation of
927 uranium(IV)-silica colloids at near-neutral pH, Geochim. Cosmochim. Acta. 75
928 (2011) 352–367. doi:10.1016/j.gca.2010.10.011.

929 [53] S. Szenknect, A. Mesbah, T. Cordara, N. Clavier, H.P. Brau, X. Le Goff, C.
930 Poinssot, R.C. Ewing, N. Dacheux, First experimental determination of the
931 solubility constant of coffinite, Geochim. Cosmochim. Acta. 181 (2016) 36–53.
932 doi:10.1016/j.gca.2016.02.010.

933 [54] T.Y. Zhang, M.H. Zhao, Equilibrium depth and spacing of cracks in a tensile
934 residual stressed thin film deposited on a brittle substrate, Eng. Fract. Mech. 69
935 (2002) 589–596. doi:10.1016/S0013-7944(01)00098-4.

936 [55] L. Desgranges, H. Palancher, M. Gamaléri, J.S. Micha, V. Optasanu, L. Raceanu,
937 T. Montesin, N. Creton, Influence of the U_3O_7 domain structure on cracking during
938 the oxidation of UO_2, J. Nucl. Mater. 402 (2010) 167–172.
939 doi:10.1016/j.jnucmat.2010.05.014.

940 [56] C. McMahon, B. Soe, A. Loeb, A. Vemulkar, M. Ferry, L. Bassman, Boundary
941 identification in EBSD data with a generalization of fast multiscale clustering,
942 Ultramicroscopy. 133 (2013) 16–25. doi:10.1016/j.ultramic.2013.04.009.

943 [57] E.J.. Whittaker, Cleavage energies of minerals, Mineral. Mag. 46 (1982) 398–9.

[58] D.L. Parkhurst, C.A.. Appelo, Description of input and examples for PHREEQC version 3-- A computer program for speciation, batch- reaction, one- dimensional transport, and inverse geochemical calculations, 2013.

[59] J.E. Cross, F.T. Ewart, Hatches — A Thermodynamic Database And Management System, Radiochim. Acta. 52–53 (1991) 421–422. doi:10.1524/ract.1991.5253.2.421.

[60] I. Grenthe, J. Fuger, R.J. Lemire, A.B. Muller, H. Wanner, I. Forest, Chemical Thermodynamics of Uranium, 1992. (1992) 715. doi:10.1063/1.473182.

[61] P. Carbol, P. Fors, S. Van Winckel, K. Spahiu, Corrosion of irradiated MOX fuel in presence of dissolved H2, J. Nucl. Mater. 392 (2009) 45–54. doi:10.1016/j.jnucmat.2009.03.044.

[62] S.Y. Yang, H.D. Yeh, Modeling transient heat transfer in nuclear waste repositories, J. Hazard. Mater. 169 (2009) 108–112. doi:10.1016/j.jhazmat.2009.03.068.

[63] O.N. Batuk, Behaviour of Uranium Dioxide under Oxidative Hydrothermal Conditions, PhD Thesis, Lomonosov Moscow Sate Univ. (2007).

Highlights

- Extended dissolution of different forms of UO_2 was conducted under strict anoxic conditions.
- Dissolved uranium of the same magnitude (10^{-9} mol/l) was obtained for all physical forms of UO_2.
- Different secondary phases of uranium were observed from dissolution in di-water.
- These U(IV) secondary phases limit dissolved concentrations of uranium.

Surface and electrochemical controls on UO_2 dissolution under anoxic conditions

Beng Thye Tan [a,*], Aleksej J. Popel [a], Richard J. Wilbraham [b], Jason Day [a], Giulio I. Lampronti [a], Colin Boxall [b], Ian Farnan [a]

[a] Department of Earth Sciences, University of Cambridge, Downing Street, Cambridge, CB2 3EQ, United Kingdom

[b] The Lloyd's Register Foundation Centre for Nuclear Engineering, Engineering Department, Lancaster University, Bailrigg, Lancashire, LA1 4YW, United Kingdom

[*] Corresponding author. Present address: Department of Earth Sciences, University of Cambridge, Downing Street, Cambridge, CB2 3EQ, United Kingdom, tel: +44 1223 768357, e-mail: btt30@cam.ac.uk

Abstract

The escape of radionuclides from underground spent nuclear fuel disposal facilities will likely result from anoxic dissolution of spent nuclear fuel by intruding groundwater. Anoxic dissolution of various forms of uranium dioxide (UO_2), namely bulk pellet, powder and thin film, has been investigated. Long-duration static batch dissolution experiments were designed to investigate the release of uranium ions in deionized water and any surface chemistry that may occur on the UO_2 surface. The dissolved uranium concentration for anoxic dissolution of nearly stoichiometric UO_2 was found to be of the order of 10^{-9} mol/l for the three different sample types. Further, clusters (~500 nm) of homogenous uranium-containing precipitates of ~20–100 nm grains were observed in thin film dissolution experiments. Such a low solubility of UO_2 across sample types and the observation of secondary phases in deionized water suggest that anoxic UO_2 dissolution does not only occur through a $U(IV)_{(solid)}$ to $U(VI)_{(aqueous)}$ process. Thus, we propose that dissolution of uranium under anoxic repository conditions may also proceed via $U(IV)_{(solid)}$ to $U(IV)_{(aqueous)}$, with subsequent $U(IV)_{(precipitates)}$ in a less defective form. Quantitative analysis of surface-sensitive EBSD diffractograms was conducted to elucidate lattice-mismatch induced cracks observed in UO_2 thin film studies. Variable temperature anoxic dissolution was conducted, and no increased uranium concentration was observed in elevated temperatures.

Keywords: UO_2; anoxic dissolution; secondary phases; surface alteration; nucleation; geological disposal

1. Introduction

The relative abundance of uranium as an energy resource, coupled with the high costs of spent nuclear fuel (SNF) reprocessing and the associated risks of nuclear proliferation, make a strong case for direct disposal of SNF in deep underground geological disposal facilities (GDF) [1,2]. The evaluation of such a facility is a multi-faceted problem; of which an important consideration is the projected radionuclide release rates from the spent fuel in the case of groundwater intrusion and secondary containment failure [3,4]. Extensive work had been devoted to the analysis of the different aspects of spent nuclear fuel dissolution under geological disposal conditions [2–11]. Depending on burn-up and local position in the rod (the linear power rating), spent fuel is comprised of ~96 at% uranium dioxide (UO_2) matrix with ~3 at% of fission products and ~1 at% of transuranium elements. As such, previous studies have shown that the release of radionuclides (apart from instant release fractions [12,13] of several percent of total inventory for some radionuclides), is mainly dependent on dissolution of the UO_2 matrix under the oxygen-free environment of deep geological facilities [3,4].

However, there has been no consensus on the proposed mechanisms of anoxic UO_2 dissolution in the literature. Ulrich et al. [14] initially suggested that anoxic dissolution of UO_2 proceeds via Eq. 1:

$$UO_2(s) + 4H^+ \rightleftharpoons U^{4+} + 2H_2O \quad (1).$$

Based on an XPS analysis of leached UO_2 samples consisting of bulk and surface U(IV), they noted surface oxidation to 7–10% U(VI) and ~20% U(V) under reducing dissolution conditions (5 vol% H_2, 95 vol% N_2 atmosphere) which was explained by a sequential oxidation mechanism of U(IV) to U(V) to U(VI) by water molecules, similar to

that proposed by Shoesmith and Sunder [15] for UO_2 dissolution below the oxidative threshold potential (–100 mV versus saturated calomel electrode on the UO_2 surface).

$$UO_2 + H_2O \rightarrow \left(U^{V}O_2OH\right)_{ads} + H^+ + e^-_{(aq)} \quad (2),$$

$$\left(U^{V}O_2OH\right)_{ads} + H_2O \rightarrow \left(U^{VI}O_2(OH)_2\right)_{ads} + H^+ + e^-_{(aq)} \quad (3).$$

A caveat to the applicability of these equations is the absence of detectable U(VI) in the sample solutions with a kinetic phosphorescence analyzer (KPA), although U(VI) is a few orders of magnitude more soluble than U(IV) [16]. Ulrich et al. concluded that the anoxic UO_2 dissolution was primarily driven by hydrolysis of U(IV) and not by oxidation to U(VI) [14]. However, it is possible that, although the sample transfer occurred with minimal exposure to oxygen in this work, a short exposure was enough to induce surface oxidation, which led to the observed U(V) and U(VI) at the surface. In addition, Ollila et al. [5] reported that after anoxic (N_2 atmosphere) dissolution of UO_2 in deionized water, the uranium oxidation state in the solution was U^{6+} as determined by anion exchange methods in an HCl medium within an inert atmosphere glove box (N_2). However, there was no information on the characterization of UO_2 samples in contact with the solution. In view of the above literature, the motivation of this paper is to investigate the anoxic dissolution mechanism of uranium dioxide with respect to the anoxic conditions pertaining in a GDF.

Considering the long timeline for SNF storage and disposal, this study focuses on the long-term surface changes and products due to dissolution of spent nuclear fuel. Three anoxic experiments with near stoichiometric uranium dioxide were conducted with

different aims. 1) The dissolution of uranium dioxide in solid pellet electrode form to determine electrochemical variation of both solution and surface and subsequent analysis of surface oxidation with Raman spectroscopy, Scanning Electron Microscopy (SEM) and Energy Dispersive X-ray (EDX) analysis techniques. 2) The dissolution of a single crystal uranium dioxide thin film (~100 nm thickness) deposited epitaxially on a (001) silicon substrate, to ascertain uranium dissolution and potential secondary phase precipitation [9,10] on a topographically flat surface with high surface sensitivity. 3) High-surface area UO_2 powder in steel heating vessels with PTFE (polytetrafluoroethylene) liners to analyse differences in dissolved uranium concentrations at different temperatures, simulating decay heat at different disposal ages.

2. Materials and methods

2.1. Anoxic conditions

Anoxic dissolution involves the exclusion of dissolved oxygen in the experiments as far as reasonably possible. All dissolution experiments were conducted in positive pressure gloveboxes with an argon atmosphere with oxygen concentrations controlled to 0.1 ppm O_2 for the thin film and powder experiments and a nitrogen atmosphere of 2.0 ppm O_2 for the solid pellet experiments. In all cases, the dissolution experiments took place in sealed containers containing deoxygenated water. Deionized Milli-Q water (18.2 MΩ/cm), for both dissolution and sample washing, was sparged with 5 vol% H_2 in 95 vol% Ar gas mixture for 6 hours to reduce the amount of dissolved oxygen to a

103 suitable low level. Post-sparging testing with CHEMetrics® Oxygen CHEMets Kit K-
104 7540 revealed dissolved oxygen content below the detection limit of 2.5 ppb.

105 *2.2. Sample preparation*

106 Efforts have been taken to reduce the amount of U(VI) and U(V) from surface
107 oxidation of the nominal UO_2 samples. Powder and thin film samples were reduced in a
108 5 vol% H_2, 95 vol% Ar atmosphere and heating to 800º C [17]. Sintered UO_2 pellets
109 were polished with SiC paper under deionized water to remove any oxidized surface
110 layer of UO_{2+x} that arises from exposure to the atmosphere for extended periods of time
111 [18]. Anderson et al. [19] have previously reported that such surface oxidation occurs
112 slowly as a logarithmic function of time due to the chemisorption of oxygen at room
113 temperatures. Pellet and thin film samples were subsequently pre-washed before
114 undertaking dissolution experiments.

115 A detailed description of the fabrication and initial characterisation of sintered UO_2
116 pellets has been previously reported by Hiezl et al. [20] with additional characterisation
117 by Popel et al. [10]. In order to make suitable electrodes for use in long-term dissolution
118 experiments, stoichiometric UO_2, disc-shaped slices of sintered pellets (~1 cm diameter
119 and ~1 mm thickness) were mounted onto a threaded brass rod using silver-loaded
120 epoxy. This assembly was then placed in a cylindrically shaped mould and cast in
121 epoxy resin in order to produce a suitable sealed working electrode. Prior to being
122 characterised, the working electrodes were polished using 600 and 1200 grit SiC paper
123 under deionized water (to avoid uranium dust formation). Such a polishing process
124 reduces differences in electrode surface area between samples and enhances the

reproducibility of triplicate dissolution experiments (see Section 2.5.1). Prior to dissolution, the polished surfaces were examined by scanning electron microscopy and Raman spectroscopy (see Section 2.3) before placing them in 10 ml of deoxygenated, deionized water in a Nalgene® bottle for 21-hours pre-washing under a N_2 atmosphere with 2.0 ppm O_2. This pre-wash phase again aims to remove any higher oxidation uranium oxide phases which might have been formed, albeit slowly, in the processing atmosphere and relies on the higher solubility of surface UO_{2+x} phases vs. bulk UO_2. Indeed, previous literature studies [21–23] have found that the solubility product at the standard state, Ksp° of U(VI) is -22.46, significantly higher than that of U(IV), -52.0 with slight variation dependent on solid form [24].

The thin film of UO_2 was produced by direct current reactive sputtering onto a single crystal Si substrate with (001) orientation using a Labstation machine at the European Commission Joint Research Centre (EC-JRC), Karlsruhe. The substrate was cleaned before the film deposition with ethanol and heated to ~600 °C under pO_2 of 2×10^{-6} mbar for 40–60 min [25]. A natural uranium metal target was used as a source of uranium with argon used as the sputtering gas at a pAr set to 5×10^{-3} mbar and O_2 used as the reactive gas at a pO_2 set to 7×10^{-6} mbar. The Si substrate was maintained at a temperature close to 600 °C. The film was deposited for 30 minutes with deposition conditions which should give film thickness in the range from 90 to 270 nm. The thin film sample was then annealed in an anoxic glove box-attached furnace at 800 °C with a reducing mixture of 5 vol% H_2 in 95 vol% Ar for two hours, taking one hour to heat up and three hours to cool down. It was subsequently transferred to another glove box, where the dissolution experiment took place under an argon atmosphere at 0.1 ppm O_2.

148 Finally, pre-wash in 20 ml of sparged deionized water in a plastic bottle for 12 hours
149 was carried out before transfer to a fresh deionized water solution for the dissolution
150 experimental run (see section 2.5.2).

151 For the powder samples, high surface area, micro-porous UO_2 beads were produced
152 from uranyl nitrate at the EC-JRC by the sol-gel technique [26,27]. About 2.3 g of this
153 powder was weighed and transferred into a 1 ml alumina boat for annealing. In order to
154 achieve stoichiometry, the powder was annealed in a tube furnace attached to a glove
155 box where ingress and egress of the sample into the furnace occurs inside the glovebox
156 with an argon atmosphere (0.1 O_2 ppm). It was annealed at 800 $^{\circ}$C for three hours with
157 a reducing gas mixture of 5 vol% H_2 in 95 vol% Ar, after an initial hour of pre-heating to
158 the requisite temperature. There was no pre-wash carried out for this set of
159 experiments.

160 *2.3. Sample characterisation*

161 The solid pellet samples were analysed before and after the dissolution experiment
162 by SEM with EDX as well as a Raman microscopy system. SEM-EDX was carried out at
163 20 keV using a JSM-6010PLUS (Jeol, Japan). Raman microscopy measurements were
164 taken using a Voyage confocal Raman microscope system (B&WTek, Newark, USA).
165 All Raman spectra were acquired with an excitation wavelength of 785 nm. The sample
166 was focussed using a 50× objective lens before taking spectra with an integration time
167 of 40 seconds over a wavenumber range from 190 to 3000 cm^{-1}. Before analysis, the
168 laser power was adjusted to < 5 mW using neutral density filters in order to avoid any
169 thermal oxidation of UO_2 to U_3O_8 [28]. In order to account for surface roughness and

surface inhomogeneity, 10 spectra were taken at random locations across the sample with the highest and lowest outliers removed to produce a sample average.

The thin film sample was analysed before and after the dissolution experiment by SEM, EDX, X-ray diffraction (XRD) and electron backscatter diffraction (EBSD) techniques [25]. A FEI Quanta 650F instrument operating at 5 kV with beam spot size 3 under high vacuum was used to acquire SEM images with a Bruker 6130 XFlash EDX detector. EBSD instrumentation from Bruker with an e-Flash$_{HD}$ detector associated with the FEI Quanta 650F SEM was used to obtain EBSD data; the resolution of each square pixel of 97 nm. The operating voltage was 20 kV and the beam spot size 5.5. The detector resolution was 320 × 240 pixels, while working distance and sample to detector distance was 26 mm and 15.5 mm respectively. Analysis of collected EBSD data from the uranium dioxide thin film was conducted with the computational aid of MTEX V5.0.3 [29], a freeware toolset for the commercial software package MATLAB™ [30]. The MATLAB™ toolbox MTEX provides a unique way to represent, analyse and interpret crystallographic preferred orientation, i.e. texture, based on integral ("pole figure") or individual orientation ("EBSD") measurements.

Due to limitations in examining radioactive uranium oxide powder under vacuum, capillary XRD was conducted with a Bruker D8 Advance diffractometer (Cu Kα radiation, λ = 1.541 Å, Ge monochromator and Sol-XE energy dispersive detector). Measurements were carried out for 12 hours each over an angular range $25° \leq 2\theta \leq 90°$ ($\Delta 2\theta$ = 0.01°). Data collection and indexing was performed with Bruker QUANTAX CrystaAlign software [31]. A full Rietveld refinement was carried out of the acquired diffraction patterns. The backgrounds were fitted using linear interpolation and the peak

193 shape was modelled using a pseudo-Voigt function for the micro-porous uranium
194 dioxide powder pre- and post-annealing. Based on
195 5.466 Å, and the equation $a_x = 5.4690 - 0.12x$ [32], a bulk stoichiometric ratio prior to
196 dissolution of $UO_{2.03}$ was found for the UO_2 powder. However, in this dissolution study,
197 the bulk stoichiometric ratio may be lower than the surface. As discussed by Sunder
198 [33], the surface is likely to be UO_{2+x} ($0 < x < 0.25$). This is because XRD is a bulk
199 technique which convolutes the signal from the underlying bulk and surface signals
200 hence typically registering lower values of *x* than surface sensitive Raman spectroscopy
201 as Raman laser has a lower penetration depth than X-rays.

202 *2.4. Aliquot analyses*

203 For inductively coupled plasma mass spectrometry (ICP-MS), the acquired 1 ml
204 aliquots (see section 2.5) were acidified with another 1 ml of 1 wt% HNO_3. All samples
205 were analysed on a Perkin Elmer Nexion 350D ICP-MS instrument. The uranium
206 calibration standards were prepared as an external calibration using serial dilutions of
207 standards (blank, 0.001, 0.01, 0.10, 1.0, 10 ppb, mass basis) prepared from single
208 element high purity standard (CPI, California, USA) in high purity 1 wt % HNO_3 (quartz
209 distilled in house). The ICP-MS internal standards were 10 ppb Rh, In and Re and each
210 sample was prepared in 1 wt % HNO_3, added online with a t-piece and mixing tube prior
211 to the nebuliser. Two different independently prepared quality control standards (SPS-
212 SW2, LGC Standards, UK and SCP Science, Canada, ICP-MS Verification Mix) were
213 repeatedly analysed throughout the run to check for calibration accuracy (~5%) with a
214 similar precision. Instrumental drift was less than 10% measured for the raw intensity of
215 the internal standards during the entire analytical run (50 or more solutions per batch).

Solutions were analysed using a Micromist FM05 microconcentric nebuliser using a pumped flow rate of 80 µl/min (Glass Expansion, Australia) and a quartz cyclonic baffled spray chamber with nickel sampler and skimmer cones. ICP-MS sensitivity in this configuration was 4.5×10^5 cps/ppb In with CeO/Ce ratios = 2.8%. Concentration results were calculated using the Syngistix 1.1 software with a simple linear calibration line and intercept set to zero. The raw intensities were blank subtracted and internal standard normalised before calibration calculations were performed. All results (unknowns and standards) were accurately corrected for dilutions by mass by performing all dilutions with calibrated pipettes on a four place analytical balance.

For the leachate from the uranium dioxide thin film experiment, dynamic light scattering was used to confirm the absence of colloids greater than 5 nm. Inductively coupled plasma atomic emission spectroscopy (ICP-AES) of this leachate found the concentration of dissolved silicon in that experiment to be in the range of 15–25 ppb.

2.5. Dissolution experiment setups

A summary of the dissolution experiments has been tabulated at the end of this section in Table 1.

2.5.1 Solid pellet dissolution

After a 21-hour prewash and drying for 1 hour in the glovebox atmosphere, UO_2 electrodes were immersed in 220 ml of sparged, deionized water in a sealed (screw top) 480 ml Fisherbrand® PTFE dissolution vessel. Dissolution measurements were performed in triplicates.

To determine the electrochemical evolution of both the uranium dioxide electrode and the solution potential, open circuit potentiometry was used [34]. Solution potential was measured using 500 μm Au disk electrodes, polished using 600 and 1200 grit SiC papers and rinsed with deoxygenated, deionized water inside the glovebox prior to immersion. Through the use of a simple switch box, the open circuit potential of both electrodes was measured vs. one reference electrode. In order to avoid chloride contamination, an ammonium nitrate saturated agar double junction was used with an Ag|AgCl reference electrode (RE-5B, BASi, Indiana, USA). All vessels were tightly closed to prevent water evaporation, with gaps around electrodes sealed using parafilm®. One vessel filled with 250 ml of deionized water and an Au electrode only (no UO_2 electrode) was used as a control. During dissolution, batch replenishment tests were conducted, where ~1 ml aliquots of the solution sample were extracted and ~1 ml of the deionized water was replenished at defined time intervals after the start of the experiment, namely 2 hours, 6 hours, 1 day, 5 days, 12 days, 30 days, 61 days and 100 days. The amount of solution in the aliquots was monitored by weighing empty and filled vials on a balance. The dissolution of all samples was performed at an ambient temperature of ~25 °C for 100 days. After completion, the PTFE vessels were acid-washed using 3 M HNO_3. 5 ml of each acid wash was used for ICP-MS analysis in order to determine the presence of any uranium sorption or precipitation on the walls of the leaching vessel.

2.5.2 Thin film dissolution

After the 12-hour prewash and drying for an hour, the UO_2 thin film sample was rinsed with sparged, deionized water and placed into a 60 mL Fisherbrand® PTFE

dissolution vessel containing 20 ml of the deionized water and two blank Si substrates (to detect any U precipitation/nucleation from the solution) [25].

Static batch replenishment tests were run where ~1 ml aliquots were extracted at various intervals and ~1 ml of the deionized water was replenished. One vessel, filled with 20 ml of the deionized water and two blank Si substrates, was used as a control blank. All vessels were tightly closed to prevent water evaporation. The amount of the solution transferred from the dissolution vessels into the vials was monitored by weighting empty and filled vials. The dissolution experiment was performed at an ambient temperature of ~25 °C for 140 days.

2.5.3 High surface area powder dissolution

After annealing, 100 mg of reduced UO_2 powder was weighed out carefully with a Mettler Toledo XS-104 mass balance and placed into each of twelve stainless steel leaching vessels with a PTFE liner and a Swagelock seal. Upon the addition of 4 ml of sparged, deionized water to each leaching vessel, the leaching vessel was tightly sealed and transferred to another glove box under double containment. The dissolution experiment was performed at 4 different temperatures ambient (~25 ˚C), 40 ˚C, 90 ˚C and 140 ˚C with deoxygenated water (<2.5 ppb O_2) within an Ar atmosphere glovebox (0.1 O_2 ppm). All vessels were kept in the glove box for the duration of the experiment and tightly sealed. The extraction was carried out on the 390th day with a syringe through a 0.45 µm pore size disposable filter.

Table 1

A summary of the UO_2 dissolution experiments conducted in this study

	Annealing	Polishing	Prewashing	Oxygen content	Leaching test conditions
Pellet	No	Yes (SiC paper + deionized water)	Yes (21 hours) – 10 mL	2 ppm glovebox <2.5 ppb dissolved O_2	100 days 220 mL deionized water
Thin film	Yes (5% H_2 in Ar at 800 ^{0}C for 2 hours)	No.	Yes (12 hours) – 20 mL	0.1 ppm <2.5 ppb dissolved O_2	140 days 20 mL deionized water
Powder	Yes (5% H_2 in Ar at 800 ^{0}C for 2 hours)	Not applicable	No	0.1 ppm <2.5 ppb dissolved O_2	390 days 4 mL deionized water Filtration 0.45 µm

3. Results

3.1. Solid pellet dissolution

ICP-MS results, represented in Fig. 1, show a uranium concentration increase from 1×10^{-9} mol/l to ~6×10^{-9} mol/l being leached from the solid uranium pellet. Such a low level of uranium release is indicative of anoxic dissolution, which has a reduced rate of uranium ion release compared to oxic leaching [35]. This also agrees with the end solution potential of the uranium containing pots (-56 mV, -52 mV, -52 mV vs. SCE, respectively) and the control pot (-55 mV vs SCE). There is no significantly measurable difference in the solution potential between the leaching and control pots. Such a negligible change in potential is predicted by the Nernst equation, as the dissolved uranium ion release into the solution is so small (10^{-9} mol/l).

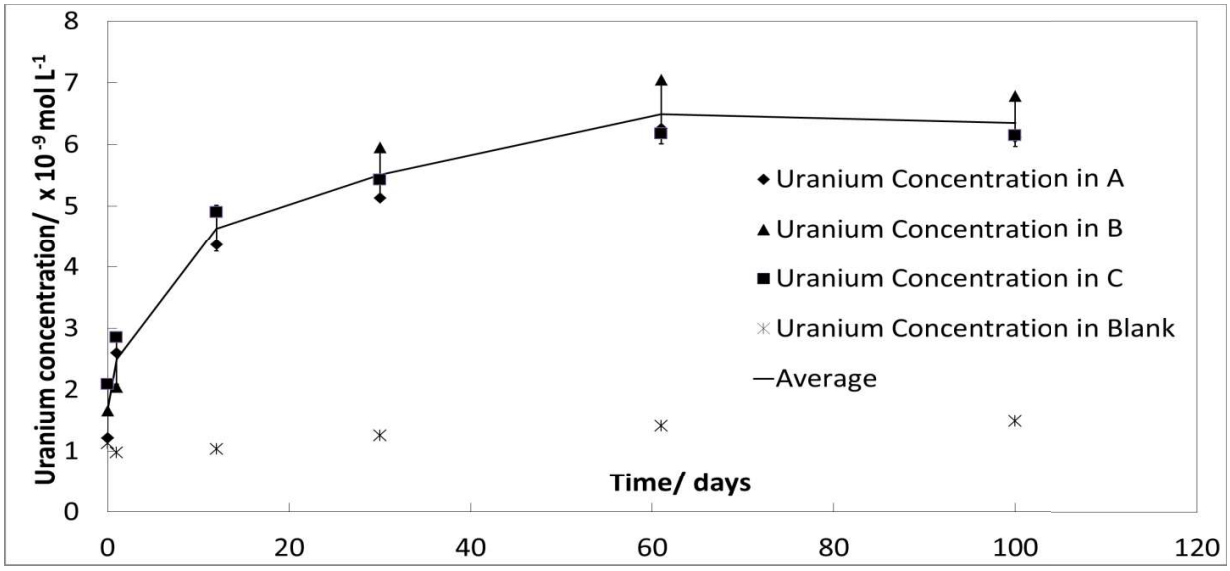

294

295 **Fig. 1.** Uranium concentration in aliquots obtained from three vessels, A, B and C
296 containing a uranium pellet each and a control vessel labelled as blank with the same
297 set up without a uranium pellet.

298 The concentration of uranium reaches a maximum value of 6 × 10^{-9} mol/l after 60
299 days. This may be attributed to the uranium reaching its solubility limit under anoxic
300 condition, hence there was a decrease in the driving force for further dissolution. Under
301 such a scenario, reprecipitation can occur, which was confirmed by the detection of
302 solid uranium precipitates when dissolved uranium was observed in the acid washout
303 fraction after the experiment. This effect is more pronounced in the uranium
304 concentration data of the thin film experiment discussed in Fig. 6 under Section 3.2.
305 ICP-MS of acid washes of the vessels after completion of the dissolution experiment
306 show a dissolved uranium concentration of ~3 × 10^{-9} mol/l in 250 cm^3 of 3 mol/l nitric
307 acid, which is significantly higher than that in the blank pot (1 x 10^{-9} mol/l). Such an
308 observation supports the presence of precipitated uranium phases within the dissolution

vessel.

Fig. 2 shows the recorded open circuit potential of the uranium dioxide electrodes at the beginning and end of this experiment. These measurements indicate some evolution [15] of the oxidation state at the uranium dioxide surface. Referencing with a standard calomel electrode, Shoesmith and Sunder [15] reported potential readings between -150 to -270 mV for near stoichiometric uranium dioxide in argon-purged solutions, containing UO_{2+x}. This correlates reasonably well with our data with an average initial reading of -150 mV shown in Fig. 2. With increased oxidation of the uranium surface, Shoesmith and Sunder reported that the potential reading would increase correspondingly, and the region of oxidative dissolution occurs at a threshold of -50 to -100 mV, where the surface composition approaches a thin layer (2–5 nm) of $UO_{2.33}$ as detected from angular-dependent XPS studies [33]. Our experimental reading reaches an average of -70 mV after 100 days of dissolution. We suspect that this might be due to oxidation arising from trace amount of ~2 ppm O_2 present in the glovebox atmosphere.

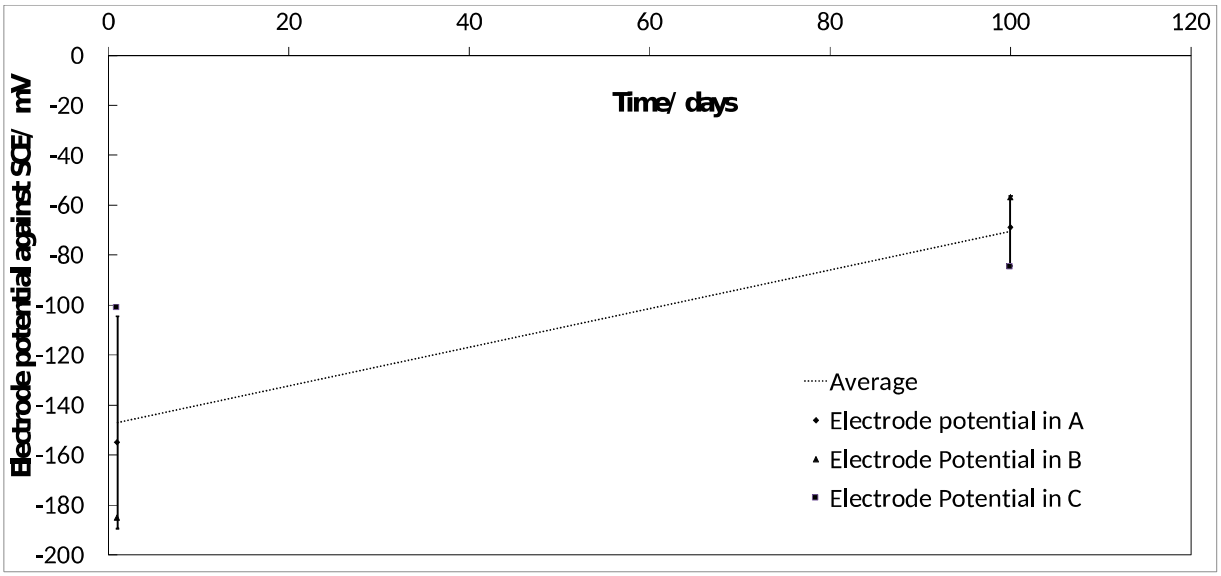

Fig. 2. Open circuit potential of the uranium dioxide electrodes recorded at the beginning and end of this leaching experiment. Note values are plotted vs. the standard calomel electrode (SCE) for ease of comparison with data from [15].

Area averaged Raman spectra of a freshly polished UO_2 electrode and three UO_2 electrodes after 100 days dissolution is shown in Fig. 3, which is a magnification of the Raman shift range 350 to 750 cm^{-1}, a region previously reported as being the most important with regards to the degree of oxidation of the UO_2 lattice [36,37]. It can be seen that there are two distinct differences between a freshly polished electrode and that leached in deionized water under anoxic conditions. Firstly, there is a decrease in the large vibration at 440 cm^{-1}, although it should be noted that this intensity difference is only significant for Electrode C after accounting for the measurement's standard deviation as function of measured area. Secondly, there is a small increase in the broad band from ~550 to ~650 cm^{-1}.

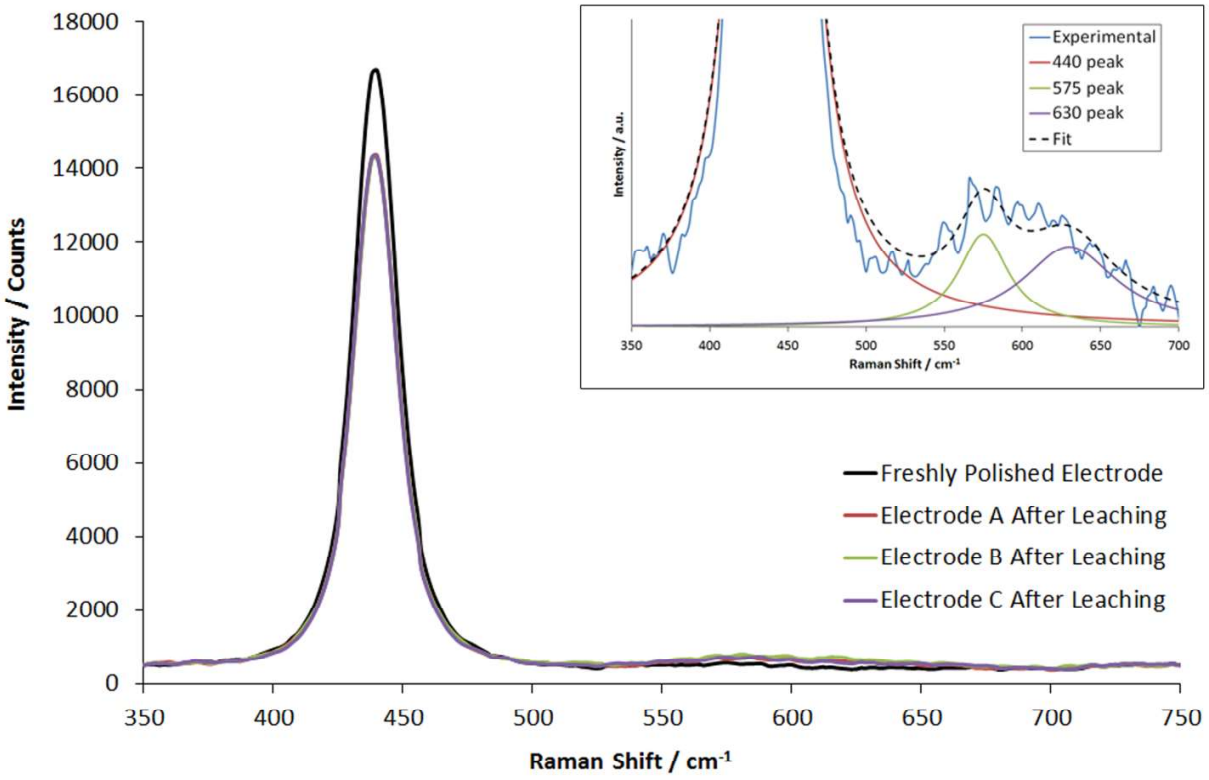

Fig. 3. Main: Linear baseline subtracted, area averaged Raman spectra of a freshly polished UO_2 electrode and three UO_2 electrodes after 100 days dissolution over the Raman shift range 350 to 750 cm^{-1}. Inset: Example Lorentzian fit of defect bands at 575 cm^{-1} and 630 cm^{-1} from a single measurement point from electrode A after leaching.

Considering the former 440 cm^{-1} vibration first, group theory predicts that a perfect fluorite structure would be expected to give a triply degenerate Raman active mode (T2g) [38], typically defined as the fundamental U-O symmetric stretching mode [11,39]. This intense vibration has been reported at ~445 cm^{-1} and in the UO_2 pellet samples of Fig. 3 is very close to this value at 440 cm^{-1}. A decrease in the intensity of this peak has been reported as being indicative of deviation from a perfect fluorite lattice structure, caused by either dopant effects or changes in UO_2 stoichiometry [37,39].

350 Turning now to the broad band from ~550 to ~650 cm^{-1}, this band has been ascribed
351 to various vibrations that may occur as a result of increasing lattice defectiveness [37].
352 In the absence of dopants, this region is composed of three overlapping peaks at 550,
353 575 and 630 cm^{-1}, respectively. The peak at 550 cm^{-1} has only recently been
354 considered and is tentatively assigned to UO_2 grain boundaries [36,40,41]. The other
355 two peaks are of more interest with regards to the degree of oxidation of the leached
356 samples. The first at 575 cm^{-1} has been assigned to a longitudinal optical (LO) phonon
357 [37]. Usually, this phonon is forbidden under the selection rule imposed due to lattice
358 symmetry, this peak can appear as a result of changes in translational symmetry at
359 oxygen vacancy sites, leading to lattice disorder and the consequential breakdown in
360 selection rules. These changes in symmetry are caused by either the incorporation of
361 interstitial oxygens or dopant ions. The second peak at 630 cm^{-1} has been attributed to
362 clustering of interstitial oxygens to form higher oxidation state cuboctahedrons
363 associated with a transition to a defective U_4O_9 structure [42].

364 Thus, the ratio of either the 575 cm^{-1} or 624 cm^{-1} peak to the 440 cm^{-1} UO
365 fundamental stretch is indicative of the degree of surface hyperstoichiometry (oxidation)
366 of UO_2 [36]. In order to determine the contributions of each peak to the broad band of
367 Fig. 3, a Lorentzian peak fit was performed for the data of Fig. 3, assuming peak
368 maxima at 440, 575 and 630 cm^{-1}. An example fit for data from electrode A is shown in
369 Fig. 3 – inset. The analysis of this peak expressed as a ratio to the 440 cm^{-1} peak are
370 shown in Fig. 4A for the 575 cm^{-1} and Fig. 4B for the 630 cm^{-1} peak.

371 For both the 575 cm^{-1} and 630 cm^{-1} peak, there is a significant increase in surface
372 oxidation heterogeneity as shown by the increase in result standard deviation after

electrode leaching in deionized water. However, with the exception of the 575 cm^{-1} peak for Electrode B, the results show a significant increase in the 575/440 and 630/440 peak ratio after dissolution compared to a freshly polished electrode. This suggests there is an increase in the degree of surface oxidation of the electrodes after leaching for 100 days, corroborating the change in the measured open circuit potentials of the uranium dioxide electrodes discussed above. Finally, despite the observed increase in surface oxidation, no new peaks were observed in the region 800–830 cm^{-1} [28] in any of the acquired spectra, suggesting that there was no detectable highly-oxidised uranium dioxide (such as U_3O_8 and above) phases formed during the leaching process.

Scanning electron microscopy and EDX studies of the UO_2 electrode surfaces were carried out pre- (Fig. 5a) and post-dissolution (Fig. 5b) to ascertain the presence of any observable surface morphology changes or secondary phases.

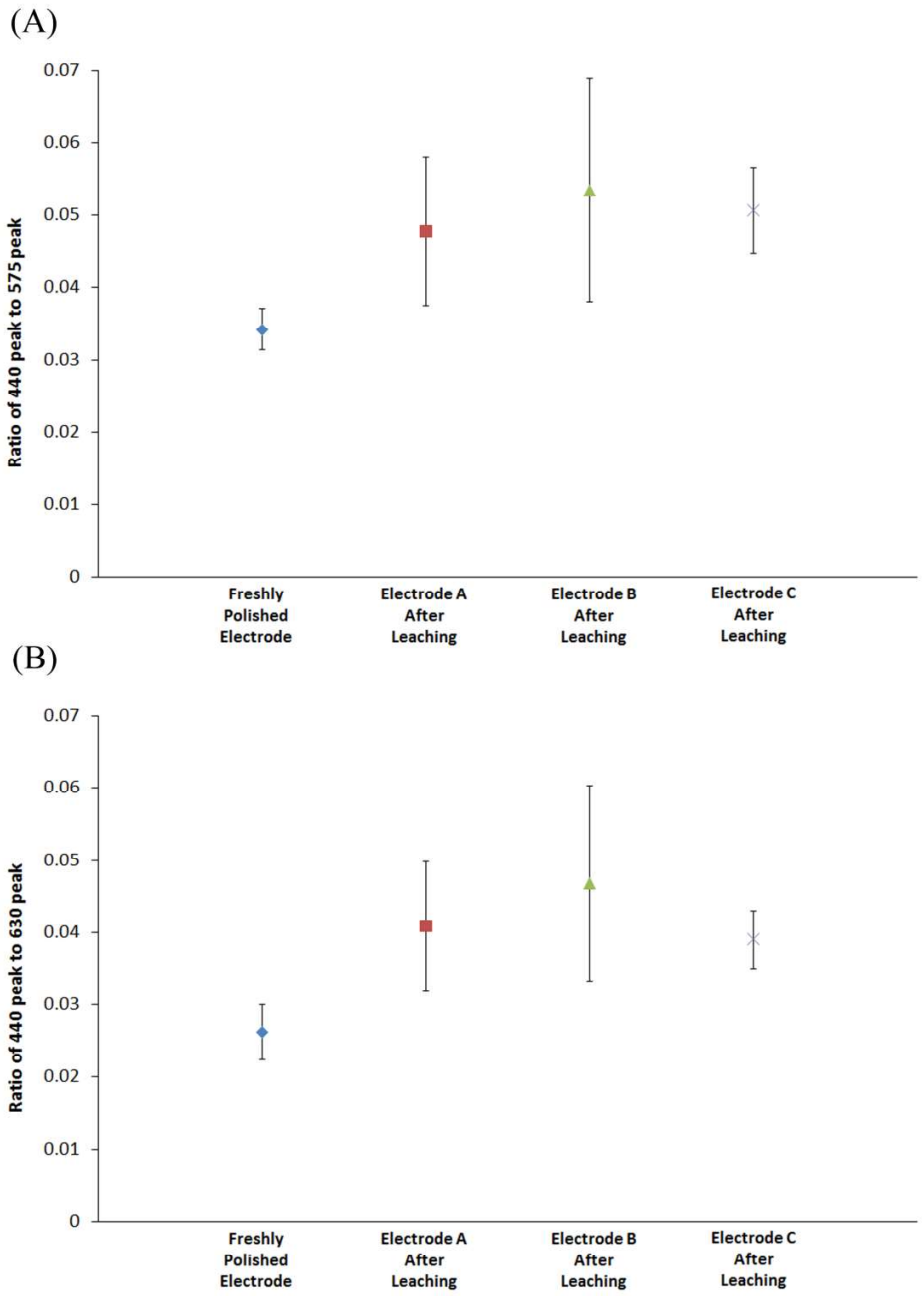

386

387 **Fig. 4.** Lorentzian peak fit results for the data of Fig. 3, assuming peak maxima at 440,
388 575 and 630 cm^{-1}. Results are expressed as a ratio of (A) the 575 cm^{-1} peak and (B) the
389 630 cm^{-1} peak to the 440 cm^{-1} peak.

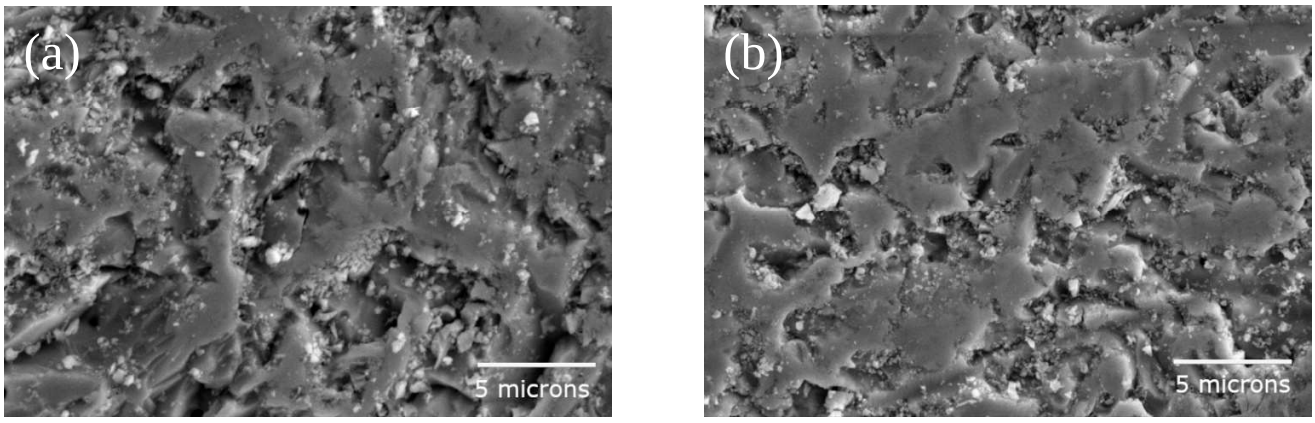

Fig 5. SEM at the surface of the (a) pre-leached UO_2 pellet after polishing and (b) the post-leached UO_2 pellet.

Comparison between Fig. 5a and Fig 5b reveals no significant differences before and after the leaching process. Furthermore, the high degree of surface roughness makes the identification of small secondary phases, such as those described for the thin film below, extremely difficult. However, comparison of the area EDX analysis of the electrodes before and after the leaching process reveals a small but measurable increase in oxygen atomic % from 45.71 (±0.23) to 46.44 (±0.35) where the uncertainties arose from the fitting. Again, this agrees with both Raman and open circuit potential measurements (see Figs. 3 and 4) that there is a small oxidation of the surface occurring due to a trace amount of ~2 ppm O_2 present in the glovebox atmosphere.

3.2. Thin film dissolution

A high-quality single-crystalline thin film (~100 nm) of UO_2 deposited on a (001) silicon single crystal substrate has been subjected to an extended anoxic dissolution test in deoxygenated deionized water under anoxic argon (0.1 O_2 ppm) atmosphere at ambient temperature (~25 °C) [25].

The advantages of UO_2 thin film dissolution over pellets or powders is that the flat morphology of the film facilitates sharper focusing in surface imaging, allowing features that will have gone unnoticed in samples with rougher surfaces to be made more apparent.

ICP-MS measurements of both the uranium dissolution vessel and the silicon wafer only vessel as a function of time are shown in Fig. 6.

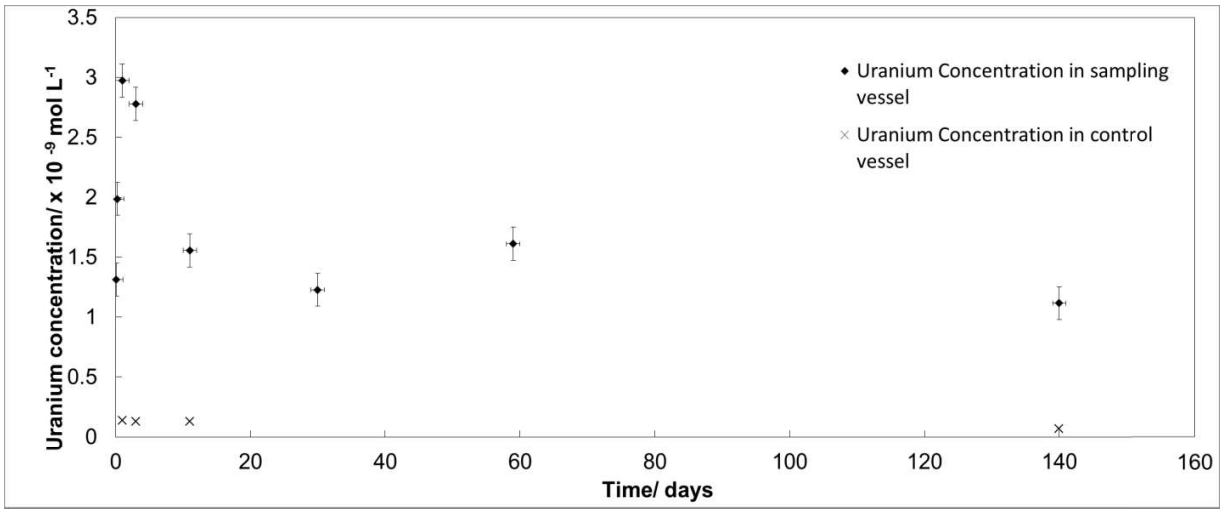

Fig. 6. Dissolved uranium concentrations of extracted aliquots from both the uranium dioxide thin film dissolution vessel and the silicon wafer only vessel (control), determined by ICP-MS.

Fig. 6 reveals uranium concentrations in the UO_2 thin film vessel are in the range of 1.2–3.0 × 10^{-9} mol/l. This is similar in order of magnitude to the uranium concentration from the pellet dissolution experiment shown in Fig. 1. The initial increase in uranium concentrations followed by a decrease and plateau concentration at >10 days dissolution time is again indicative of a secondary phase precipitation mechanism. The nature of such deposits is described in more detail in the following sections.

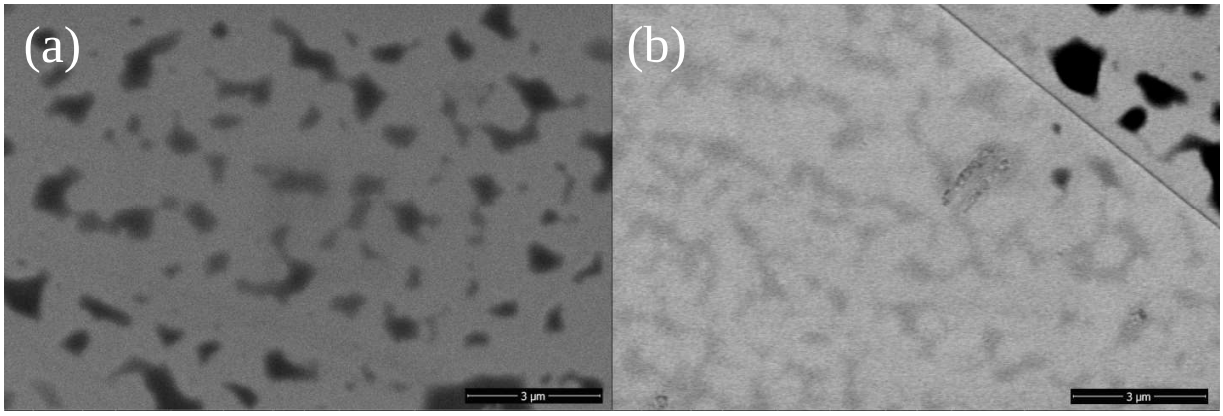

Fig. 7. (a) 30000× magnified secondary electron and (b) backscattered electron micrographs of the thin film before prewash and heat treatment.

From the pre-leaching SEM micrographs of Fig. 7, the surface is generally smooth with some trace particulates. Backscattered atomic contrast electron images (not shown) reveal that the particles are significantly darker than the uranium surface, i.e. they have a significantly lower atomic number, suggesting they are not uranium dioxide particles. A likely cause is carbon particles from the carbon tape used in the mounting.

Post-leach SEM images of a UO_2 thin film exposed to anoxic deionized water are shown in Figs. 8 and 9.

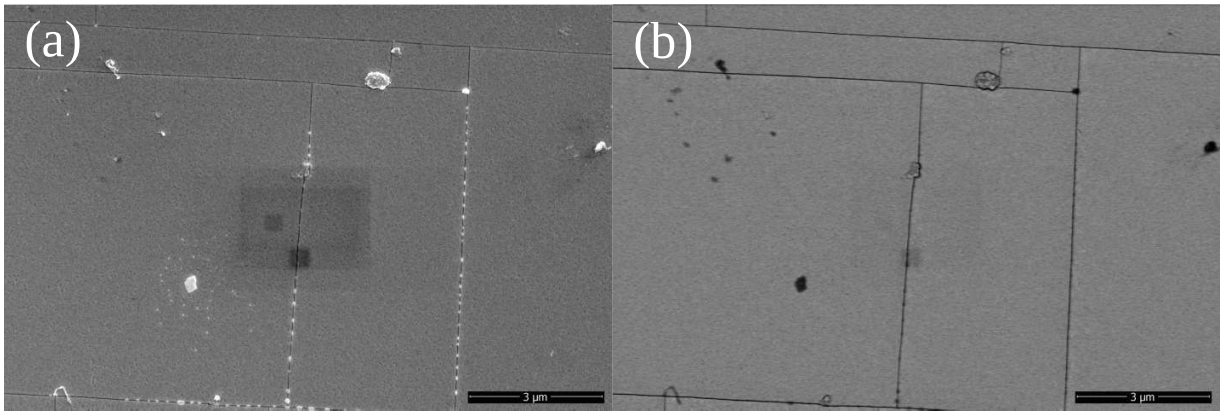

435 **Fig. 8.** (a) 30000× magnified secondary electron and (b) backscattered electron
436 micrographs of the leached thin film surface after 140 days dissolution.

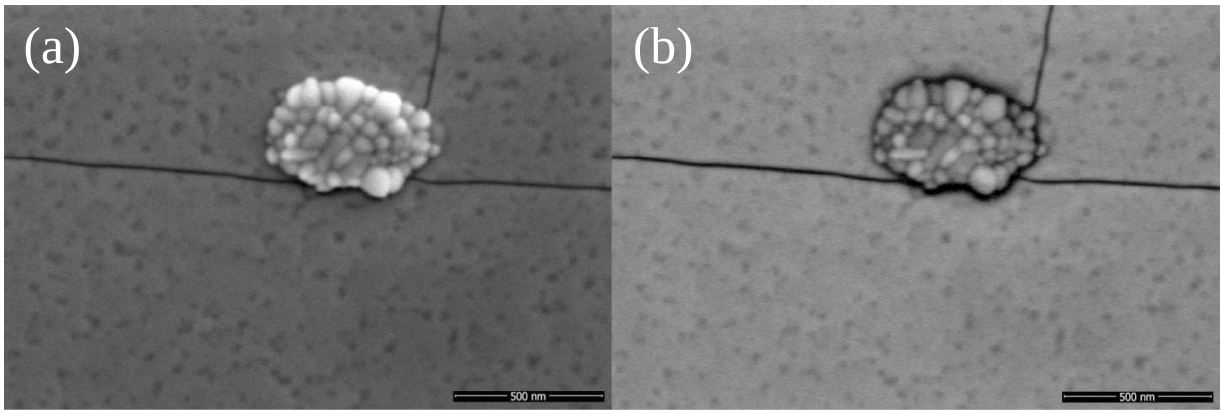

437

438 **Fig. 9.** (a) 200,000× magnification secondary electron and (b) backscattered electron
439 micrographs on the nucleate with clear growth domains ranging between 20-100 nm
440 [25].

441 From Figs. 8 and 9, there are three main differences that can be seen between
442 pre and post leaching. First, more cracks are observed. These cracks are likely due to
443 the relaxation of the stress between the substrate and thin film during the dissolution
444 process. Both structures are based on the face centred cubic structure with slight
445 differences in the lattice parameters, the uranium dioxide (fluorite type lattice) thin film
446 and the underlying silicon (diamond type lattice) substrate having lattice parameters of
447 5.47 Å [43] and 5.43 Å [44], respectively.

448 Secondly, high magnification images at 200,000× magnification (Fig. 9) enable the
449 identification of small pits (20–100 nm) where dissolution has occurred. Based on
450 previous studies, dissolution is known to initiate at energetically reactive sites [45] such
451 as point defects, dislocations terminating at the surface and so forth [46–48]. Lastly, Fig.

9 reveal the presence of circular (d = 20–100 nm) secondary phase formations preferentially nucleated at film cracks. The backscattered electron image in Fig. 9b shows that the nucleated phases have almost the same contrast as the rest of the film, which implies similarity in composition. Unfortunately, due to the small size of the individual grains a reliable EDX analysis could not be carried out to obtain compositional information on the secondary phase.

SEM imaging was also conducted on the silicon substrates in the same vessel as the UO_2 thin film, with secondary and backscattered electron images shown in Fig. 10.

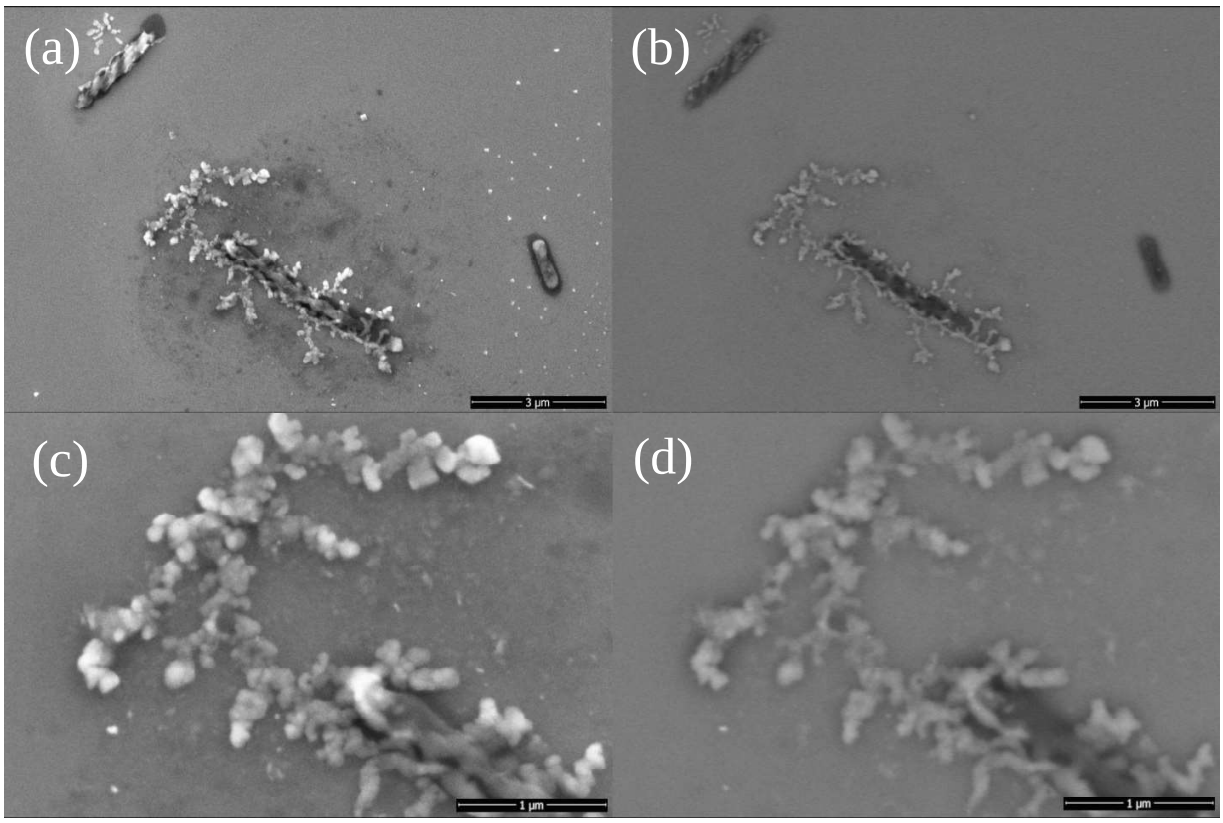

Fig. 10. Secondary (a) and backscattered electron (b) micrographs of secondary precipitates detected at 30, 000× and secondary (c) and backscattered electron (d)

463 micrographs of secondary precipitates detected on blank silicon substrates at 100, 000×
464 magnifications.

465 Fig. 10 shows some precipitates present on the silicon surface. Back-scattered
466 electron image, Fig. 10b and Fig. 10d show that the precipitates contrasted significantly
467 against the silicon substrate suggesting the precipitates have higher atomic numbers.
468 Considering the closed system of deionized water, silicon substrates and uranium thin
469 film, this implies that uranium precipitates are not just a local phenomenon found at the
470 uranium thin film surface. However, the mechanism of precipitation is postulated to be
471 different.

472 The precipitates formed on the silicon substrates differ significantly from the
473 precipitates formed on the UO_2 thin film in terms of topography and morphology. On the
474 flat silicon substrate, Fig. 10 shows clearly the presence of two types of precipitates,
475 randomly scattered particles and dendritic precipitates at the dissolution trenches and
476 pits, appearing as agglomerates of many grains (~50 nm) with different heights. Both
477 these precipitates have distinctly different morphologies from those formed on the
478 uranium thin film. Spherical UO_2 colloids have previously been reported in oxygen-
479 starved dissolution of uranium dioxide [49]. We believe the scattered particles might be
480 formed from colloidal agglomeration and precipitation [50] from dissolved uranium in the
481 solution and the dendritic growth are uranium secondary phases formed after interaction
482 with the silicon substrate at dissolution pits/trenches.

483 Despite the low ionic strength of deionized water contributing to a large kinetic barrier
484 against aggregation [51], the gravitational force on the colloids coupled with the large

difference in density between the dense uranium colloids and the surrounding fluid resulted in their precipitation after formation. Neglecting Brownian motion, Fig. 11 shows the relationship of colloidal size to settling time using sedimentation velocity calculation based on the Stokes' equation where sedimentation velocity $= \frac{g(\rho_{UO_2} - \rho_f)(d_{UO_2})2}{18\mu_f}$ (4)

where g represents the gravitational acceleration experienced by the colloid, ρ_{UO_2} represents the density of uranium dioxide, ρ_f represents the density of fluid (water), d_{UO_2} represents the diameter of uranium dioxide colloids and μ_f stands for the dynamic viscosity of water.

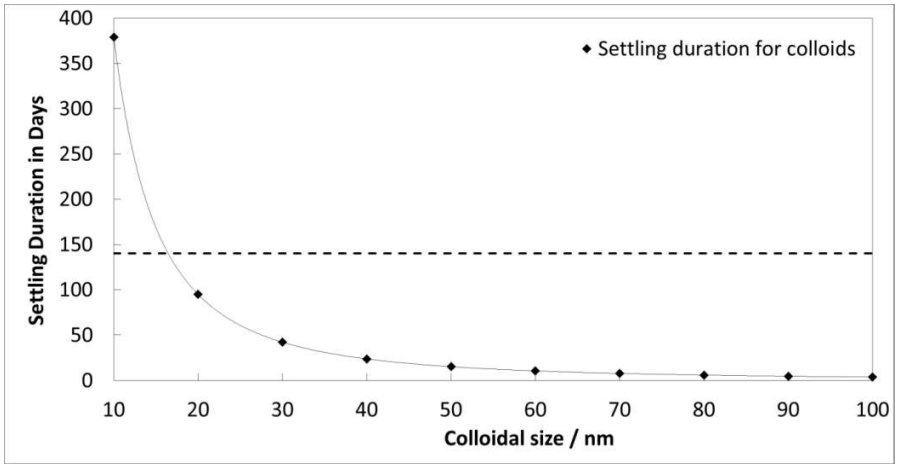

Fig. 11. Stokes' equation predicts the relationship between the settling/sedimentation duration against colloidal size for colloidal precipitation in 2 cm deep leaching vessel, similar to our set-up.

For 140 days experiments, colloid precipitation is seen to have a colloidal size limit at 15 nm. Smaller colloids will take a much longer time to settle. The velocity of

501 sedimentation was calculated to be 1.53×10^{-8} ms^{-1} for the observed ~50 nm uranium
502 dioxide colloids, achieving sedimentation after 2 cm descent (depth in our experiment)
503 in ~14 days.

504 To identify the precipitates, EBSD, EDX and XRD were attempted but no signals were
505 detected that allowed differentiation from the underlying UO_2 thin film. The lack of
506 elemental analysis opens up possible alternative interpretations for these colloids to be
507 uranium silicates, such as coffinite. Given the high solution concentration of silicon ions
508 (25 ppb or 10^{-6} mol/l Si from ICP-AES measurement of the solution after the
509 experiment), these colloids are possibly uranium silicate colloids that have been formed
510 in the near field of the silicon substrate at near neutral pH [52] if there is super
511 saturation of silicon ions of a few orders of magnitude. Our concentrations of silicate to
512 uranium concentration is quite close to that reported in the dissolution of coffinite by
513 Szenknect et al [53]. The only caveat to this interpretation is the difficulty in producing
514 coffinite at room temperature in laboratory conditions [6,52,53] where the concentration
515 of silicon is higher than our measured silicon concentrations at 10^{-4} mol/ l. It is however
516 possible that the precipitates might be precursors of coffinite.

517 The distinct morphology of the dendritic formation implies a different secondary
518 phase from that observed at the uranium thin film. From the sharp contrast from the
519 underlying silicon substrate at Fig. 10d, these grains may be preferential uranium
520 precipitation in the dissolution trenches/pits where super saturation of silicon ions is
521 possible and uranium secondary phases containing silicon, potentially uranium silicates
522 are formed.

X-ray diffraction analysis of the uranium thin film in standard Bragg-Brentano geometry is shown in Fig. 12. Unfortunately, the diffractogram of Fig. 12 does not show any signal from any secondary phases that may be present, most likely due to the low amount of material present versus the bulk UO_2 film.

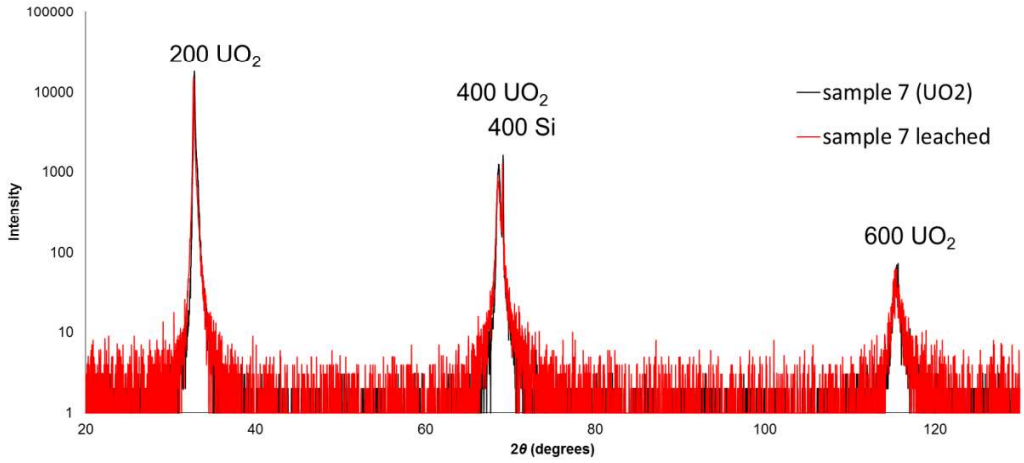

Fig. 12. XRD diffractogram for the pre-leached and post-leached UO_2 thin film sample on a silicon substrate. Only 200, 400, and 600 UO_2 reflections corresponding to the (001) crystallographic orientation are present.

Neck and Kim [21] proposed that for actinides in neutral and alkaline solutions, where $An(OH)_{4(aq)}$ are the predominant aqueous species, the solubilities of $AnO_{2(cr)}$ become equal to those of the amorphous solids. Hence, a conclusion was drawn that the crystalline dioxides are covered by amorphous hydroxide layers. Despite this, from X-ray diffraction of the pre and post-leached thin film samples (Fig. 12) and surface sensitive EBSD measurements (Fig. 14), we found that the sample of UO_2 did not amorphize during the dissolution duration of 140 days.

Finally, we observe that dissolution of the uranium dioxide thin film led to micro-crack formations seen in Figs. 8 and 9. We postulate this to result from the release of film strain due to lattice-mismatch between the uranium dioxide thin film and the underlying silicon substrate. We investigated carefully the misorientation differences between each point of the thin film surface with the help of EBSD images. MTEX, a MATLAB toolbox for quantitative texture analysis, was used to quantify the misorientation differences between individual points on the thin film to investigate this dissolution-assisted strain release micro-cracks formation in the compressively stressed thin film. Such crack formation in thin films under tensile stress has been simulated by Zhang et al [54]. These micro-cracks are distinct from previously observed, oxidative cracks [55] as we have no evidence of oxidation of UO_2 to U_3O_7 from our XRD data.

A thresholded EBSD map, Fig. 13, shows that the crystal orientation is constant throughout the grain, with virtually the entire area within 1 degree of misorientation. Next, subgrain boundaries were defined with the fast multiscale clustering (FMC) method [56] with a scaling parameter for grouping and segregating pixels into subgrains, (C_Maha of 4.8). Fig. 13 shows the subgrain features found reflect the crack morphology. By fitting a misorientation profile with a third order polynomial function we calculated a precision error (3sigma) smaller than ± 0.3° (see Electronic Supplementary Information (ESI)).

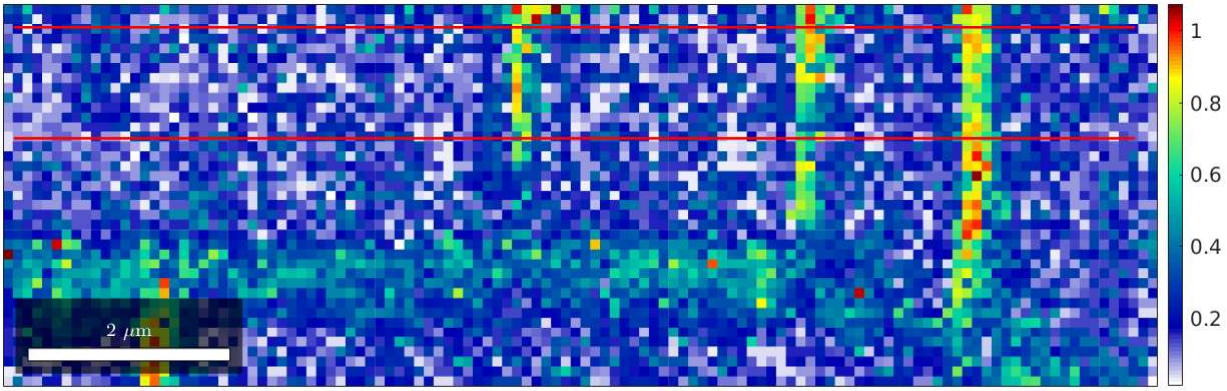

Fig. 13. Thresholded EBSD map showing the misorientation angle of every pixel with respect to the average orientation. The twelve adjacent misorientation profiles delimited by the two red curves were averaged to obtain the averaged misorientation profile of Figure 14.

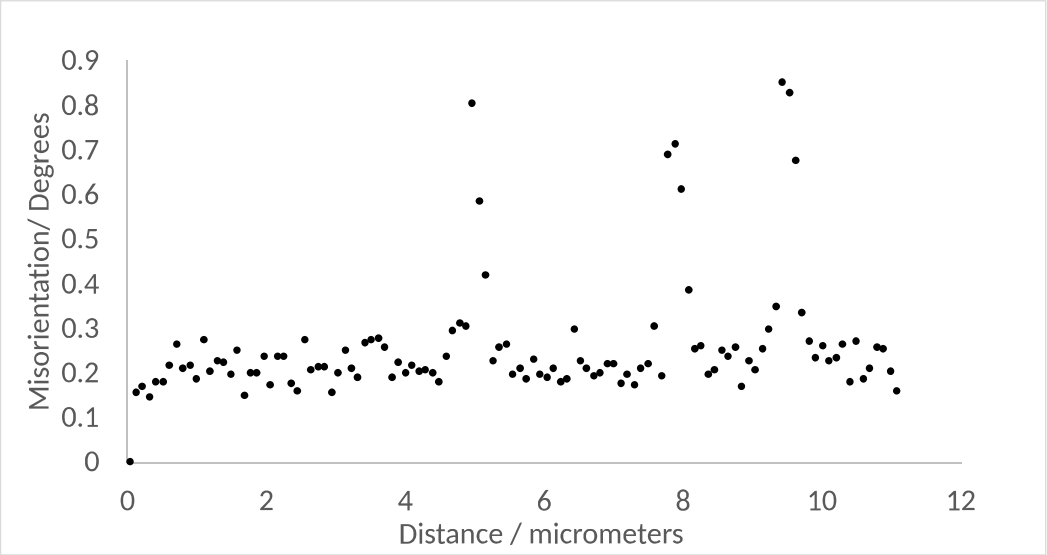

Fig. 14. Averaged misorientation profile (see Fig. 15 as a reference)

The resolution of each square pixel shown in Fig. 13 is 97 nm by 97 nm. Vertical grains with areas of two by ten pixels left and right of each crack were merged and their

average misorientation axes were calculated with respect to the immediate adjacent areas to the left. These misorientation axes are plotted in the inverse pole figure shown in Fig 15. Our data show that the misorientation axis looks relatively similar at both flanks of the cracks. With our averaging approach, we have been able to show that the misorientation axes oscillate around <111>, which is the cleavage related direction expected for a cubic fluorite structure [57]. Our interpretation is that due to the lattice mismatch between the UO_2 and the silicon substrate crystal structures, the oxide structure is distorted along the <111> cleavage directions throughout the entire thin film. This distortion becomes experimentally significant (i.e. larger than 0.3 º) at the proximity of the cracks: that is, the crack allows for a larger crystal distortion. Such distortion promotes further propagation of the cracks themselves in a positive feedback loop. This can be seen from Fig. 8 where the cracks are seen at 90º to each other, implying a <111> direction of propagation in this (001) oriented uranium dioxide thin film.

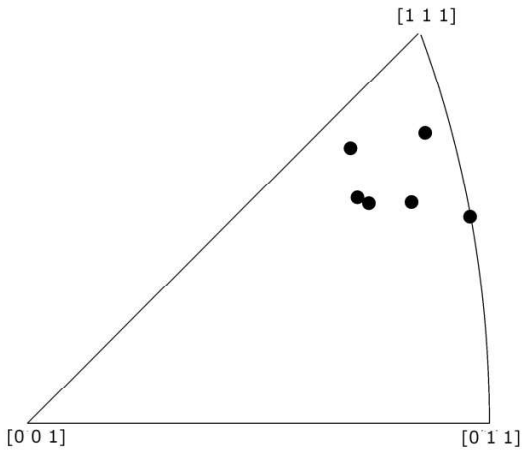

Fig. 15. Plot of misorientation axes obtained on either side of the three cracks. They have similar misorientation axis with some statistical variation.

585 *3.3. Powder samples*

586 This last experiment aims to determine the effect of temperature on uranium dioxide
587 dissolution. High surface area uranium dioxide powder was leached under varying
588 temperatures to determine the effect of temperature on uranium dioxide dissolution.
589 ICP-MS determined uranium solution concentration values from the UO_2 powder
590 leaching vessels held at different temperatures (ambient temperature (~25°C), 40 °C, 90
591 °C and 150 °C) are shown in Fig. 16. It should be noted that the aliquot extraction was
592 done at the ambient glovebox temperature of 25°C.

593 From Fig. 16, it can be seen that the concentration of dissolved uranium does not
594 vary significantly despite the different temperatures employed. In fact, the mean U
595 concentration appears to decrease from 40 °C to 150 °C. It should be noted that the
596 aliquot extraction was done a few minutes after removing the samples from the
597 autoclave and temperatures may have fallen slightly. This observation indicates that
598 increased temperatures do not increase dissolved uranium concentrations for long
599 duration dissolution. It can again be seen that the final concentrations are ~10^{-9} mol/l
600 consistent with our results on the thin film and bulk dissolution experiments at ambient
601 temperature.

602 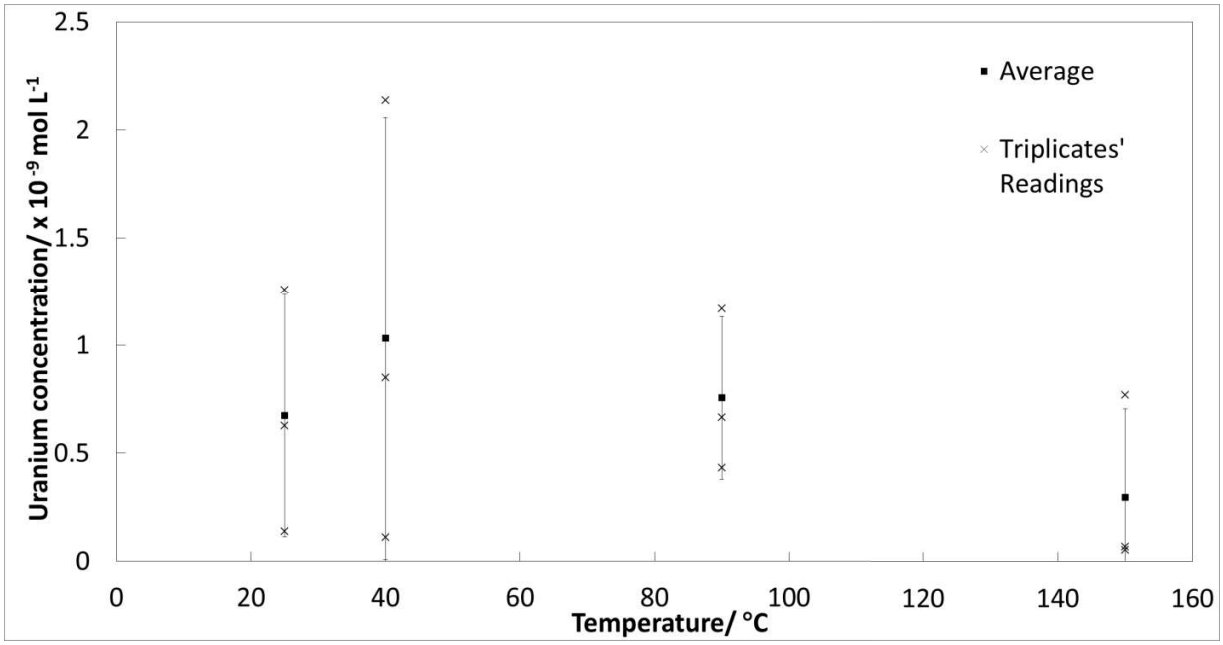

603 **Fig. 16.** ICP-MS determined uranium concentration values after 390 days of dissolution
604 at temperatures from 25 to 140 ˚C.

605 **4. Discussion**

606 *4.1. Simulations*

607 Phreeqc 3.4.0-13927 [58] calculates the equilibrium concentration of ions for a given
608 combination of reactants in solution after inputting initial conditions, such as solubility,
609 pH, Eh, concentration of dissolved oxygen and so forth. Using a referenced
610 thermodynamic database, such as Hatches [59], we estimated the equilibrium
611 concentration of dissolved uranium ions by integrating the different speciation of
612 uranium (IV, V, VI) at different concentrations of dissolved oxygen using existing
613 solubility and reaction parameters for UO_2 from the Nuclear Energy Authority (NEA)
614 database.

615

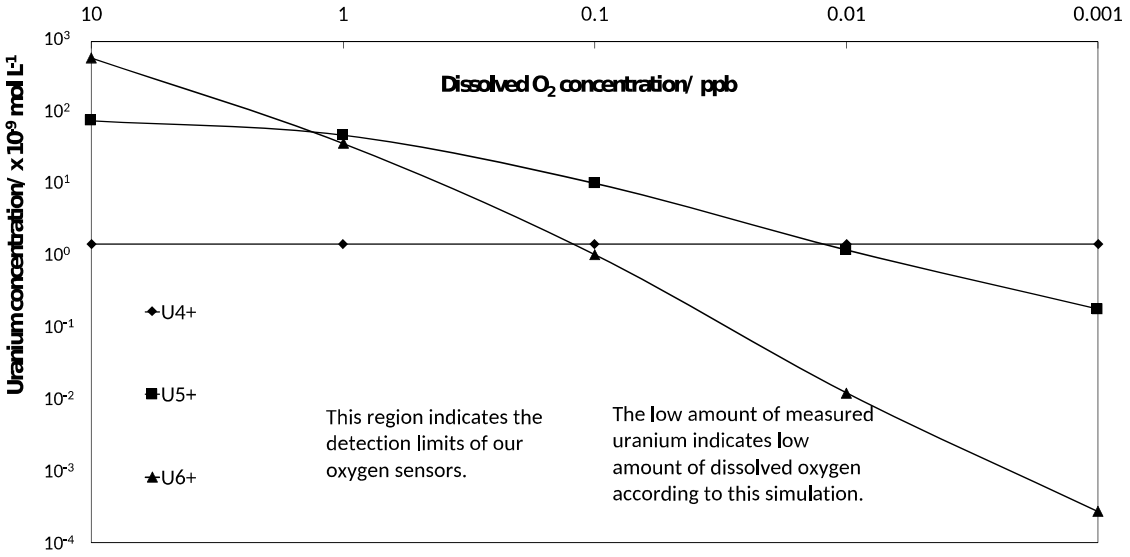

616

617 **Fig. 17.** Phreeqc simulation of dissolved uranium concentration at equilibrium as a
618 function of oxygen content for UO_2 (NEA) dissolution in deionized water at room
619 temperature, where log K^0 of UO_2 = 54.5 ± 1.0.

620 Given a starting condition of stoichiometric tetravalent uranium dioxide, oxidation of
621 uranium dioxide, U(IV)O_2 to U^{5+} and U^{6+} are dominant in solution at concentrations of
622 dissolved oxygen above 0.1 ppb. Based on the highest dissolved uranium concentration
623 readings in all our experiments (see Fig. 1) of about 6 × 10^{-9} mol/L, we can relate that
624 the upper limit of dissolved oxygen in our system is about 0.1 ppb.

625 Simulations show constant equilibrium concentration of tetravalent uranium at these
626 low levels of dissolved oxygen indicating that anoxic dissolution of uranium dioxide in its
627 tetravalent form proceeds invariably at a limiting rate due to low associated solubility
628 and such tetravalent dissolution becomes dominant at low levels of dissolved oxygen for

629 stoichiometric uranium dioxide where oxidation of uranium dioxide to higher oxidation
630 levels is seen to drop off sharply according to these thermodynamic calculations.

631 *4.2. Experimental discussions*

632 There is some variability in reported uranium concentrations for the anoxic dissolution
633 of uranium dioxide, ranging from 10^{-7} mol/L to 10^{-10} mol/L [21] and these have been
634 noted by NEA [60] to result from a range of solids with different thermodynamic
635 stabilities. The common theme from the results of this series of experiments, with
636 different physical forms of UO_2, is that the dissolved uranium concentration is ~10^{-9}
637 mol/l and in all cases less than 10^{-8} mol/l, for all physical forms when care is taken to
638 control the oxygen content of the water and therefore oxidation potential of the water.
639 Thermodynamic calculations indicate that concentrations in this range represent the
640 solubility limit of uranium in its tetravalent oxidation state.

641 For the first time, well-defined growth of precipitates at low uranium concentration
642 was observed [25]. This contradicts the notion of an oxidative dissolution mechanism for
643 U with it transforming to hexavalent form prior to dissolution, as U^{6+} has solubility limits
644 (~10^{-6} mol/l) [3] that are 3 orders of magnitude higher than the U concentration values
645 observed (~10^{-9} mol/l). This difference in solubilities is also observed with anoxic
646 dissolution as ICP-MS results from pre-washes are noted to contain a higher
647 concentration of uranium, which we attribute to preferential dissolution of U^{5+} and U^{6+} in
648 slightly oxidized uranium dioxide.

649 The low concentration of dissolved uranium ions and the high solubility of hexavalent
650 uranium implies that no secondary phase formation should take place at this

concentration if dissolution was going through the hexavalent pathway. Hence, the observation of these uranium precipitates leads us to conclude that anoxic dissolution of uranium must proceed through the tetravalent phase.

We put forward that the anoxic dissolution of stoichiometric uranium over time is made up of two simultaneous and competing processes:

1) A widely-accepted mechanism [3] dissolved oxygen-dependent transformation of $U(IV)_{(solid)}$ to $U(V,VI)_{(solid)}$ then $U(VI)_{(aqueous)}$,

This will lead to $U(VI)_{(precipitates)}$ at a high concentration of dissolved uranium ions at its solubility limit, as in the case of oxic dissolution.

We observe a small amount of transformation of uranium to higher oxidation states indirectly through the increase in oxygen levels with EDX at the surface of our solid pellet electrode dissolution experiments and from Raman evidence of higher numbers of interstitial oxygens in leached samples, but not a significant increase in the dissolved uranium concentration.

2) A proposed non-oxygen dependent [25] $U(IV)_{(solid)}$ to $U(IV)_{(aqueous)}$ then $U(IV)_{(precipitates)}$

process 2 has been demonstrated to prevail in our sets of anoxic experiments and thus has significance in real-life nuclear repositories which are expected be anoxic [2].

From the solid pellet experiment, it can be concluded that in anoxic dissolution with low levels of oxygen at 2.0 ppm O_2, it is still possible to observe surface oxidation

671 indirectly from Raman spectroscopy inferences, open circuit potential and EDX
672 measurements. Despite this, the dissolved uranium concentration remains low at 6 × 10-
673 9 mol/l, which is an indication that mainly tetravalent uranium ions are present in solution
674 with their characteristic low solubility. However, with pellet studies the higher surface
675 roughness inhibits clear observations of any secondary phases that may be formed.
676 Nevertheless, we have observed from ICP-MS results of the acid post-washes of the
677 leaching vessel, an average of 3 × 10^{-9} mol/l of dissolved uranium in 250 cm^3 of 3.0 M
678 nitric acid. This highlights the presence of uranium sorption/precipitation on the wall of
679 the PTFE vessels as observed before [10,61].

680 Considering an accidental container corrosion scenario of 500-1000 years when
681 container will fail to be water tight and groundwater ingresses, the temperature of spent
682 nuclear fuel interacting with groundwater will be higher than the prevailing underground
683 repository temperatures depending on the fuel burn-up and the waste canisters. Thus,
684 temperatures in the vicinity of the spent nuclear fuel will vary from ~45 ºC to ~130 ºC
685 [62].

686 High-surface area powder dissolution conducted at elevated temperatures for 390
687 days showed uranium concentrations falling within a range between 0.1 × 10^{-9} to
688 2 × 10^{-9} mol/l. We notice a slight decrease in the mean dissolved uranium
689 concentrations at higher temperatures, albeit within the error bars. Although, it should
690 be noted that the aliquot extraction was performed at an ambient glove box temperature
691 of ~25 °C.

692 Slightly higher concentration of dissolved uranium concentrations in the solid pellet
693 experiment (6.0×10^{-9} mol/l) might be attributed to a thin layer of higher oxidized
694 uranium on its surface as these samples were not annealed in a reducing environment
695 like the others with values of about 3.0×10^{-9} mol/l. Since the uranium concentration
696 values in the contact solutions were essentially of the same order of magnitude ($\sim 10^{-9}$
697 mol/l) for the pellet, thin film and powder samples, and formation of a uranium
698 containing secondary phase took place, it can be suggested that the equilibrium
699 uranium concentration in the solution is limited by the solubility of the nucleating
700 secondary phase and is independent of the UO_2 form (bulk pellet, thin film or powder).
701 Just as schoepite's solubility [35] forms the upper limit of uranium dissolution in oxic
702 conditions, the limitation of uranium dioxide dissolution in anoxic conditions will be
703 limited by solubility of these uranium (IV) secondary nucleates. Hence, parameters such
704 as specific surface area, density of reactive surface sites, particle sizes and sample
705 crystallinity (amorphous vs. crystalline) should not affect the uranium concentration
706 established in the solution in the long-term and may only affect the kinetic aspects of the
707 process [63].

708 **5. Conclusions**

709 For extended durations up to 390 days, we conclude that the baseline scenario of
710 uranium dioxide dissolution in deionized water will result in dissolved uranium dioxide
711 concentration of the order of 10^{-9} mol/l, which is indicative of U^{4+} dissolution. Relatively
712 slight variation in uranium concentrations of less than one order of magnitude is
713 observed between different sets of UO_2 samples (pellets, thin film and powder).

Variable temperature dissolution was conducted over a duration of 390 days and the concentration of dissolved uranium did not increase with elevated temperatures.

The dissolved uranium concentration of these long-term anoxic uranium dissolution experiments went through a maximum before decreasing to a constant value being indicative of a dissolution and precipitation mechanism, which is verified by the observed uranium containing secondary phases. At such low dissolved uranium concentration, dissolution and precipitation of uranium is hypothesized to proceed through the tetravalent form. This hypothesis is reinforced by clear observations of clusters (~500 nm) of homogenous uranium-containing precipitates of 20–100 nm grains in the thin film dissolution experiment.

From these experiments, we conclude that anoxic uranium dissolution with deionized water proceeds in 2 forms simultaneously at the surface.

1) a dissolved oxygen-dependent step of $U(IV)_{(solid)}$ to $U(V, VI)_{(solid)}$ then $U(VI)_{(aqueous)}$

2) a non oxygen-dependent $U(IV)_{(solid)}$ to $U(IV)_{(aqueous)}$ process to $U(IV)_{(precipitates)}$

We proposed that the equation for process 2 will take the following form:

$$UO_{2(s,\ \text{defective})} + 2H_2O_{(l)} \rightarrow U(OH)_{4(aqueous)} \rightleftharpoons UO_{2(s,\ \text{less defective})} + 2H_2O_{(l)},\ \Delta H < 0 \quad (5)$$

Acknowledgements

We would like to acknowledge the Singapore Nuclear Research and Safety Initiative for partial funding. We would also like to acknowledge Thomas Gouder, Rachel Eloirdi, Alice Seibert from the European Commission, Joint Research Centre, Directorate for Nuclear Safety and Security for providing the thin film sample. Lastly, we will also like to express our thanks for being able to use the UTGARD National Nuclear User Facility (NNUF) for some of our experiments.

Conflicts of interests

There are no conflicts of interests to declare.

Data Availability

The raw/processed data required to reproduce these findings cannot be shared at this time as the data also forms part of an ongoing study. However, additional information on EBSD data processing has been included in the electronic supplementary information.

References

[1] MIT, The Future of the Nuclear Fuel Cycle, 2011. http://medcontent.metapress.com/index/A65RM03P4874243N.pdf%0Ahttps://mitei.mit.edu/system/files/The_Nuclear_Fuel_Cycle-all.pdf.

[2] D. Cui, E. Ekeroth, P. Fors, K. Spahiu, The Interaction of Dissolved Hydrogen with Spent Fuel or UO2 Doped with Alpha, in: Mater. Res. Soc. Symp. Proc., 2008.

[3] D.W. Shoesmith, Fuel corrosion processes under waste disposal conditions, J. Nucl. Mater. 282 (2000) 1–31. doi:10.1016/S0022-3115(00)00392-5.

[4] H. He, M. Broczkowski, K.O. Neil, D. Ofori, D. Shoesmith, Corrosion of nuclear

757 fuel (UO2) inside a failed nuclear waste container | NWMO TR-2012-09, 2012.

758 [5] K. Ollila, M. Olin, M. Lipponen, Solubility and Oxidation State of Uranium under
759 Anoxic Conditions (N 2 Atmosphere), Radiochim. Acta. 74 (1996) 9–13.
760 https://www.degruyter.com/downloadpdf/j/ract.1996.74.issue-
761 s1/ract.1996.74.special-issue.9/ract.1996.74.special-issue.9.pdf.

762 [6] M. Amme, T. Wiss, H. Thiele, P. Boulet, H. Lang, Uranium secondary phase
763 formation during anoxic hydrothermal leaching processes of UO2 nuclear fuel, J.
764 Nucl. Mater. 341 (2005) 209–223. doi:10.1016/j.jnucmat.2005.02.004.

765 [7] T. Mennecart, B. Grambow, M. Fattahi, Z. Andriambololona, Effect of alpha
766 radiolysis on doped UO2 dissolution under reducing conditions, Radiochim. Acta.
767 92 (2004) 611–615. doi:10.1524/ract.92.9.611.55010.

768 [8] J. Bruno, I. Casas, I. Puigdomènech, UO 2 under reducing conditions and the
769 influence of an oxidized surface layer (UO 2+ x): Application of a continuous flow-
770 through reactor, Geochim. Cosmochim. Acta. 55 (1991) 647–658.
771 doi:10.1016/0016-7037(91)90330-8.

772 [9] A.J. Popel, V.G. Petrov, V.A. Lebedev, J. Day, S.N. Kalmykov, R. Springell, T.B.
773 Scott, I. Farnan, The effect of fission-energy Xe ion irradiation on dissolution of
774 UO2 thin films, J. Alloys Compd. 721 (2017) 586–592.
775 doi:10.1016/j.jallcom.2017.05.084.

776 [10] A.J. Popel, T.W. Wietsma, M.H. Engelhard, A.S. Lea, O. Qafoku, C. Grygiel, I.
777 Monnet, E.S. Ilton, M.E. Bowden, I. Farnan, The effect of ion irradiation on the

778 dissolution of UO2 and UO2-based simulant fuel, J. Alloys Compd. 735 (2018)
779 1350–1356. doi:10.1016/j.jallcom.2017.11.216.

780 [11] H. He, Z. Qin, D.W. Shoesmith, Characterizing the relationship between
781 hyperstoichiometry, defect structure and local corrosion kinetics of uranium
782 dioxide, Electrochim. Acta. 56 (2010) 53–60. doi:10.1016/j.electacta.2010.09.064.

783 [12] D. Serrano-Purroy, F. Clarens, E. González-Robles, J.P. Glatz, D.H. Wegen, J.
784 De Pablo, I. Casas, J. Giménez, A. Martínez-Esparza, Instant release fraction and
785 matrix release of high burn-up UO2spent nuclear fuel: Effect of high burn-up
786 structure and leaching solution composition, J. Nucl. Mater. 427 (2012) 249–258.
787 doi:10.1016/j.jnucmat.2012.04.036.

788 [13] K. Lemmens, E. González-Robles, B. Kienzler, E. Curti, D. Serrano-Purroy, R.
789 Sureda, A. Martínez-Torrents, O. Roth, E. Slonszki, T. Mennecart, I. Günther-
790 Leopold, Z. Hózer, Instant release of fission products in leaching experiments with
791 high burn-up nuclear fuels in the framework of the Euratom project FIRST-
792 Nuclides, J. Nucl. Mater. 484 (2017) 307–323. doi:10.1016/j.jnucmat.2016.10.048.

793 [14] K.U. Ulrich, E.S. Ilton, H. Veeramani, J.O. Sharp, R. Bernier-Latmani, E.J.
794 Schofield, J.R. Bargar, D.E. Giammar, Comparative dissolution kinetics of
795 biogenic and chemogenic uraninite under oxidizing conditions in the presence of
796 carbonate, Geochim. Cosmochim. Acta. 73 (2009) 6065–6083.
797 doi:10.1016/j.gca.2009.07.012.

798 [15] D.W. Shoesmith, S. Sunder, The prediction of nuclear fuel (UO2) dissolution rates

799 under waste disposal conditions, J. Nucl. Mater. 190 (1992) 20–35.
800 doi:10.1016/0022-3115(92)90072-S.

801 [16] M. Altmaier, E. Yalçıntaş, X. Gaona, V. Neck, R. Müller, M. Schlieker, T.
802 Fanghänel, Solubility of U(VI) in chloride solutions. I. The stable
803 oxides/hydroxides in NaCl systems, solubility products, hydrolysis constants and
804 SIT coefficients, J. Chem. Thermodyn. 114 (2017) 2–13.
805 doi:10.1016/j.jct.2017.05.039.

806 [17] M. Pijolat, C. Brun, F. Valdivieso, M. Soustelle, Reduction of uranium oxide U3O8
807 to UO2 by hydrogen, Solid State Ionics. 101–103 (1997) 931–935.
808 doi:10.1016/S0167-2738(97)00385-8.

809 [18] G. Leinders, Low-Temperature Oxidation of Fine Uo 2 Powders: Thermochemistry
810 and Kinetics, Inorg. Chem. 9 (2018) 2–10. doi:10.1021/acs.inorgchem.8b00517.

811 [19] B.J.S. Anderson, L.E.J. Roberts, E.A. Harper, Aszderson, Roberts, and Hayper :
812 The Oxides, (1949).

813 [20] Z. Hiezl, D.I. Hambley, C. Padovani, W.E. Lee, Processing and microstructural
814 characterisation of a UO2-based ceramic for disposal studies on spent AGR fuel,
815 J. Nucl. Mater. 456 (2015) 74–84. doi:10.1016/j.jnucmat.2014.09.002.

816 [21] V. Neck, J.I. Kim, Solubility and hydrolysis of tetravalent actinides, Radiochim.
817 Acta. 89 (2001) 1–16. doi:10.1524/ract.2001.89.1.001.

818 [22] D. Rai, A.R. Felmy, J.L. Ryan, Uranium(IV) Hydrolysis Constants and Solubility

819 Product of UO2·x*H2O(am), Inorg. Chem. 29 (1990) 260–264.
820 doi:10.1021/ic00327a022.

821 [23] K. Fujiwara, H. Yamana, T. Fujii, K. Kawamoto, T. Sasaki, H. Moriyama, Solubility
822 product of hexavalent uranium hydrous oxide, J. Nucl. Sci. Technol. 42 (2005)
823 289–294. doi:10.1080/18811248.2005.9726392.

824 [24] K. Opel, S. Weiß, S. Hübener, H. Zänker, G. Bernhard, Study of the solubility of
825 amorphous and crystalline uranium dioxide by combined spectroscopic methods,
826 Radiochim. Acta. 95 (2007) 143–149. doi:10.1524/ract.2007.95.3.143.

827 [25] A.J. Popel, B.T. Tan, T. Gouder, G.I. Lampronti, J. Day, R. Eloirdi, A. Seibert, I.
828 Farnan, Surface alteration evidence for a mechanism of anoxic dissolution of
829 UO2, Appl. Surf. Sci. 464 (2019) 376–379. doi:/10.1016/j.apsusc.2018.09.094.

830 [26] A. Fernández, D. Haas, R.J.M. Konings, J. Somers, Transmutation of actinides, J.
831 Am. Ceram. Soc. 85 (2002) 694–696.

832 [27] M. Cologna, V. Tyrpekl, M. Ernstberger, S. Stohr, J. Somers, Sub-micrometre
833 grained UO2 pellets consolidated from sol gel beads using spark plasma sintering
834 (SPS), Ceram. Int. 42 (2016) 6619–6623. doi:10.1016/J.CERAMINT.2015.12.172.

835 [28] J.M. Elorrieta, L.J. Bonales, M. Naji, D. Manara, V.G. Baonza, J. Cobos, Laser-
836 induced oxidation of UO_2: A Raman study, J. Raman Spectrosc. (2018) 878–
837 884. doi:10.1002/jrs.5347.

838 [29] F. Bachmann, R. Hielscher, H. Schaeben, Texture Analysis with MTEX – Free

839 and Open Source Software Toolbox, Solid State Phenom. 160 (2010) 63–68.
840 doi:10.4028/www.scientific.net/SSP.160.63.

841 [30] N. The MathWorks, MATLAB 2016a, (2016).

842 [31] G. Bruker Nano GmbH, Berlin, QUANTAX CrystAlign., (2010).

843 [32] K.I. Maslakov, Y.A. Teterin, A.J. Popel, A.Y. Teterin, K.E. Ivanov, S.N. Kalmykov,
844 V.G. Petrov, R. Springell, T.B. Scott, I. Farnan, XPS study of the surface
845 chemistry of UO2 (111) single crystal film, Appl. Surf. Sci. 433 (2018) 582–588.
846 doi:10.1016/j.apsusc.2017.10.019.

847 [33] S. Sunder, D.W. Shoesmith, M.G. Bailey, F.W. Stanchell, N.S. McIntyre, Anodic
848 oxidation of UO2. Part I. Electrochemical and X-ray photoelectron spectroscopic
849 studies in neutral solutions, J. Electroanal. Chem. 130 (1981) 163–179.
850 doi:10.1016/S0022-0728(81)80384-1.

851 [34] R.J. Wilbraham, C. Boxall, D.T. Goddard, R.J. Taylor, S.E. Woodbury, The effect
852 of hydrogen peroxide on uranium oxide films on 316L stainless steel, J. Nucl.
853 Mater. 464 (2015) 86–96. doi:10.1016/j.jnucmat.2015.04.007.

854 [35] E. Cera, M. Grivé, J. Bruno, K. Ollila, Modelling of the U0 2 dissolution
855 mechanisms in synthetic groundwater solutions Dissolution experiments carried
856 out under oxic conditions, 2001.

857 [36] J.M. Elorrieta, L.J. Bonales, N. Rodríguez-Villagra, V.G. Baonza, J. Cobos, A
858 detailed Raman and X-ray study of UO2+x oxides and related structure

transitions, Phys. Chem. Chem. Phys. 18 (2016) 28209–28216. doi:10.1039/C6CP03800J.

[37] H. He, D. Shoesmith, Raman spectroscopic studies of defect structures and phase transition in hyper-stoichiometric UO2+x, Phys. Chem. Chem. Phys. 12 (2010) 8108. doi:10.1039/b925495a.

[38] G.C. Allen, I.S. Butler, Nguyen Anh Tuan, Characterisation of uranium oxides by micro-Raman spectroscopy, J. Nucl. Mater. 144 (1987) 17–19. doi:10.1016/0022-3115(87)90274-1.

[39] M. Razdan, D.W. Shoesmith, Influence of Trivalent-Dopants on the Structural and Electrochemical Properties of Uranium Dioxide (UO2), J. Electrochem. Soc. 161 (2013) H105–H113. doi:10.1149/2.047403jes.

[40] G. Guimbretière, L. Desgranges, A. Canizarès, R. Caraballo, F. Duval, N. Raimboux, R. Omnée, M.R. Ammar, C. Jégou, P. Simon, In situ Raman monitoring of He2+ irradiation induced damage in a UO2 ceramic, Appl. Phys. Lett. 103 (2013). doi:10.1063/1.4816285.

[41] O.A. Maslova, G. Guimbretière, M.R. Ammar, L. Desgranges, C. Jégou, A. Canizarès, P. Simon, Raman imaging and principal component analysis-based data processing on uranium oxide ceramics, Mater. Charact. 129 (2017) 260–269. doi:10.1016/j.matchar.2017.05.015.

[42] L. Desgranges, G. Baldinozzi, P. Simon, G. Guimbretière, A. Canizares, Raman spectrum of U 4O 9: A new interpretation of damage lines in UO 2, J. Raman

880 Spectrosc. 43 (2012) 455–458. doi:10.1002/jrs.3054.

881 [43] G. Leinders, T. Cardinaels, K. Binnemans, M. Verwerft, Accurate lattice
882 parameter measurements of stoichiometric uranium dioxide, J. Nucl. Mater. 459
883 (2015) 135–142. doi:10.1016/j.jnucmat.2015.01.029.

884 [44] Y. Okada, Y. Tokumaru, Precise determination of lattice parameter and thermal
885 expansion coefficient of silicon between 300 and 1500 K, J. Appl. Phys. 56 (1984)
886 314–320. doi:10.1063/1.333965.

887 [45] C.L. Corkhill, D.J. Bailey, F.Y. Tocino, M.C. Stennett, J.A. Miller, J.L. Provis, K.P.
888 Travis, N.C. Hyatt, Role of Microstructure and Surface Defects on the Dissolution
889 Kinetics of CeO2, a UO2 Fuel Analogue, ACS Appl. Mater. Interfaces. 8 (2016)
890 10562–10571. doi:10.1021/acsami.5b11323.

891 [46] C.L. Corkhill, E. Myllykylä, D.J. Bailey, S.M. Thornber, J. Qi, P. Maldonado, M.C.
892 Stennett, A. Hamilton, N.C. Hyatt, Contribution of energetically reactive surface
893 features to the dissolution of CeO2 and ThO2 analogues for spent nuclear fuel
894 microstructures, ACS Appl. Mater. Interfaces. 6 (2014) 12279–12289.
895 doi:10.1021/am5018978.

896 [47] W. Stumm, Reactivity at the mineral-water interface: Dissolution and inhibition,
897 Colloids Surfaces A Physicochem. Eng. Asp. 120 (1997) 143–166.
898 doi:10.1016/S0927-7757(96)03866-6.

899 [48] U. Schwertmann, T.U. Miinchen, Solubility and dissolution of iron oxides, (1991)
900 1–25.

[49] M.D. Kaminski, N.M. Dimitrijevic, C.J. Mertz, M.M. Goldberg, Colloids from the aqueous corrosion of uranium nuclear fuel, J. Nucl. Mater. 347 (2005) 77–87. doi:10.1016/j.jnucmat.2005.07.009.

[50] H. Zänker, C. Hennig, Colloid-borne forms of tetravalent actinides: A brief review, J. Contam. Hydrol. 157 (2014) 87–105. doi:10.1016/j.jconhyd.2013.11.004.

[51] P.C. Hiemenz, R. Rajagopalan, Surface Tension and Contact Angle: Application to Pure Substances, 1997. doi:10.1201/9781315274287.

[52] I. Dreissig, S. Weiss, C. Hennig, G. Bernhard, H. Zänker, Formation of uranium(IV)-silica colloids at near-neutral pH, Geochim. Cosmochim. Acta. 75 (2011) 352–367. doi:10.1016/j.gca.2010.10.011.

[53] S. Szenknect, A. Mesbah, T. Cordara, N. Clavier, H.P. Brau, X. Le Goff, C. Poinssot, R.C. Ewing, N. Dacheux, First experimental determination of the solubility constant of coffinite, Geochim. Cosmochim. Acta. 181 (2016) 36–53. doi:10.1016/j.gca.2016.02.010.

[54] T.Y. Zhang, M.H. Zhao, Equilibrium depth and spacing of cracks in a tensile residual stressed thin film deposited on a brittle substrate, Eng. Fract. Mech. 69 (2002) 589–596. doi:10.1016/S0013-7944(01)00098-4.

[55] L. Desgranges, H. Palancher, M. Gamaléri, J.S. Micha, V. Optasanu, L. Raceanu, T. Montesin, N. Creton, Influence of the U_3O_7 domain structure on cracking during the oxidation of UO_2, J. Nucl. Mater. 402 (2010) 167–172. doi:10.1016/j.jnucmat.2010.05.014.

[56] C. McMahon, B. Soe, A. Loeb, A. Vemulkar, M. Ferry, L. Bassman, Boundary identification in EBSD data with a generalization of fast multiscale clustering, Ultramicroscopy. 133 (2013) 16–25. doi:10.1016/j.ultramic.2013.04.009.

[57] E.J.. Whittaker, Cleavage energies of minerals, Mineral. Mag. 46 (1982) 398–9.

[58] D.L. Parkhurst, C.A.. Appelo, Description of input and examples for PHREEQC version 3-- A computer program for speciation, batch- reaction, one- dimensional transport, and inverse geochemical calculations, 2013.

[59] J.E. Cross, F.T. Ewart, Hatches — A Thermodynamic Database And Management System, Radiochim. Acta. 52–53 (1991) 421–422. doi:10.1524/ract.1991.5253.2.421.

[60] I. Grenthe, J. Fuger, R.J. Lemire, A.B. Muller, H. Wanner, I. Forest, Chemical Thermodynamics of Uranium, 1992. (1992) 715. doi:10.1063/1.473182.

[61] P. Carbol, P. Fors, S. Van Winckel, K. Spahiu, Corrosion of irradiated MOX fuel in presence of dissolved H2, J. Nucl. Mater. 392 (2009) 45–54. doi:10.1016/j.jnucmat.2009.03.044.

[62] S.Y. Yang, H.D. Yeh, Modeling transient heat transfer in nuclear waste repositories, J. Hazard. Mater. 169 (2009) 108–112. doi:10.1016/j.jhazmat.2009.03.068.

[63] O.N. Batuk, Behaviour of Uranium Dioxide under Oxidative Hydrothermal Conditions, PhD Thesis, Lomonosov Moscow Sate Univ. (2007).

942

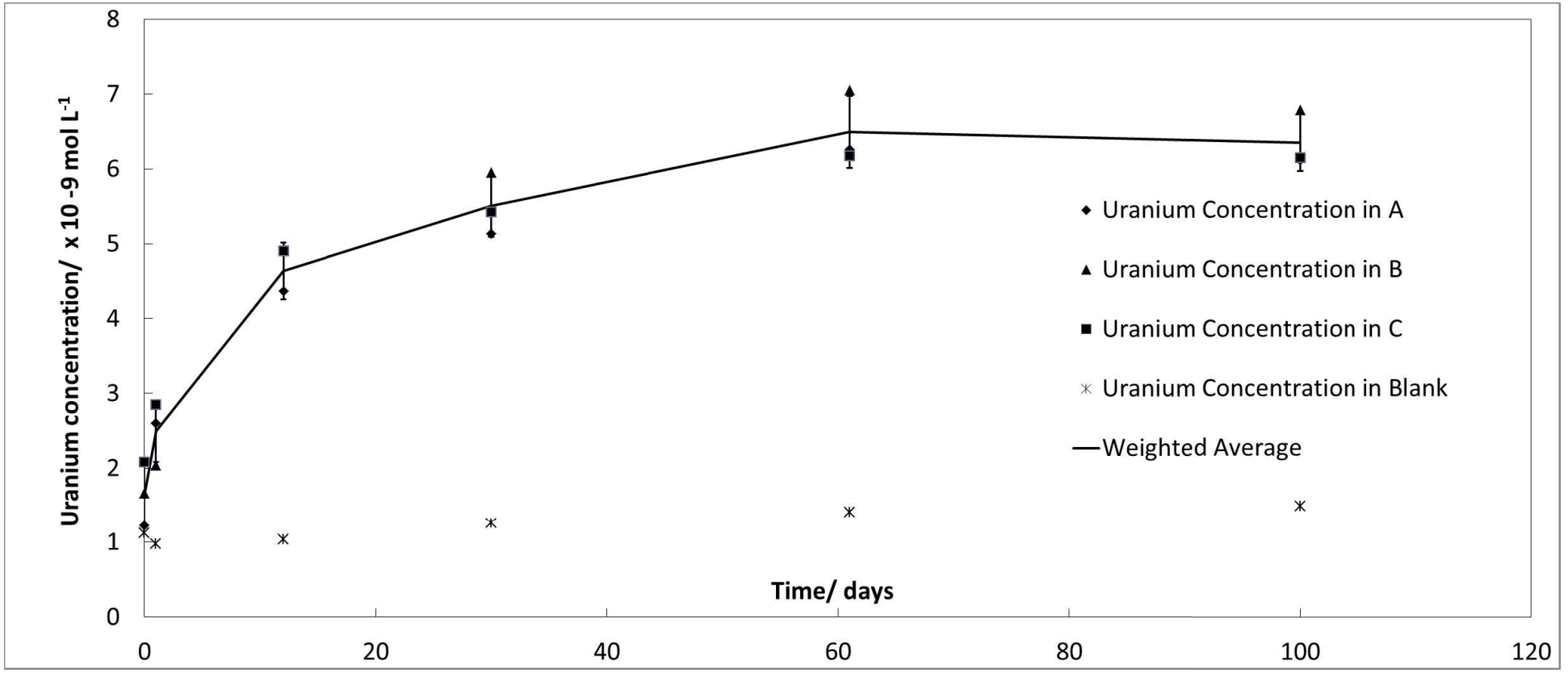
Uranium concentration/ x 10 -9 mol L-1
Time/ days
Uranium Concentration in A
Uranium Concentration in B
Uranium Concentration in C
Uranium Concentration in Blank
Weighted Average
0
1
2
3
4
5
6
7
8
0
20
40
60
80
100
120

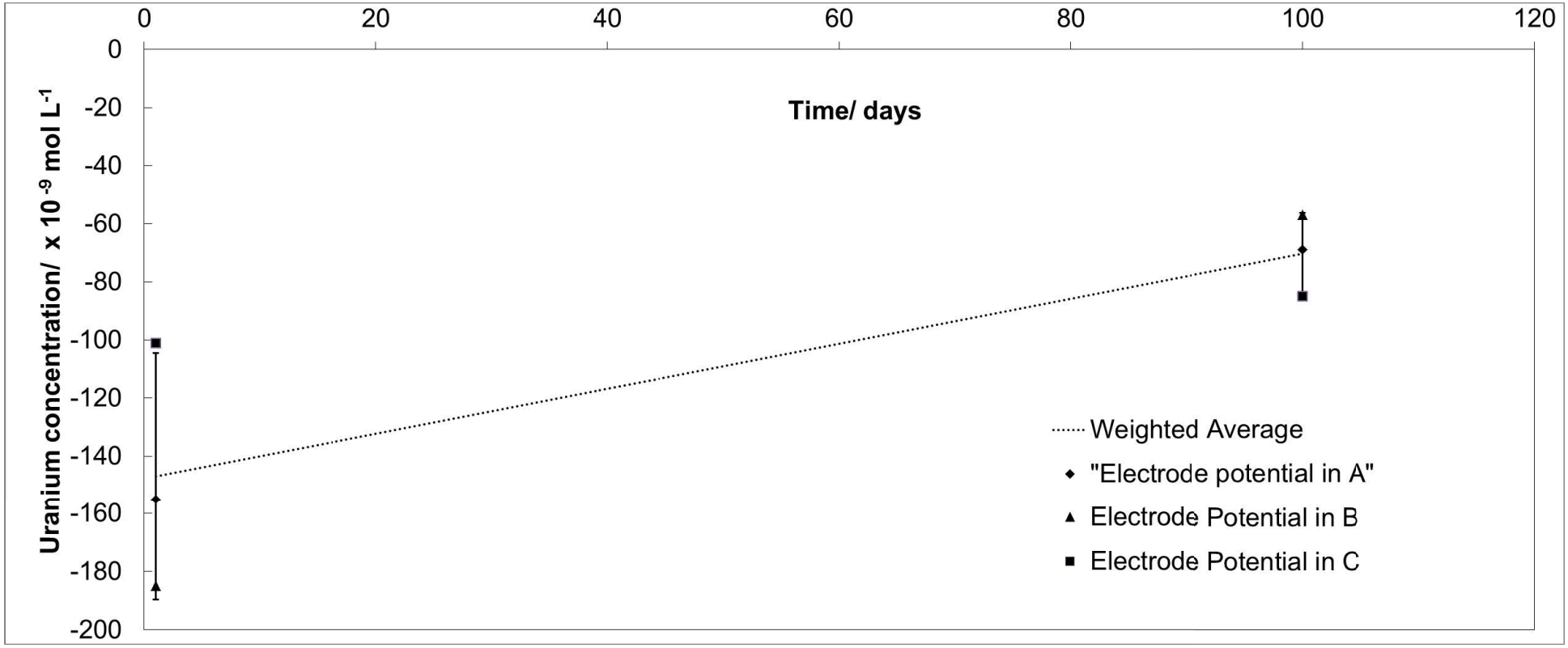
0
20
40
60
80
100
120
0
-20
-40
-60
-80
-100
-120
-140
-160
-180
-200
Time/ days
Uranium concentration/ x 10 -9 mol L-1
Weighted Average
"Electrode potential in A"
Electrode Potential in B
Electrode Potential in C

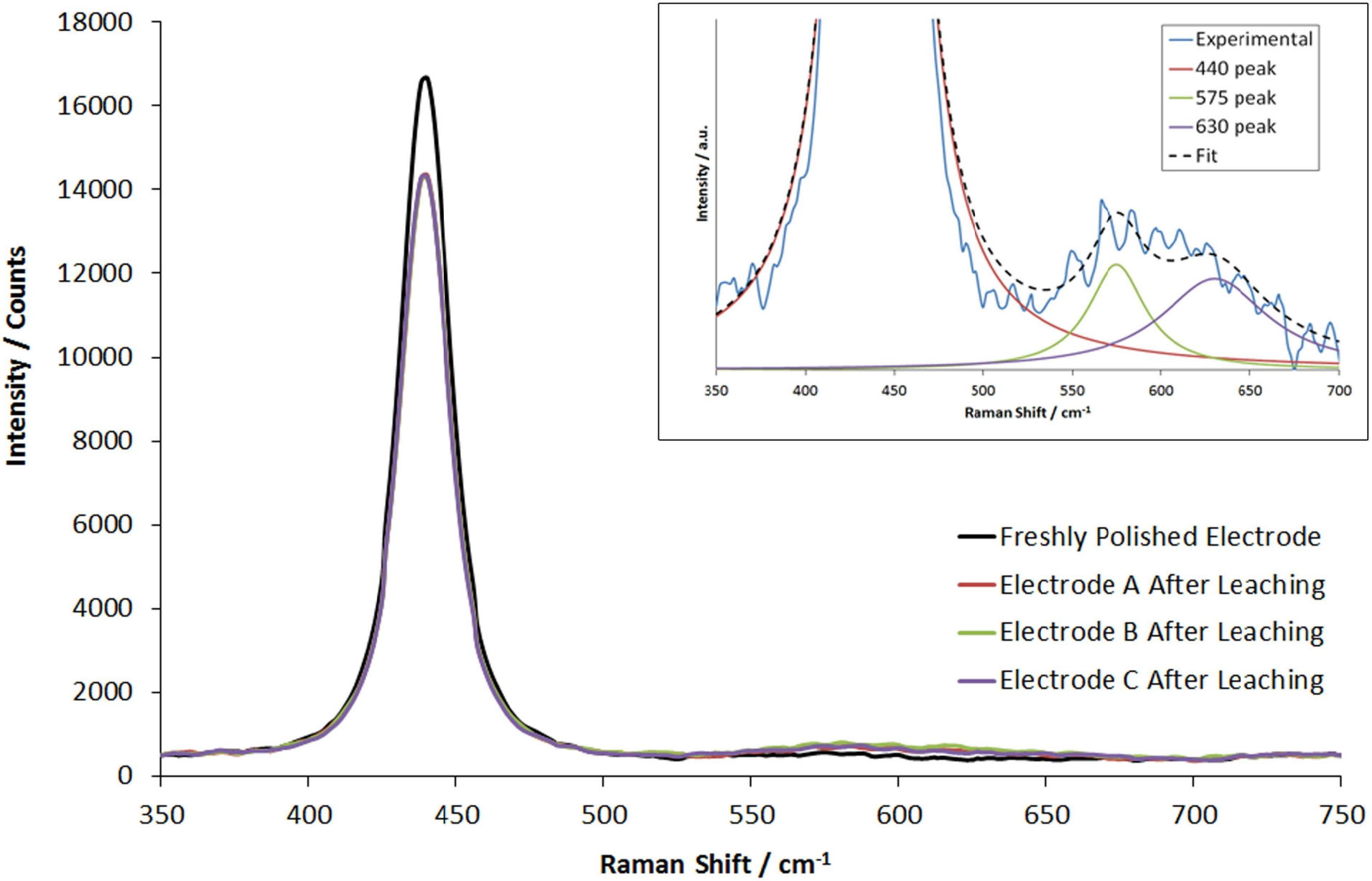
Intensity / Counts
18000
16000
14000
12000
10000
8000
6000
4000
2000
0
350
400
450
500
550
600
650
700
750
Raman Shift / cm-1
Freshly Polished Electrode
Electrode A After Leaching
Electrode B After Leaching
Electrode C After Leaching
Intensity / a.u.
Experimental
440 peak
575 peak
630 peak
Fit
350
400
450
500
550
600
650
700
Raman Shift / cm-1

(A)

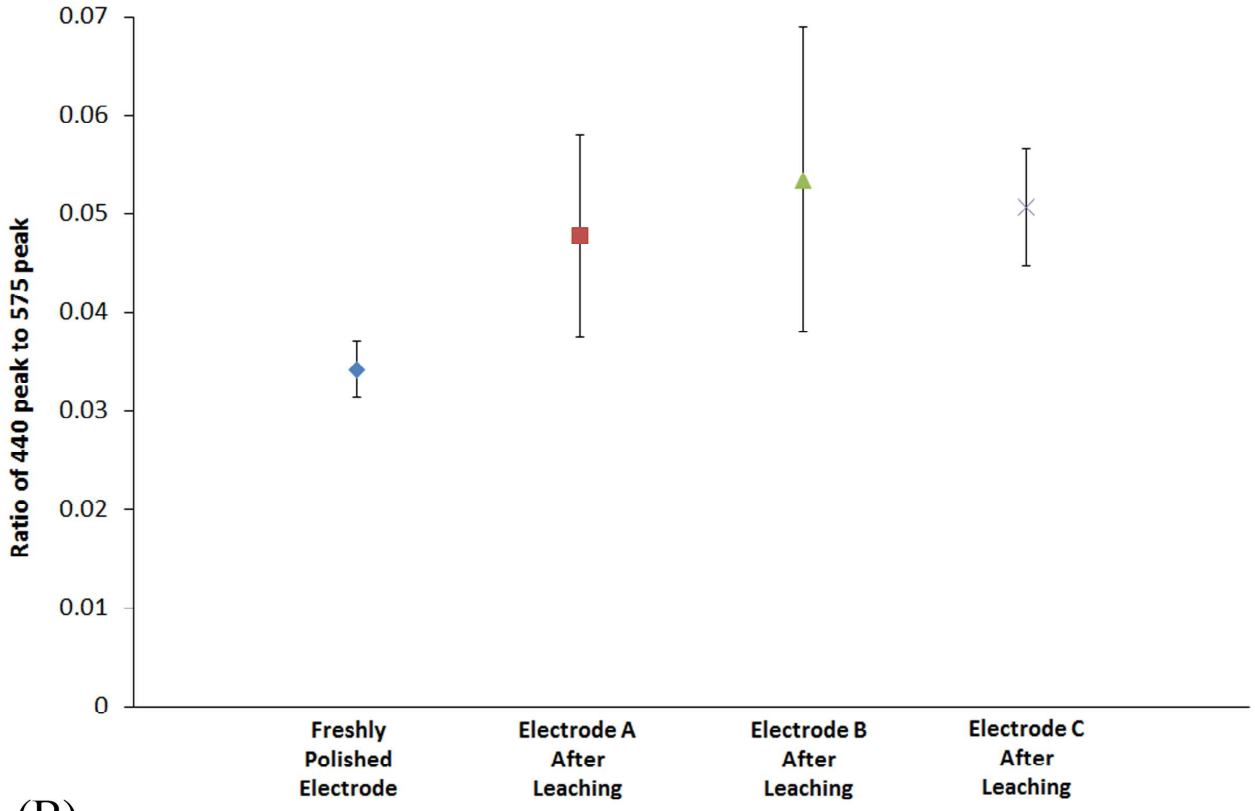
0.07
0.06
0.05
0.04
0.03
0.02
0.01
0
Ratio of 440 peak to 575 peak
Freshly Polished Electrode
Electrode A After Leaching
Electrode B After Leaching
Electrode C After Leaching

(B)

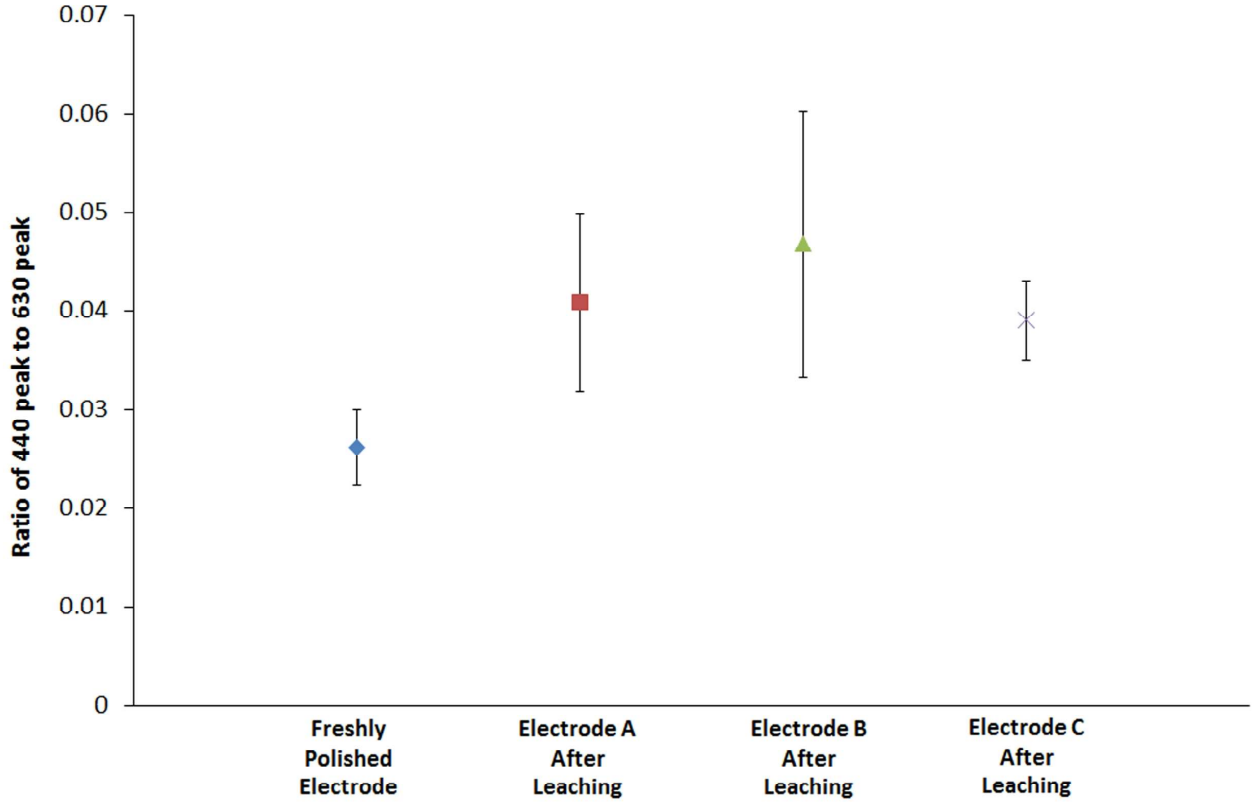
0.07
0.06
0.05
0.04
0.03
0.02
0.01
0
Ratio of 440 peak to 630 peak
Freshly Polished Electrode
Electrode A After Leaching
Electrode B After Leaching
Electrode C After Leaching

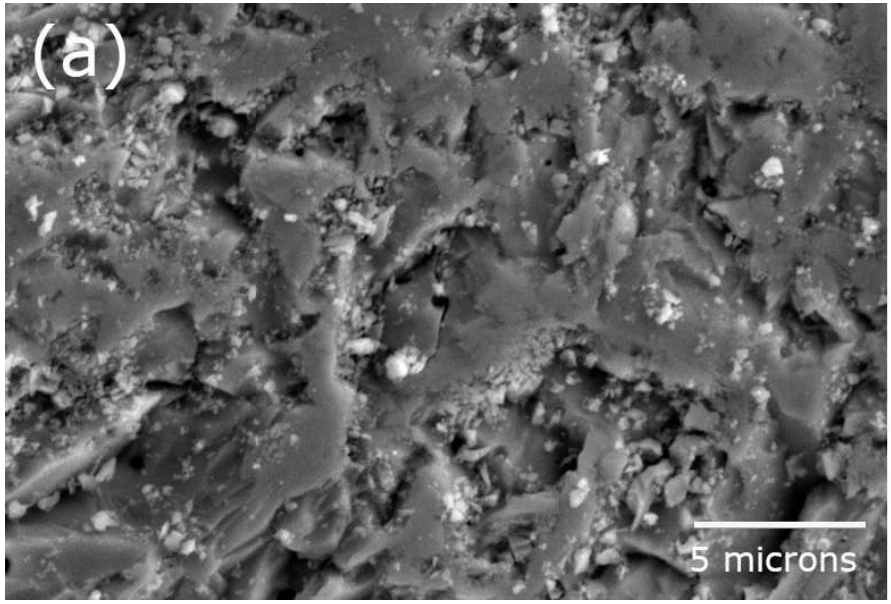
(a)
5 microns

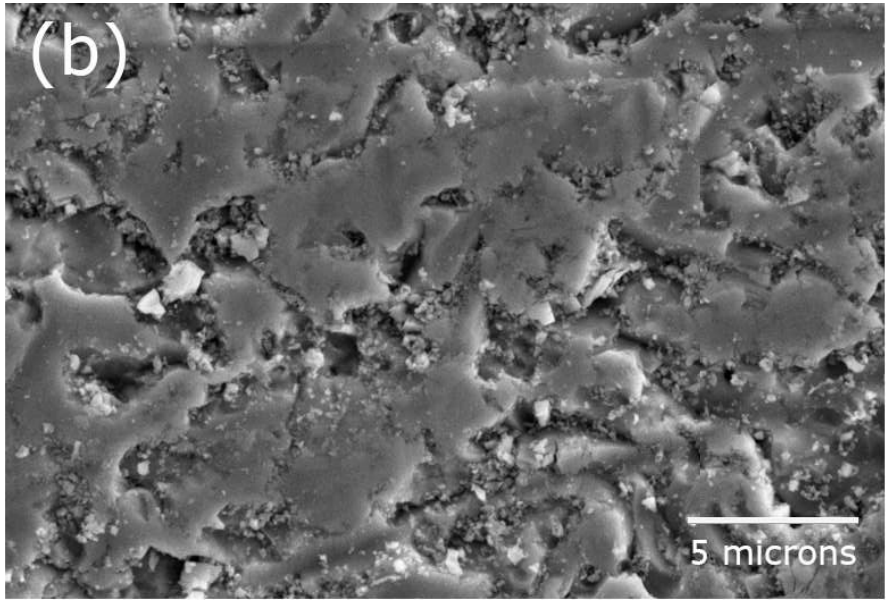
(b)
5 microns

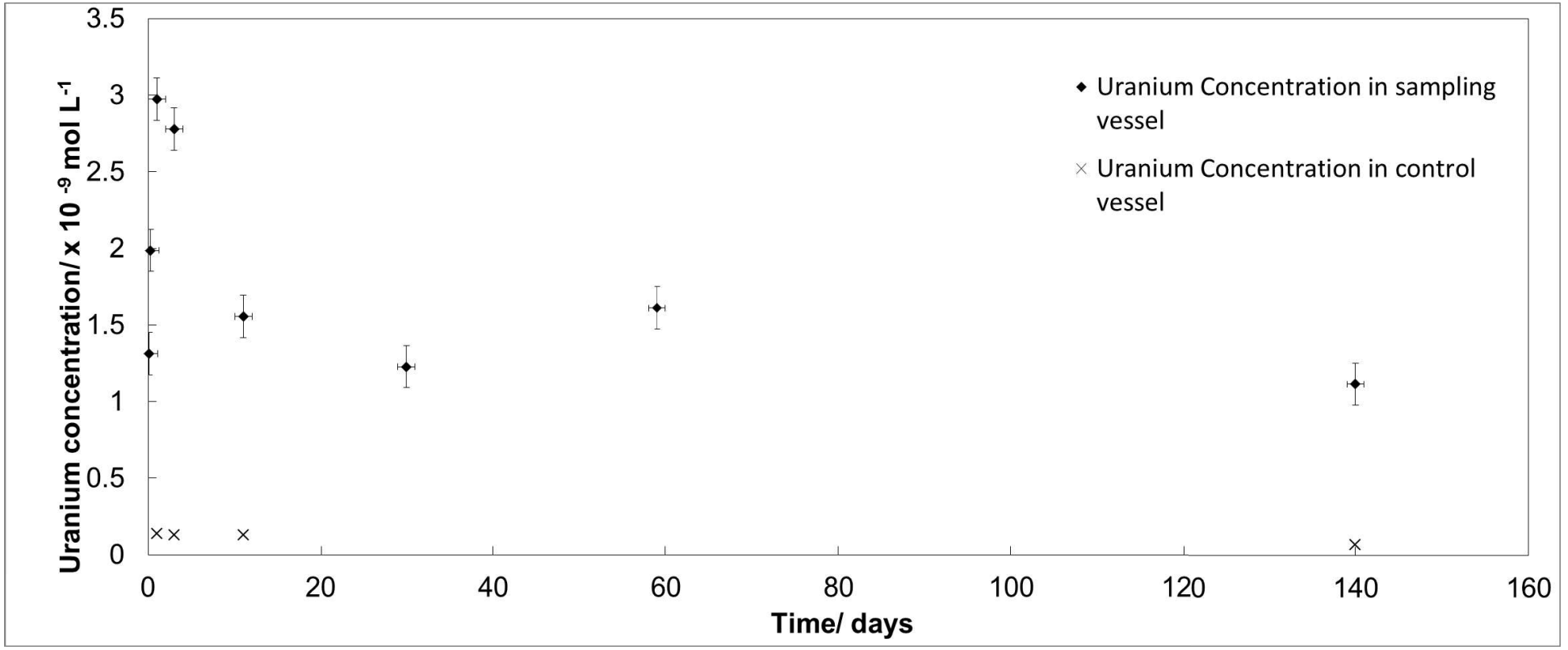
Uranium concentration/ x 10 -9 mol L-1
3.5
3
2.5
2
1.5
1
0.5
0
0
20
40
60
80
100
120
140
160
Time/ days
Uranium Concentration in sampling vessel
Uranium Concentration in control vessel

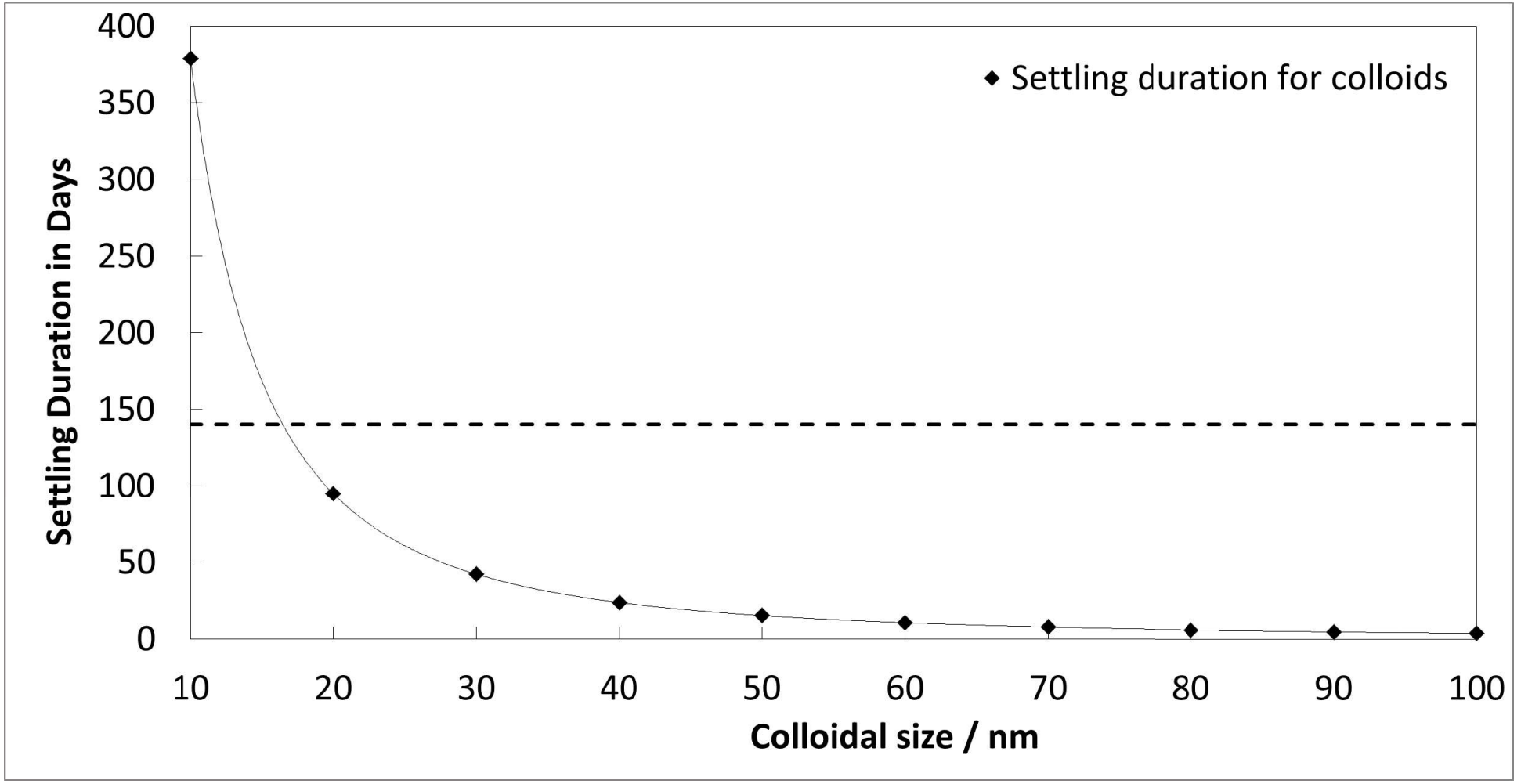
Settling duration for colloids
Settling Duration in Days
400
350
300
250
200
150
100
50
0
10
20
30
40
50
60
70
80
90
100
Colloidal size / nm

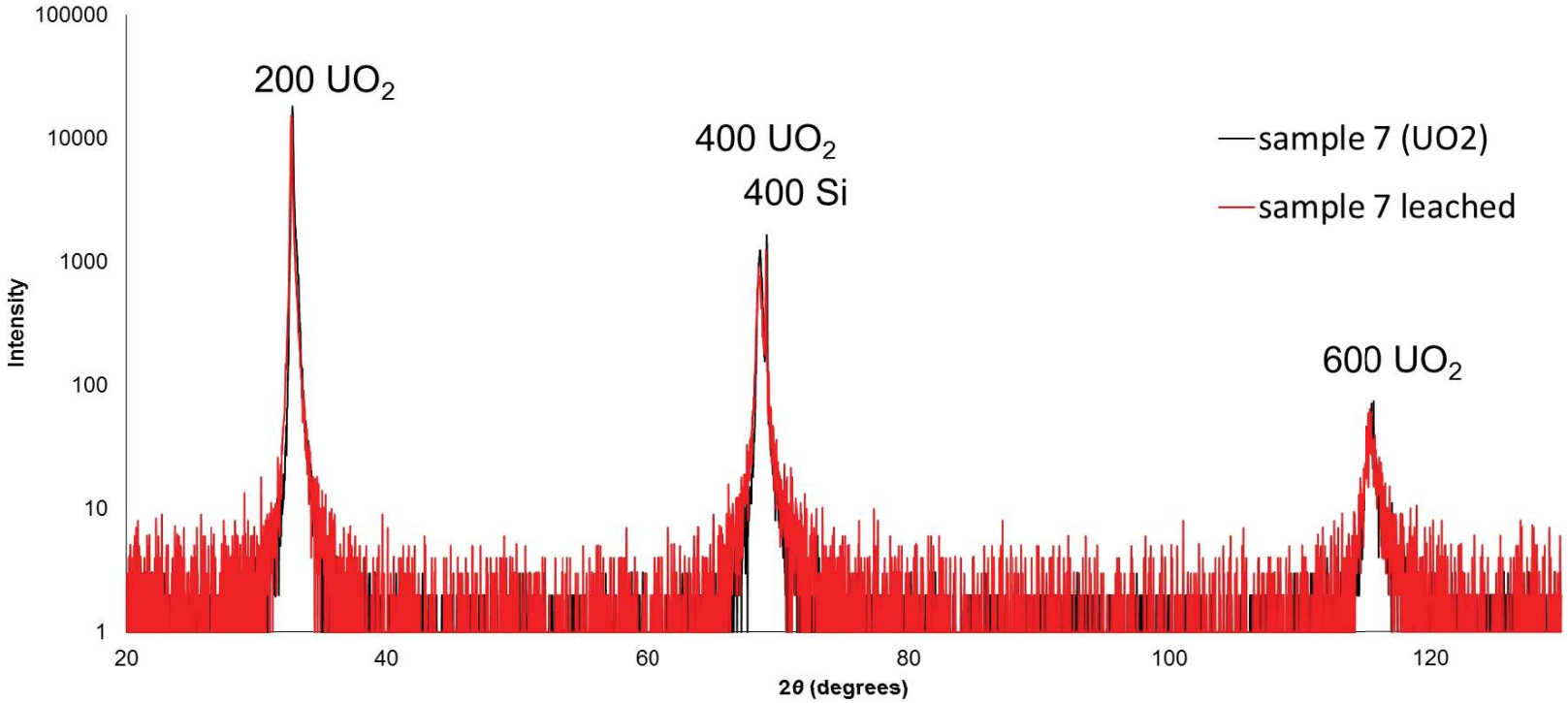
100000
10000
1000
100
10
1
Intensity
200 UO2
400 UO2
400 Si
600 UO2
sample 7 (UO2)
sample 7 leached
20
40
60
80
100
120
2θ (degrees)

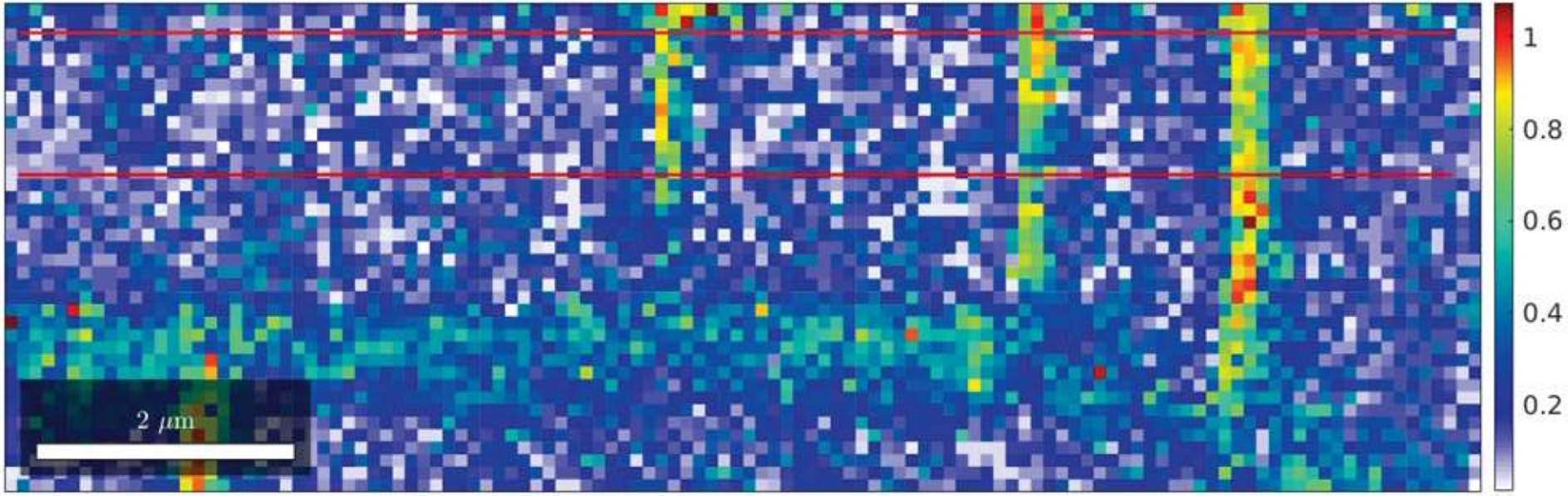
2 μm
1
0.8
0.6
0.4
0.2

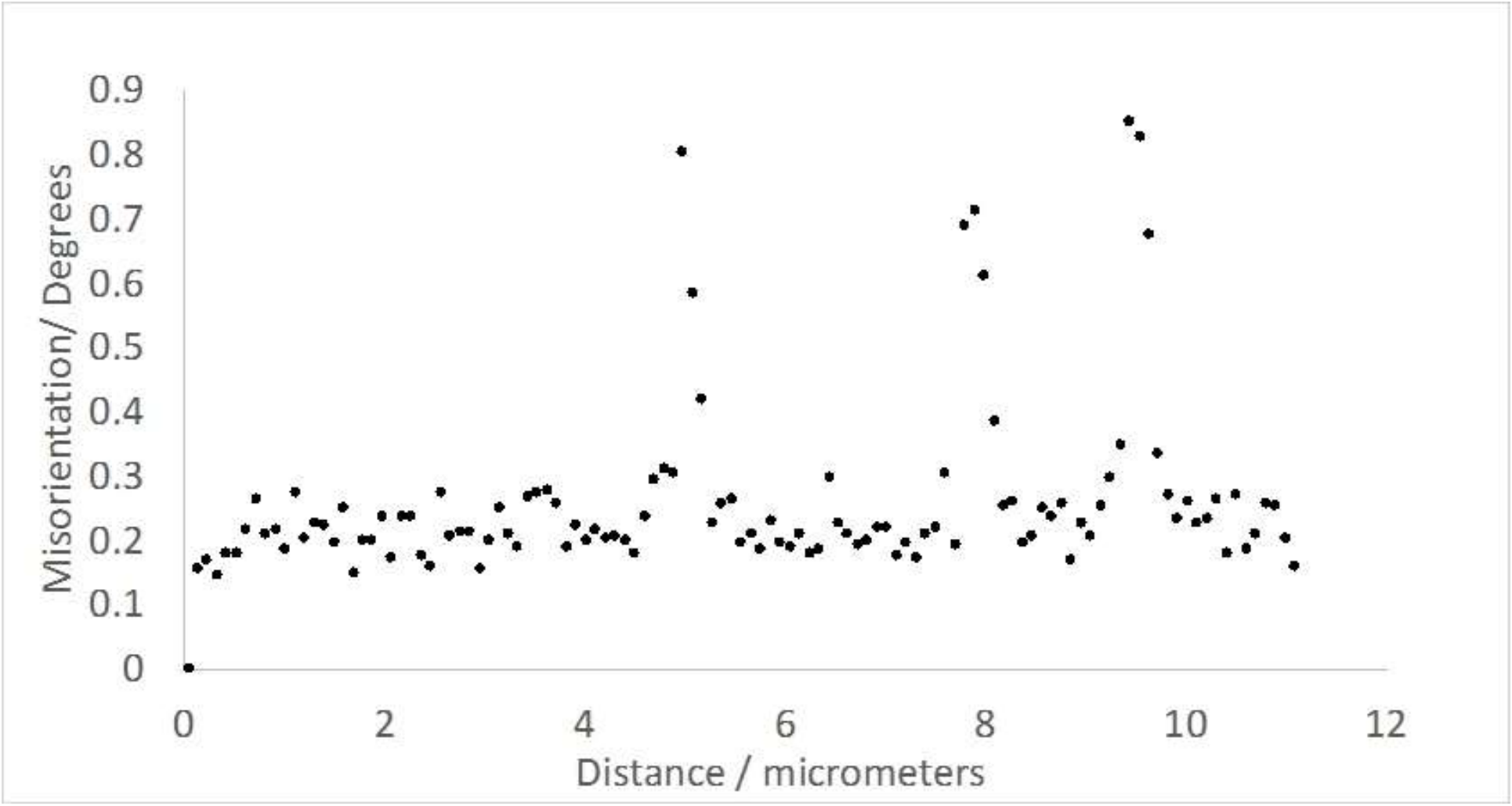
Misorientation/ Degrees
0.9
0.8
0.7
0.6
0.5
0.4
0.3
0.2
0.1
0
0
2
4
6
8
10
12
Distance / micrometers

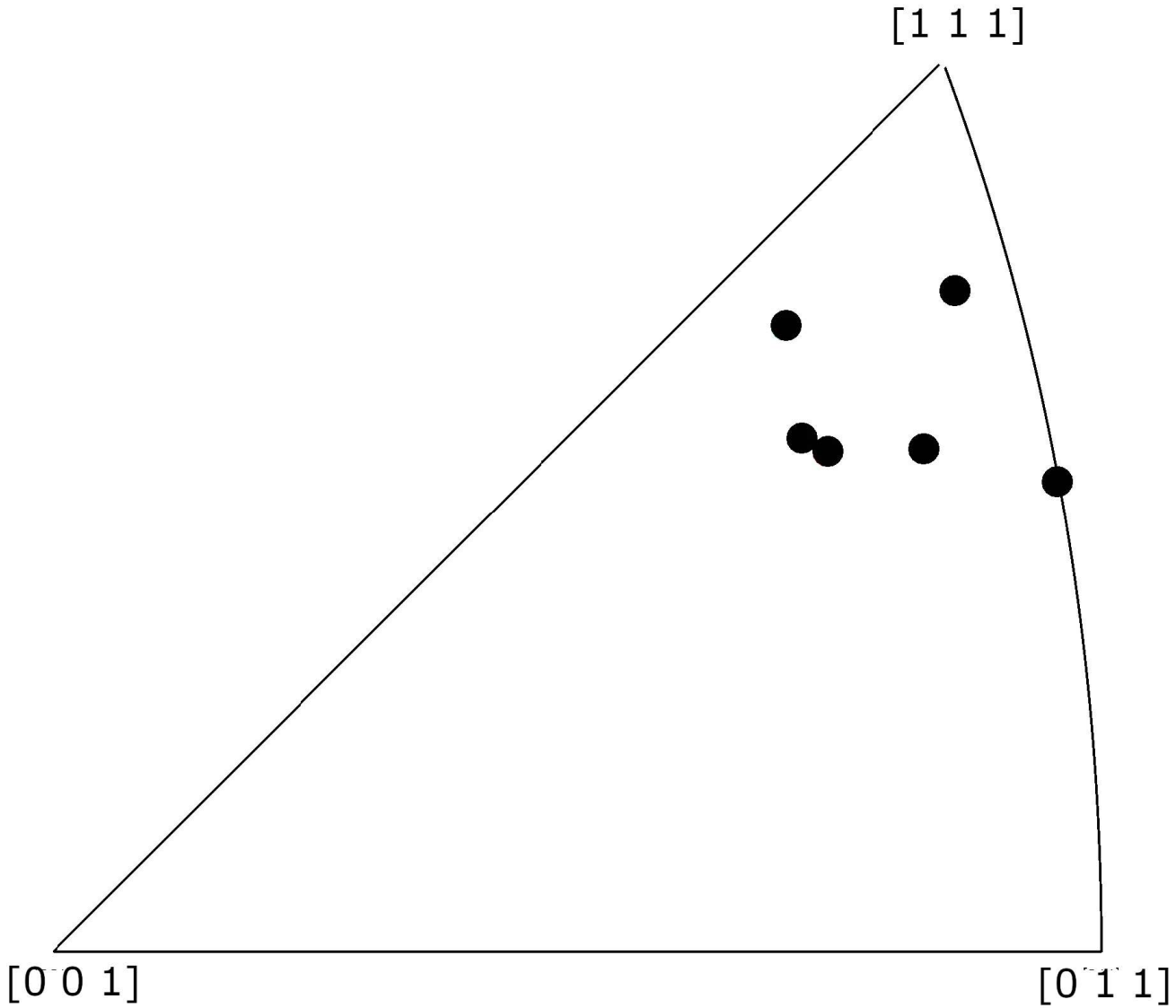
[1 1 1]
[0 0 1]
[0 1 1]

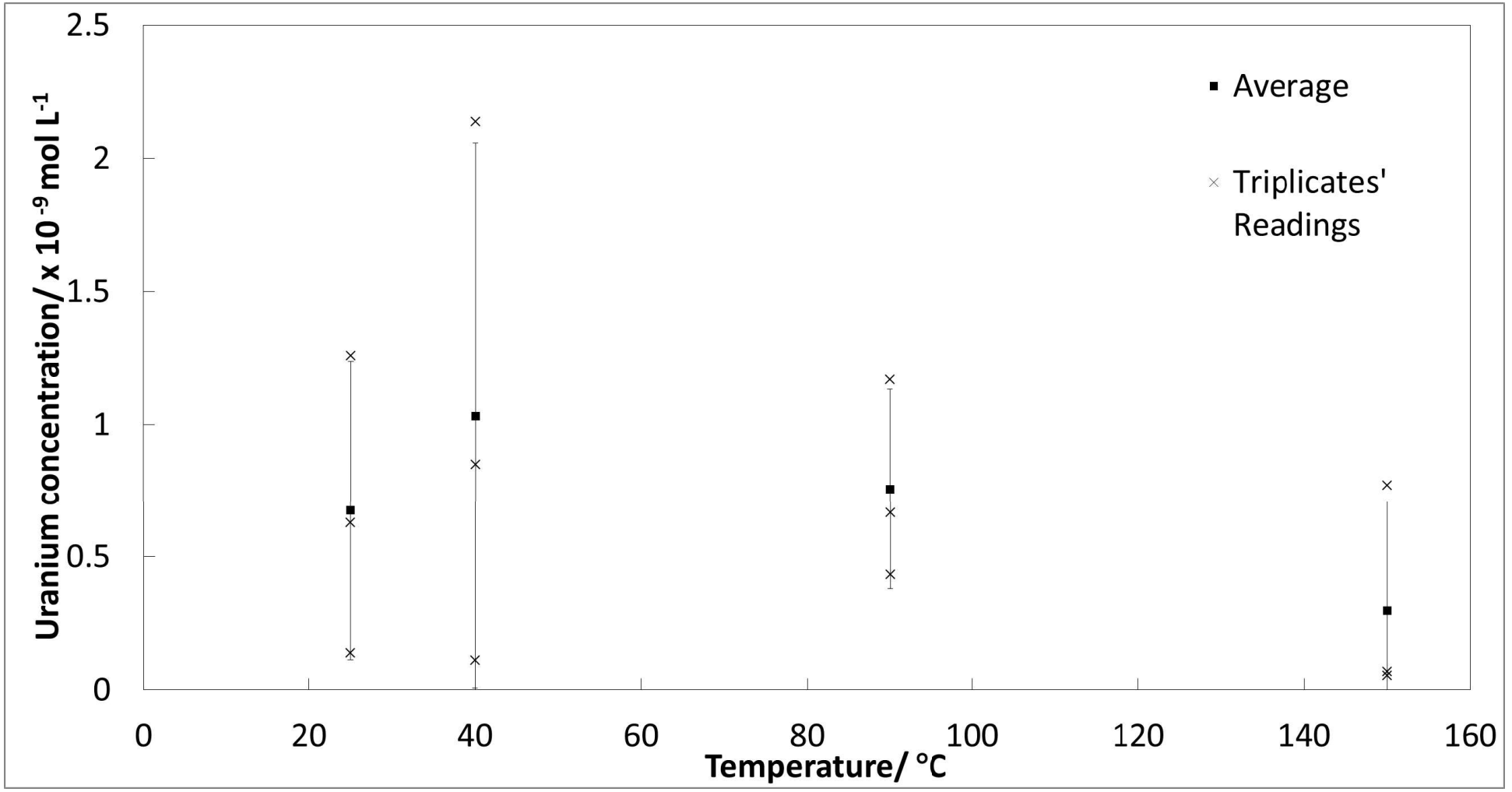
Uranium concentration/ x 10 -9 mol L-1
2.5
2
1.5
1
0.5
0
0
20
40
60
80
100
120
140
160
Temperature/ °C
Average
Triplicates' Readings

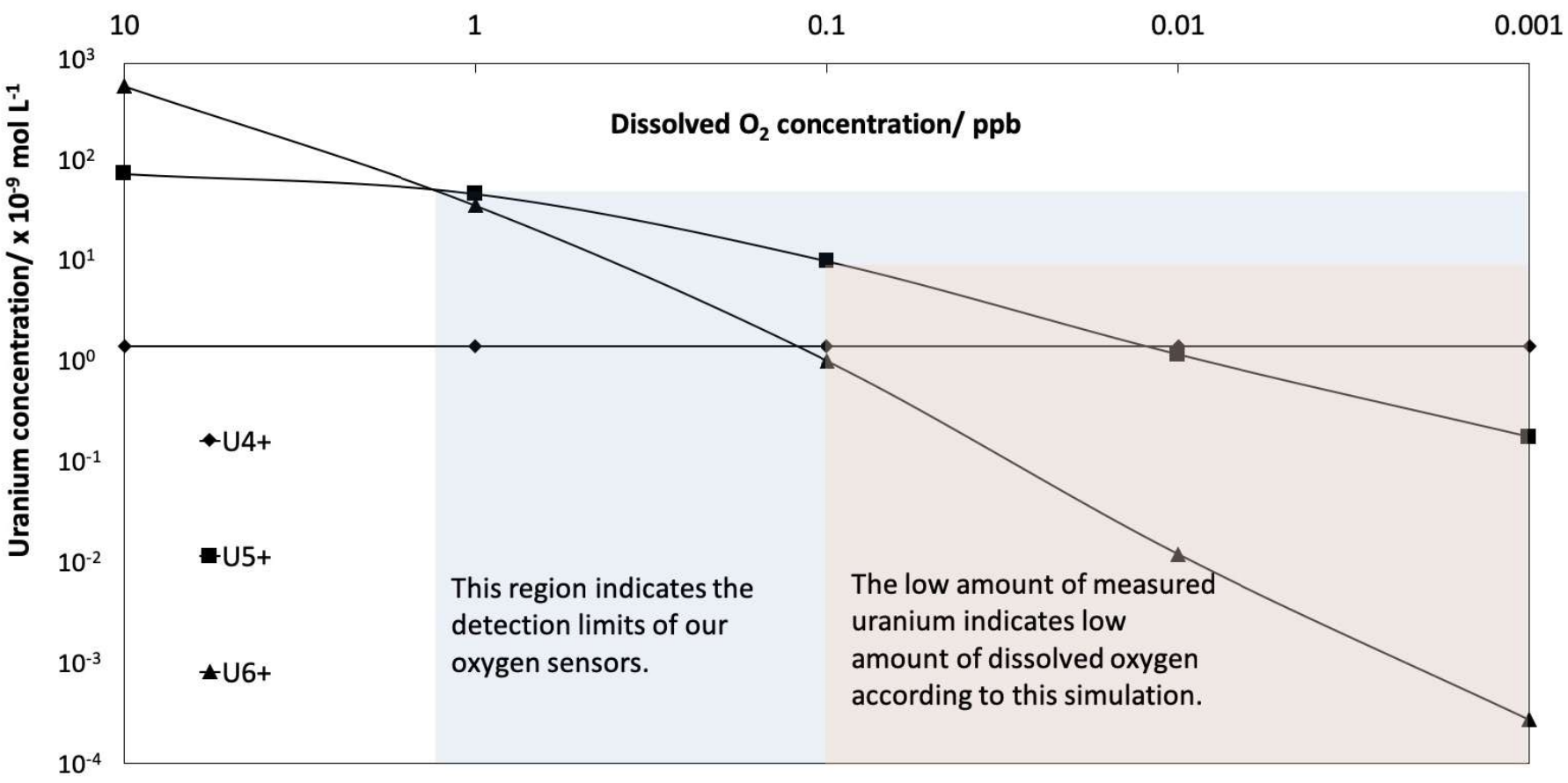
10
1
0.1
0.01
0.001
Dissolved O_2 concentration/ ppb
Uranium concentration/ x 10^{-9} mol L^{-1}
10^3
10^2
10^1
10^0
10^{-1}
10^{-2}
10^{-3}
10^{-4}
U4+
U5+
U6+
This region indicates the detection limits of our oxygen sensors.
The low amount of measured uranium indicates low amount of dissolved oxygen according to this simulation.

Figure Captions

Fig. 1. Uranium concentration in aliquots obtained from three vessels, A, B and C containing a uranium pellet each and a control vessel labelled as blank with the same set up without a uranium pellet.

Fig. 2. Open circuit potential of the uranium dioxide electrodes recorded at the beginning and end of this leaching experiment. Note values are plotted vs. the standard calomel electrode (SCE) for ease of comparison with data from (Shoesmith and Sunder, 1992).

Fig. 3. Main: Linear baseline subtracted, area averaged Raman spectra of a freshly polished UO_2 electrode and three UO_2 electrodes after 100 days dissolution over the Raman shift range 350 to 750 cm^{-1}. Inset: Example Lorentzian fit of defect bands at 575 cm^{-1} and 630 cm^{-1} from a single measurement point from electrode A after leaching.

Fig. 4. Lorentzian peak fit results for the data of Fig. 5, assuming peak maxima at 440, 575 and 630 cm^{-1}. Results are expressed as a ratio of (A) the 575 cm^{-1} peak and (B) the 630 cm^{-1} peak to the 440 cm^{-1} peak.

Fig 5. (a) SEM at the surface of the (a) pre-leached UO_2 pellet after polishing and (b) the post-leached UO_2 pellet.

Fig. 6. Dissolved uranium concentrations of extracted aliquots from both the uranium dioxide thin film dissolution vessel and the silicon wafer only vessel (control), determined by ICP-MS.

Fig. 7. (a) 30000× magnified secondary electron and (b) backscattered electron micrographs of the thin film before prewash and heat treatment.

Fig. 8. (a) 30000× magnified secondary electron and (b) backscattered electron micrographs of the leached thin film surface after 140 days dissolution.

Fig. 9. (a) 200,000× magnification secondary electron and (b) backscattered electron micrographs on the nucleate with clear growth domains ranging between 20-100 nm (Aleksej J. Popel, Beng Thye Tan, Thomas Gouder, Giulio I. Lampronti, Jason Day, Rachel Eloirdi, Alice Seibert, 2019).

Fig. 10. Secondary (a) and backscattered electron (b) micrographs of secondary precipitates detected at 30, 000× and secondary (c) and backscattered electron (d) micrographs of secondary precipitates detected on blank silicon substrates at 100, 000× magnifications.

Fig. 11. Stokes' equation predicts the relationship between the settling/sedimentation duration against colloidal size for colloidal precipitation in 2 cm deep leaching vessel, similar to our set-up.

Fig. 12. XRD diffractogram for the pre-leached and post-leached UO_2 thin film sample on a silicon substrate. Only 200, 400, and 600 UO_2 reflections corresponding to the (001) crystallographic orientation are present.

Fig. 13. Thresholded EBSD map showing the misorientation angle of every pixel with respect to the average orientation. The twelve adjacent misorientation profiles delimited by the two red curves were averaged to obtain the averaged misorientation profile of Figure 16.

Fig. 14. Averaged misorientation profile (see Fig. 15 as a reference)

Fig. 15. Plot of misorientation axes obtained on either side of the three cracks. They have similar misorientation axis with some statistical variation.

Fig. 16. ICP-MS determined uranium concentration values after 390 days of dissolution at temperatures from 25 to 140 ˚C.

Fig. 17. Phreeqc simulation of dissolved uranium concentration at equilibrium as a function of oxygen content for UO_2 (NEA) dissolution in deionized water at room temperature, where log K^0 of UO_2 = 54.5 $\pm$ 1.0.

In the ESI

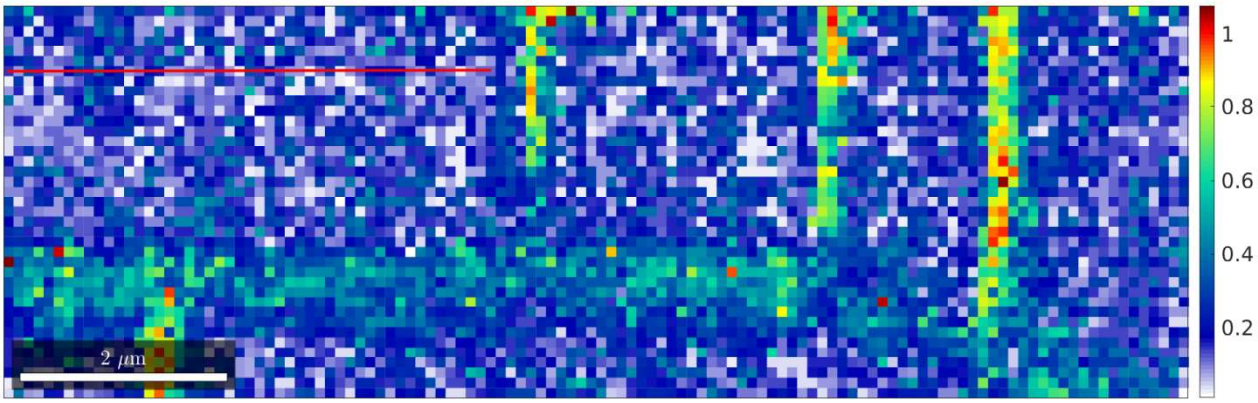

Fig. ESI 1. Thresholded EBSD map showing the misorientation angle of every other pixel with respect to the average orientation. The misorientation profile used for the quantification of the precision error is shown in red.

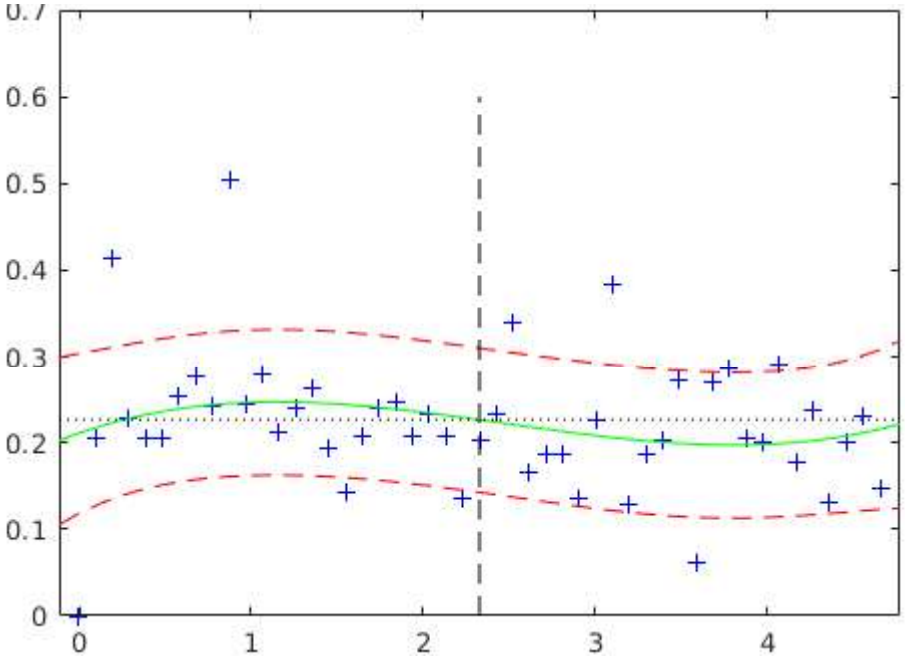

Fig. ESI 2. Distance (in um) versus misorientation angle (in °) fitting plot of the profile shown in Figure 13 (green curve). The red dashed represent the 3rd order polynomial fitting curve plus or minus ± sigma = 0.08°.